RHEOLOGICAL ASPECT OF CELL-FREE LAYER FORMATION IN MICRO-BLOOD FLOW

: Experimental and Numerical Study

NAMGUNG BUMSEOK

(MS. in Biomedical Eng., Yonsei University)

A THESIS SUBMITTED

FOR THE DEGREE OF DOCTOR OF PHILOSOPHY

DEPARTMENT OF BIOENGINEERING

NATIONAL UNIVERSITY OF SINGAPORE

2012

DECLARATION

I hereby declare that this thesis is my original work and it has been written by me in its entirety. I have duly acknowledged all the sources of information which have been used in the thesis.

This thesis has also not been submitted for any degree in any university previously.

NAMGUNG BUMSEOK		**DEC. 04, 2012**
Name of Student	Signature of Student	Date

Name: Namgung Bumseok

Degree: Ph.D.

Dept: Department of Bioengineering

Thesis Title: Rheological Aspect of Cell-Free Layer Formation in Micro-blood Flow: Experimental and Numerical Study

Abstract

This thesis aims to provide detailed insight into the rheological aspects of cell-free layer (CFL) formation in micro-blood flow and its relation to red blood cell (RBC) aggregation. Both experimental and computational approaches were utilized in characterizing the relationship between the CFL width change and RBC aggregation. The rheological effects of the CFL on the arteriolar wall shear stress (WSS) were examined in the rat cremaster muscle *in vivo*. A new histogram-based algorithm was suggested for better determination of the CFL width. The elevation in RBC aggregation increased the CFL width and attenuated the RBC-wall contact frequency. Computational prediction showed that the aggregation effect on the CFL width was prominent in low shear conditions, but this effect was diminished in high shear conditions. Inclusion of the CFL width in determining the WSS revealed that the temporal CFL variation might have an increasing effect on the WSS, and this could be enhanced by RBC aggregation.

Keywords: microcirculation, plasma layer, red blood cell aggregation, wall shear stress

ACKNOWLEDGEMENTS

First of all, I sincerely thank Dr. Sangho Kim for his passionate guidance and inspiration during my graduate study. Without his great supervision, my research could not be accomplished. His scientific expertise and deep knowledge on hemodynamics and on blood rheology led me to achieve my degree. Whenever I fell into deep depress and distress, he always encouraged me to face the difficulties resolutely.

I am deeply indebted to Mr. Seung Kwan Cho who is not only my senior but also my old friend. During the time with him for last ten years, he always carefully listened to my voice and gave me valuable advices. A sincere appreciation needs to be extended to my colleagues whose friendship I will cherish the memory that we were together and were friend, including: Dr. Peng Kai Ong, Mr. Meong Keun Ju, Ms. Hyun Rim Oh, Mr. Maung Ye Swe Soe, Mr. Shihong Yang, Mr. Jae Sung Son, Mr. Young Jun Shin and Mr. Kyung Ryoul Mun. I specially thank Ms. Yeon I Woo for her expert technical assistance and animal surgery. I also need to extend my deepest appreciation to Prof. Hansung Kim and Dr. Dohyung Lim for their great guidance during the time when I was in Yonsei University for my Master degree.

Last but not least, I dedicate my dissertation to my life partner, Hanna, and to my family. Without their sacrifice and unwavering love, it was definitely not possible to accomplish my research. I really appreciate their unbounded support and encouragement. I would like to and have to say to them that I deeply love you and will love forever.

Jesus, I praise your glory and unmerited favor. I thank you that as I look to you for all my needs and wants in the midst of every difficulty and challenge, you place me at the right place at the right time and provide me with every resource. I believe that I can walk above my problems when I keep my eyes on you and trust you.

Your word is a lamp to my feet and a light for my path. - Psalms 119:105

TABLE OF CONTENTS

SUMMARY

Although there is great interest in the cell-free layer (CFL) due to its significant role in the microcirculatory system, detailed information on its rheological effects in microcirculation and its relation to red blood cell (RBC) aggregation is limited. The following aims are focused on establishing the relationship between RBC aggregation and the CFL width change and its effect on the blood rheology in the microcirculation.

Firstly, determination of an appropriate method for the CFL measurement *in vivo* and/or *in vitro* is essential in providing detailed information on the characteristics of the CFL. Four different histogram-based thresholding algorithms (Otsu's, intermodes, minimum and 2nd peak) were examined and compared to propose more suitable methods. Using our current experimental system, the results proved that the CFL width determined by the minimum algorithm showed the best accordance in line with the manual measurement.

In vitro experiments were performed by perfusing RBCs in a circular microtube (25 μm ID) in order to provide detailed insight into the dynamic changes of CFL width at both physiological (Normal) and pathological (Hyper) levels of aggregation. The cell-free area (CFA) was also measured to provide additional information on the CFL variation in space and time domains. A prominent enhancement in the mean CFL width was found in hyper-aggregating conditions as compared to that in non-aggregating conditions ($P < 0.001$). The frequent contacts between the RBC and tube wall were observed in the flow, and these contacts became greatly attenuated when the aggregation level was increased from none to normal ($P < 0.05$) and hyper ($P < 0.001$) levels. In

addition, the enhanced aggregation level from none to hyper significantly enlarged the CFA ($P < 0.01$).

RBC aggregation effect on the CFL width change was further investigated with a two-phase computational model. The model development integrates both empirical relations for relative viscosity (ratio of apparent viscosity to medium viscosity) and core viscosity measured on independent blood samples to create a continuum model that includes RBC core and the CFL. The constitutive relations were derived from *in vitro* experiments performed with three different glass-capillary tubes (ID = 30, 50 and 100 μm) over a wide range of pseudoshear rates (5-300 s^{-1}). The aggregation level of the blood samples was also varied by adding Dextran 500 kDa. Our model predicted that the CFL width was strongly modulated by the relative viscosity function. Aggregation increased the CFL width, and this effect became more pronounced at low shear rates.

Lastly, effect of CFL width on the wall shear stress (WSS) and its relation to RBC aggregation were investigated by examining the hypothesis that temporal variations of the CFL would increase the WSS and this effect could be enhanced by RBC aggregation. The CFL widths in the arterioles (29.5-67.1 μm ID) of rat cremaster muscle were measured and the width variations were introduced into the WSS estimation. The WSS became underestimated when the CFL variation was not taken into account in all rheological conditions, and this effect became more pronounced with increasing CFL variability.

Keywords: microcirculation, plasma layer, red blood cell aggregation, wall shear stress

LIST OF TABLES

LIST OF FIGURES

CHAPTER I: INTRODUCTION AND BACKGROUND

1. Hemodynamic aspect of red blood cell (RBC) aggregation in microcirculation

1.1 Important role of RBC in microcirculation

"Hemodynamics" is defined as "the physical aspect of the cardiovascular system" or "cardiovascular biophysics" by McDonald [70]. In recent decades, hemodynamics has become a multidisciplinary study on the suspension of blood, which includes blood rheology, cell mechanics and physiology.

Blood, a vital fluid of humans, is a concentrated suspension of cells and cell fragments in plasma. The suspending components include RBCs (or erythrocytes), white blood cells (or leukocytes) and platelets [88] (Figure I-1). The RBC is the major cell component that constitutes 40%-45% of blood in physiological condition. Healthy human RBCs are reported to survive for about 120 days in the circulation. The normal shape of RBC consists of a biconcave discoid with a width of ~7.7 μm, thickness of ~2.8 μm, surface area of ~130 μm^2 and volume of ~98 μm^3 [37]. Due to its shape, RBC has a great surface to volume ratio as compared to spheres, which allows RBC to deform without significant strain [103]. Therefore, the RBC can even pass through micro-vessels (typically capillaries) with diameters smaller than its size.

The RBC has been of particular interest in many previous hemodynamic studies as it is the major cell component in the blood and supplies oxygen to surrounding tissues. In particular, the peripheral region of circulatory system (microvasculature), which consists of arterioles (Figure I-2A), venules (Figure I-2B) and capillaries (Figure I-2C), can be characterized down to micro-size diameters (< 200 μm) and microfluidic environment.

The microvasculature provides a large area that allows the exchange of material and vital substances with tissue [94]. Accordingly, even small changes in blood properties or flow conditions might significantly influence the microcirculatory system functions.

Chapter I

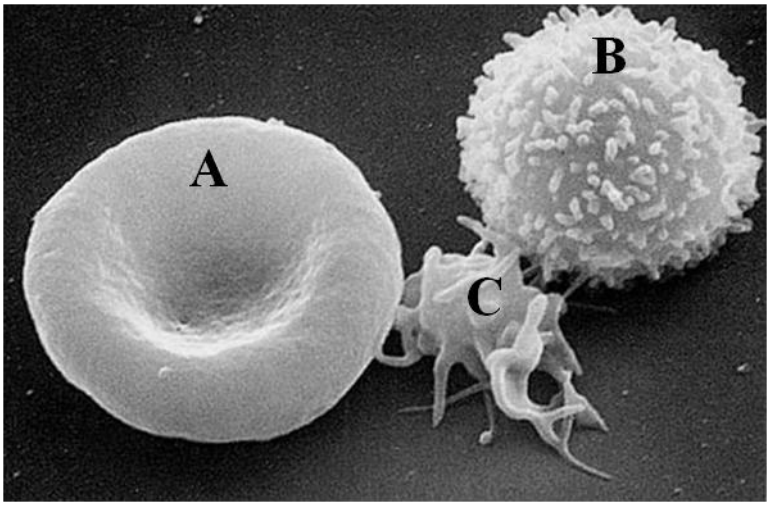

Figure I-1: Electron microscopic image of blood cell components.
A and B are red blood cell and white blood cell, respectively. C is platelet.
(*Image courtesy of Electron Microscopy Facility at The National Cancer Institute at Frederick (NCI-Frederick))*

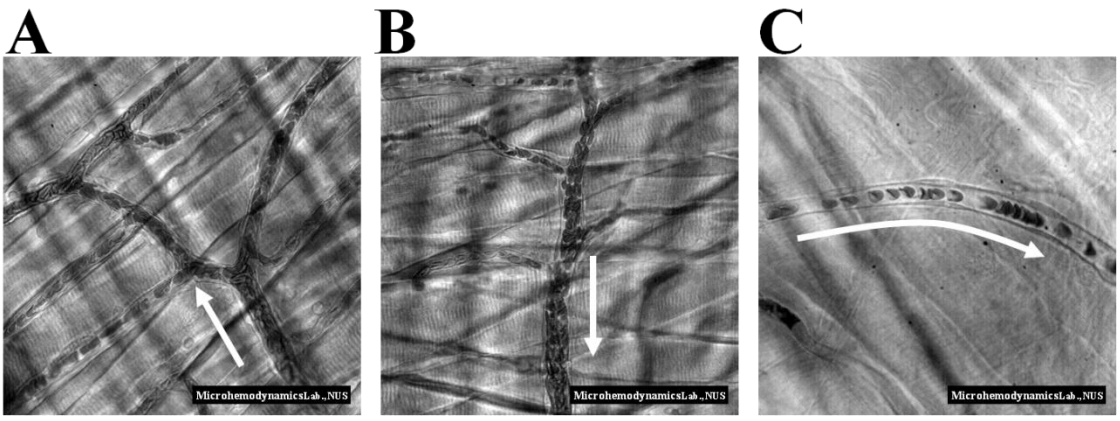

Figure I-2: Typical example of arteriolar flow (A), venular flow (B) and capillary (C) flow in a rat cremaster muscle.
The arrow indicates the flow direction.

1.2 Principle mechanism of RBC aggregation

Since the RBCs play a vital role in humans, its rheological characteristic has been studied in many previous studies. The RBCs can form aggregates (stack-of-coin-like rouleaux, see Figure I-3) which is a reversible feature of blood. The RBC aggregation can be modulated by shear forces [16, 25, 106] under shear flow. Low shear conditions are more favorable for strong aggregate formation whereas high shear forces easily dissociate the formed aggregates. This feature is a key mechanism that explains how blood exhibits a shear-dependent non-Newtonian behavior under shear flow.

Previous studies of the RBC aggregation tendency among different animal species [8, 10, 79, 89] have shown that athletic species have a higher aggregation capacity than non-athletic ones [89]. However, the exact role aggregation plays in the circulatory system is not fully elucidated [73]. There are two main factors influencing the RBC aggregation; the suspending medium composition (extrinsic factor) and cellular properties (intrinsic factor). RBC aggregation requires the induced presence of an "aggregant" in the suspending medium such as fibrinogen in native plasma. The RBC aggregates cannot be formed if the cells are washed and re-suspended in a protein-free or polymer-free solution [35, 68, 78, 91]. As shown in Figure I-4, the RBC aggregation of rat blood is not found in its native plasma, but aggregation can be induced by adding Dextran 500. Addition of Dextran 500 might not influence the membrane elasticity of RBC, as reported in a previous study, because the membrane elasticity of RBC is independent of dextran concentration [19], however, there is a minimal influence on cell volume and surface area [77]. Hence, the modification of membrane due to dextran might not be involved in the dextran-induced RBC aggregation. In addition, experimental evidence indicated that

RBCs' tendency to aggregate ("aggregability") would be another important intrinsic factor [9, 10]. A relevant study showed that horse RBCs exhibited a higher level of aggregation than human RBCs in the same concentration of polymer solution [10].

There are two coexisting theoretical models, namely the bridging model and depletion model, which explain the principle mechanism of the aggregation. The bridging model hypothesizes that aggregation can occur when the binding force, due to bridging effect between cells when macromolecules are absorbed onto adjacent cell surfaces, exceeds the disaggregating force due to electrostatic repulsion [91]. In contrast, the depletion model postulates that a preferential exclusion of macromolecules from RBC surface, which generates an osmotic gradient, draws fluid away from the intercellular gap and enhances the collective movement of adjacent cells [78, 97]. In recent years, the depletion model has been more commonly accepted by researchers. Although the two theories are still under debate, it is obvious that macromolecules play a common role in reducing the gap between RBCs, which results in an increase of the tendency to form aggregates.

Figure I-3: Rouleaux formation induced by Dextran 500 infusion in rat venule.

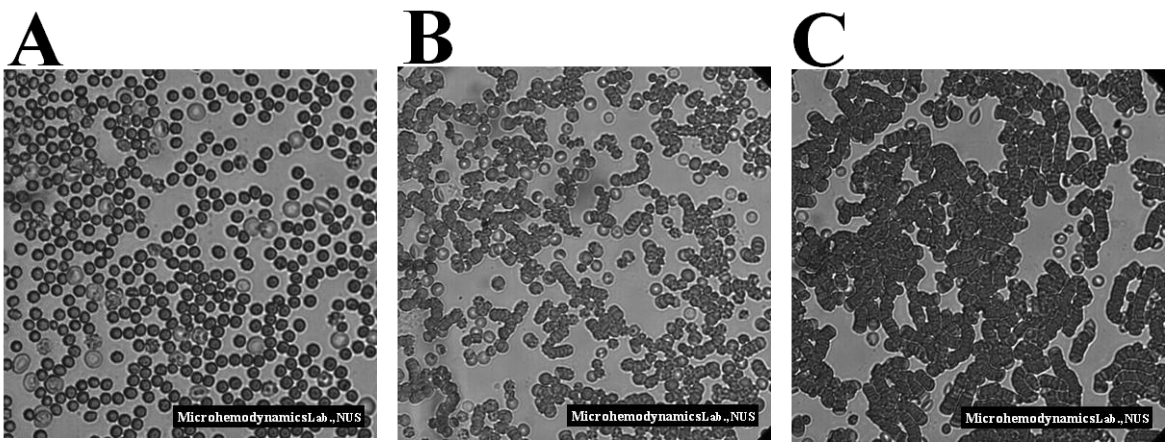

Absence of aggregation	Physiological condition	Pathological condition
M = 0.0	M = 16.69	M = 24.18
	(Dex. Conc.: 200 mg/kg)	(Dex. Conc.: 250 mg/kg)

Figure I-4: Typical microscopic images of Dextran 500 induced rat RBC aggregation at three different levels (A, B and C) of dextran-PBS concentration.
M indicates the value obtained from Myrrene aggregometer at M0 mode.

1.3 Clinical relevance of RBC aggregation

Many clinical studies have reported that abnormally intensified aggregation, namely hyper-aggregation (Figure I-4C), is a common response to hemorheological disorders. The acute and chronic elevation in aggregation is frequently found in sepsis [11], HIV infection [48, 74], nephritic syndrome [86], hypertension [27, 62, 98], rheumatoid arthritis [64] and diabetes mellitus [26]. These clinical reports propose that alteration of RBC aggregation may be a primary cause of abnormal microcirculatory responses. Therefore, hyper-aggregation syndrome can occur in those pathological conditions. A study that assessed correlation between RBC aggregation and inflammatory state showed that an abnormally elevated concentration of C-reactive protein was observed in the inflammatory state, which in turn results in an enhancement of RBC aggregation [3]. Other studies have also shown that RBC aggregation is significantly dependent on the fibrinogen concentration in plasma [13, 35, 68]. Thus, hyper-aggregation provides visible evidence that reflects the rheological alteration in inflammatory system under pathological conditions.

2. Cell-free layer (CFL) formation in microcirculation

2.1 Principle mechanism of CFL formation

The formation of a CFL is a prominent hemodynamic feature in microcirculation. The layer formation is attributed to axial migration of the cells toward flow center [39, 51, 71]. The axial migration is promoted by "tank-treading" motion which arises from both compressive and tensile forces acting on the cell membrane under shear flow [71]. Owing to deformable membrane of the RBC, the tank-treading motion promotes cell migration more dominantly than tumbling motion which is commonly observed with solid particles under shear flow [1]. The cell migration due to the tank-treading motion consequently leads to phase separation of blood into CFL adjacent to the vessel wall and RBCs rich core in the flow center [39, 71]. Thus, the layer width is defined as the distance between the outermost edge of RBC core and the luminal surface of the endothelium (Figure I-5).

2.2 Physical and rheological factors influencing CFL width

The CFL width is influenced by physical and rheological factors such as hematocrit, RBC deformability and aggregability, vessel diameter, and flow rate [65, 71, 115, 116]. It has been qualitatively known that (a) the CFL width increases with the increase in the vessel diameter, (b) the CFL would also increase as hematocrit decreases, (c) impaired RBCs deformability decreases the CFL width, and (d) higher aggregation tendency enhances the CFL width [71]. It has also been confirmed under *in vivo* experimental conditions that the CFL width in the arterioles of the rat cremaster muscle can be

enhanced by RBC aggregation and flow reduction [84]. In addition, the elasticity of microvessels influences the CFL width in which relatively thicker CFL widths can be formed in elastic vessels rather than in hardened vessels [66].

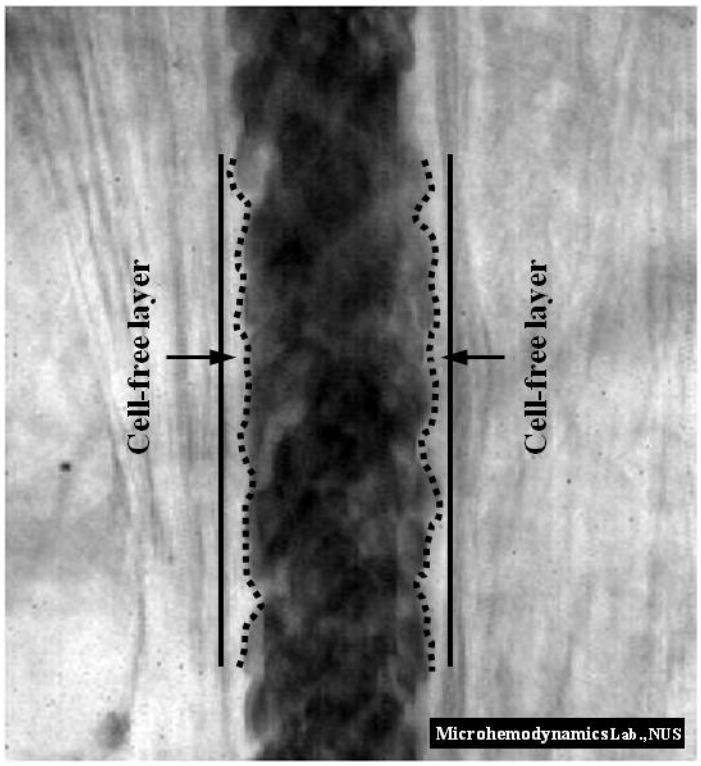

Figure I-5: Typical example of a cell-free layer in arteriole (ID = 55μm).
The solid line and dashed line indicate luminal vessel wall and outer edge of RBC core, respectively.

2.3 Physiological implication of CFL

It has long been established that the CFL plays a lubricating role by reducing the friction between RBC core and the tube wall in vertical micro-glass tubes [2, 28]. Alternatively, the CFL can be a diffusion barrier to nitric oxide (NO) scavenging by RBCs as well as oxygen delivery from the cells to tissue [18, 22, 34, 58, 119]. Many computational approaches have been employed to predict the effect of the CFL on the NO profiles by varying the CFL width. These predictions showed that the CFL can inhibit the scavenging of NO by RBCs, which leads to higher tendency of NO diffusion to the tissue [57]. The inhibition effect of the CFL on NO scavenging greatly influences NO bioavailability in tissue and this effect can offset the increase in NO scavenging rate due to the increase in core hematocrit by the CFL [57].

In addition, a thicker CFL may attenuate wall shear stress (WSS) by reducing the effective viscosity of blood, which in turn leads to lower nitric oxide (NO) production by the endothelium [122]. A previous theoretical study [109] suggested that the WSS may be influenced by a dynamic change of the CFL. Although rheological significance of the CFL in microvessels has been emphasized, only limited information on the CFL in microcirculation is available due to the lack of conventional measurement technique and the complexity of the vascular network *in vivo*.

As described above, many *in vitro* and *in vivo* studies have emphasized that the CFL may be an important determinant of blood flow. In particular, its impact on blood circulation would be more significant in micro-blood flow than in macro-blood flowsince the ratio of CFL width to vessel (or tube) diameter becomes greater as the vessel diameter

decreases. Therefore, providing detailed information on the CFL characteristics and its effect in microcirculation is essential for better understanding of the hemodynamic response to the functional alteration of microcirculatory vessels.

3. Overview of dissertation

This dissertation aims to provide the detailed insight into rheological aspect of CFL in micro-blood flows. CHAPTER I covers the literature review on the CFL and its physiological significance (Figure I-6). In CHAPTER II, conventional methods for the CFL measurement are reviewed and their limitations are discussed. A comparative study of four different histogram-based thresholding algorithms (Otsu's, intermodes, minimum and 2nd peak) for improvement of the CFL measurement accuracy is included (Figure I-7). In CHAPTER III, *in vitro* experiments performed by perfusing RBCs in a circular microtube with 25-μm diameter to provide the detailed insight into the dynamic changes of the CFL width and its relation to RBC aggregation at both physiological and pathophysiological levels are described (Figure I-8). In CHAPTER IV, currently available computational approaches for prediction of the CFL width are reviewed and their limitations are discussed. *In vitro* experiments and numerical model development for the CFL width prediction are discussed (Figure I-9). In CHAPTER V, relation between WSS and CFL width are discussed. Finally, the hypothesis that the variation of CFL width would increase WSS is examined (Figure I-10).

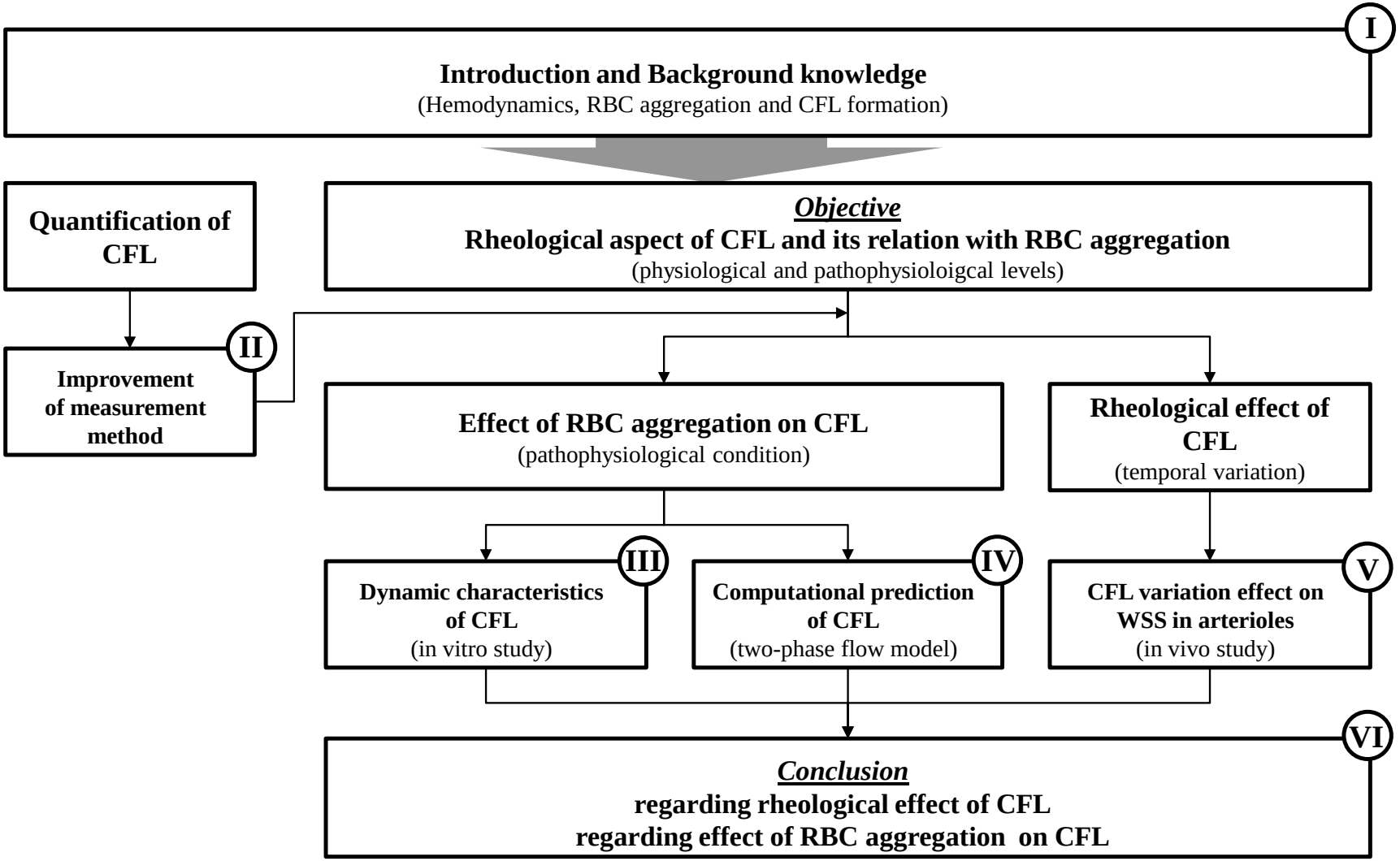

Figure I-6: Overall flow chart of the dissertation.

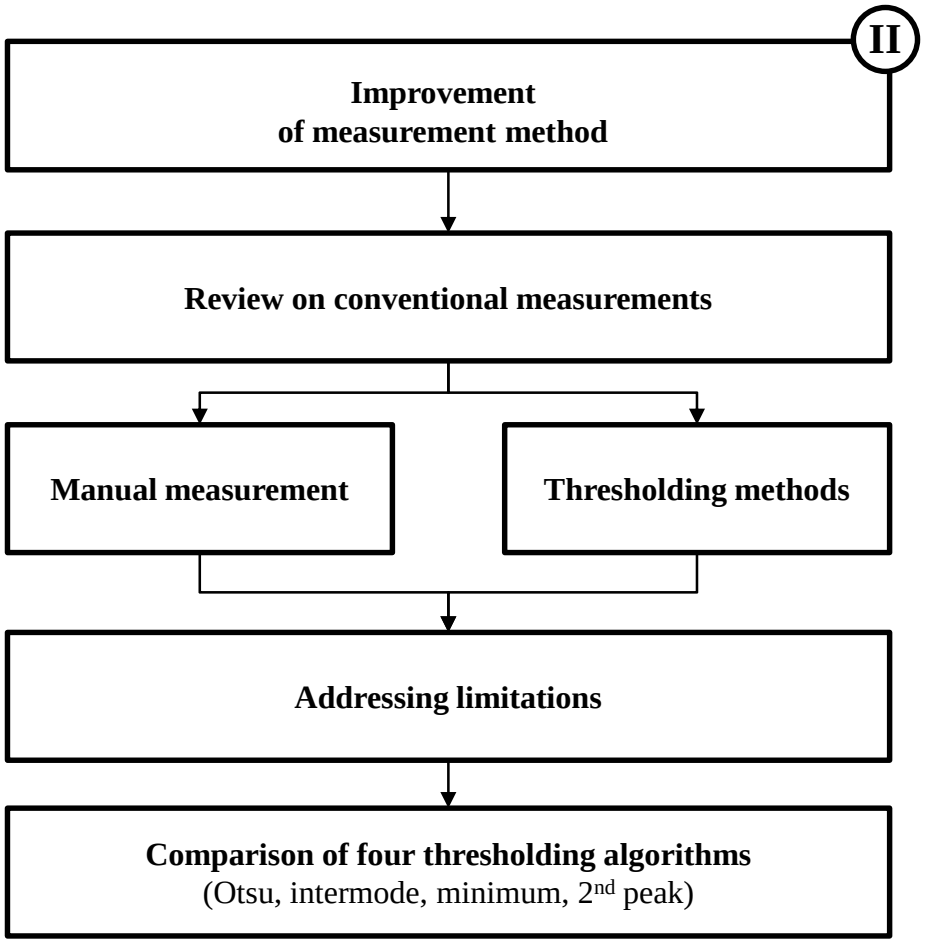

Figure I-7: Flow chart of CHAPTER II.

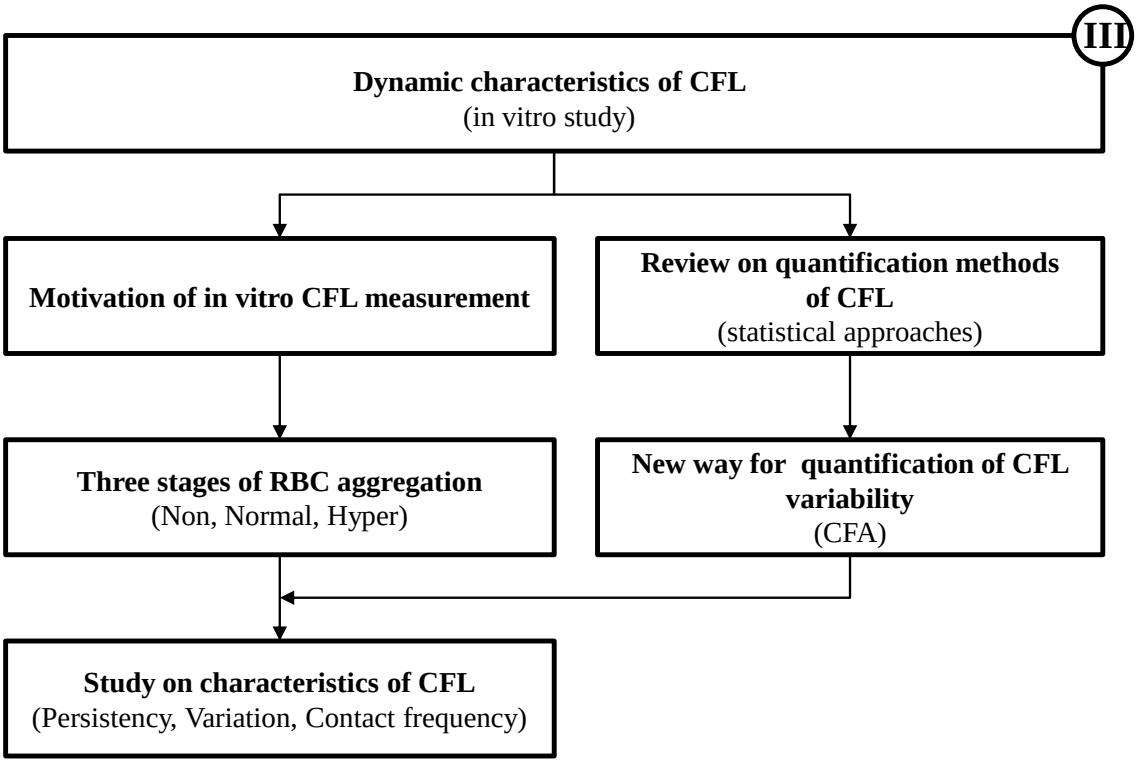

Figure I-8: Flow chart of CHAPTER III.

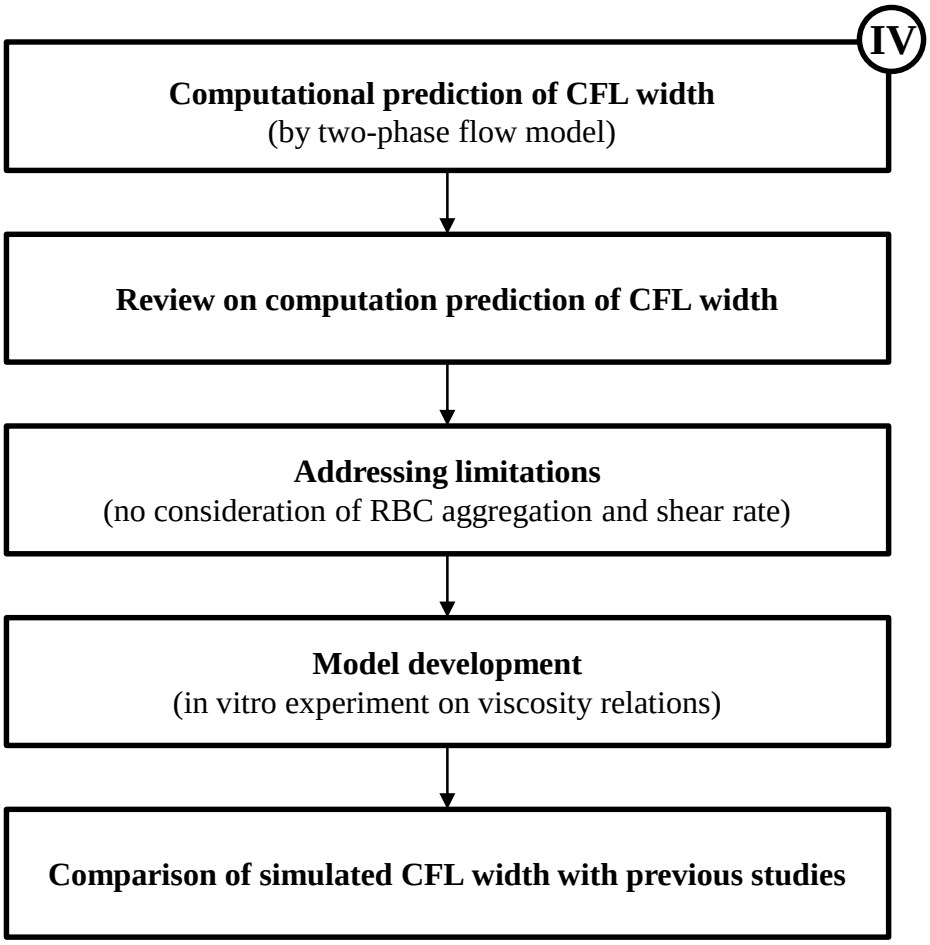

Figure I-9: Flow chart of CHAPTER IV.

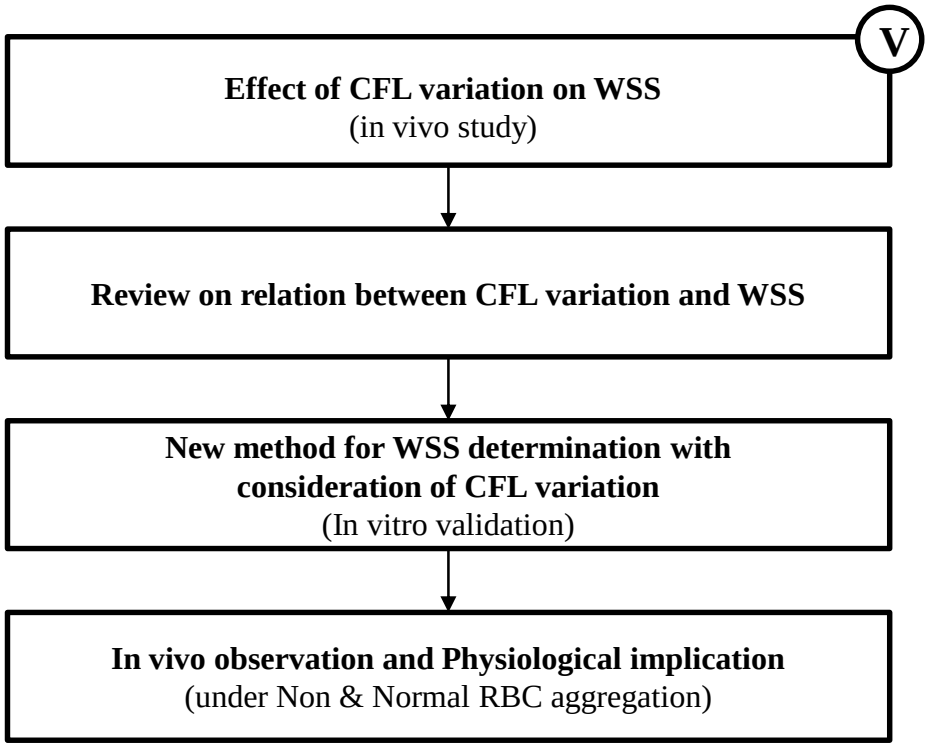

Figure I-10: Flow chart of CHAPTER V.

CHAPTER II: A COMPARATIVE STUDY OF HISTOGRAM-BASED THRESHOLDING METHOD FOR DETERMINATION OF CELL-FREE LAYER WIDTH IN SMALL BLOOD VESSELS

1. Introduction

A number of studies have been carried out to quantify spatial or temporal variations of CFL. However, previous method determining the layer width mainly relied on manual measurements with limited frame rate of the video image and/or digital images from microscopy [66, 112, 116]. Manual measurement is an extremely time-consuming process and may produce low consistency of measurement due to the human error. Furthermore, to obtain substantial data on spatial and temporal variations of the layer, a rapid succession of measurements is essential at a single or multiple sites [51].

To overcome these limitations, a recent study proposed a simple but effective way of separating the objective from other background using a thresholding method [49]. The thresholding algorithm provides consistency and automation of the measurement. It greatly reduces the human measurement error and makes the measurement less time-consuming. However, the automated method also has a drawback that the measurement accuracy may be dependent upon selection of a thresholding method. In earlier studies [49, 50], the Otsu's method have been used to determine the threshold level for the measurement of CFL width. However, as previous studies [55, 96] pointed out, this algorithm may break down when the sizes of object and background are unequal.

2. Motivation and Purpose

Since the importance of the CFL in the microcirculatory network was noted, the detailed information of the layer is essential to better understand its influence in the microcirculation.

- Previous studies have relied on the manual measurement which is time-consuming and has potential human error.
- Although image thresholding based measurement greatly reduces the measurement time, previous algorithm (Otsu's method) may not be a universal method.

Therefore, the present study aimed to examine several appropriate thresholding methods and propose the best suitable algorithm depending on the experimental conditions. To achieve this, we compared four different algorithms (Otsu, intermodes, minimum, and 2^{nd} peak methods) which have been widely used for their simplicity, easy implementation, and high-speed processing [96, 108]. The suggested process in this chapter may provide crucial information on selection of an appropriate thresholding method for the automated determination of the cell-free layer width.

In the following section, materials and method for *in vivo* experiment is described and a detailed procedure for measuring the CFL width from the experiment is presented. The results and discussion section compares obtained CFL widths by using the thresholding algorithms and discusses the measurement accuracy of each method.

3. Materials and Methods

3.1 Animal preparation and experimental procedure

Animal handling and all procedures were provided according to the Guide for the Care and Use of Laboratory Animals (Institute for Laboratory Animal Research, National Research Council, Washington, DC: National Academy Press, 1996) and approved by the local Animal Subjects Committee. In this study, two arterioles (ID 43 and 45 μm) and two venules (ID 50 and 67 μm) in the cremaster muscles from Wistar-Furth rats were used for CFL width measurements. For better performance of the measurement analysis, an unbranched area with stable flow, clear focus, and good image contrast was selected. An intravital microscope (Ortholux II, Leitz) was used with a 40X water-immersion objective (Olympus) and a long working distance condenser (Instec, Boulder, CO), which has numerical apertures of 0.7 and 0.35, respectively. A narrow bandwidth blue filter with peak transmission at 400 nm (Spectra Physics, no. 59820) was used to enhance the contrast between the RBCs core and tissue background field, and a high-speed video camera (FASTCAM ultima SE, Photron USA) was utilized to record microvascular flows for one second at 4500 frames/s. The detailed information on the animal preparation and measurement procedure is available in Appendix A.

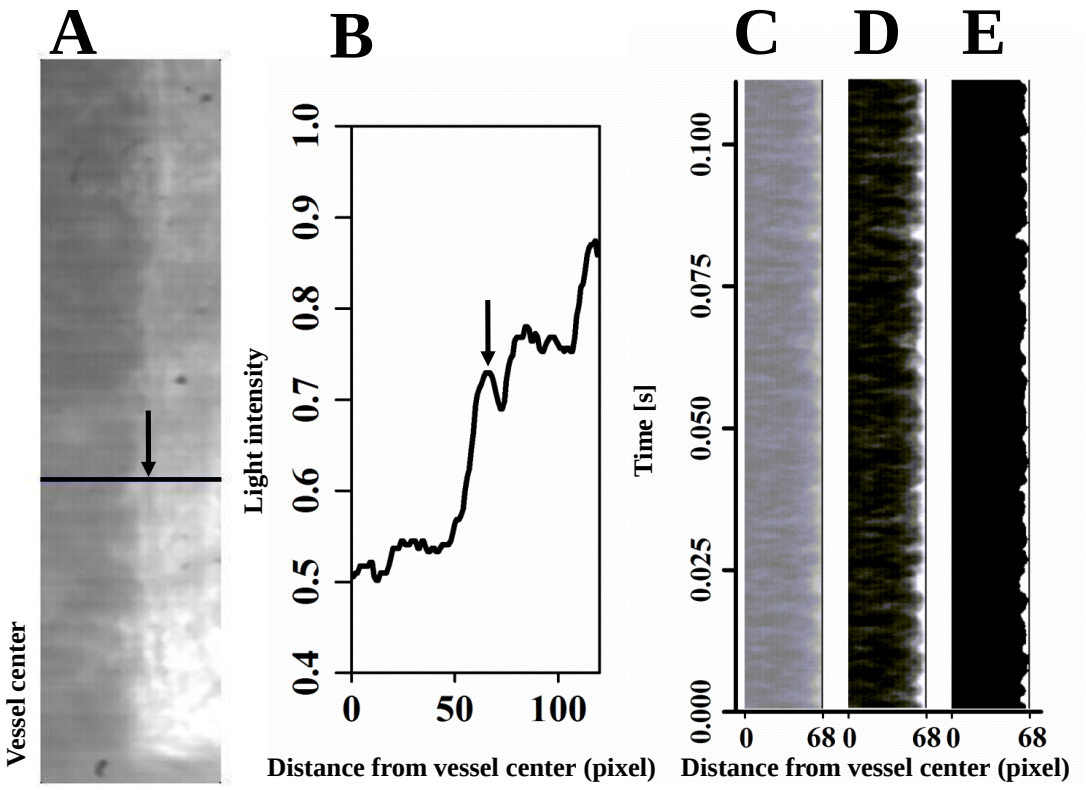

Figure II-1: Digital image analysis for determination of the CFL width.
A: An image of RBC flow in an arteriole (ID 43 μm). B: Intensity profile of the analysis line for determination of the vessel wall location (horizontal axis: distance from vessel center, vertical axis: light intensity). C: Grayscale image after reconstruction for 0.11 s which corresponds to the stacked image from 500 frames. D: Contrast enhanced image. E: Binary image by the minimum method. Arrows in A and B and solid line in C, D, and E indicate the vessel wall location.

3.2 Image analysis

The digital image processing procedure was performed with a commercially available image processing software package (MATLAB, Mathworks, Natick, MA). Uncompressed format video was recorded with the high speed camera mounted on microscope and then extracted into grayscale images (BMP format) with 640 x 480 resolutions. All extracted images were filtered with a median filter to remove "Salt and Pepper" noise which represents randomly occurring white and black pixels due to electrical interface interruption during acquisition or transmission [21]. To obtain time-dependent variation of CFL width, an analysis line was drawn across the vessel and its spatial location was determined where the vessel wall can be clearly distinguishable from the background (Figure II-1A). The arrow in Figure II-1B indicates the location of the inner vessel wall defined by the criterion for the determination of the vessel wall as reported in a previous study [49]. The initial peak of the light intensity that transits from dark to light over two pixels was considered as the inner vessel wall. Intensity values along the analysis line were stored into a 1-D image matrix, and the matrices were reconstructed by stacking over consecutive 4500 frames. Thus, the reconstructed image has a 2-D image matrix, with each row representing the line intensity data for one frame. Figure II-1C shows the typical example of reconstructed image taken from 500 frames which corresponds to the time period of 0.11 s. After reconstruction, the contrast of the stacked image was digitally enhanced by using the software. Although the optical blue filter was also used to enhance the contrast between the RBC core and background, the actual contrast of the captured image was not always sufficient to properly distinguish the RBC core from the background. Hence, digital image contrast adjustment was carried

out to further enhance the contrast (Figure II-1D). These stacks of enhanced images were then binalized by a thresholding method for the automated determination of the CFL width (Figure II-1E). Although 4500 intensity line data were obtained for 1 s on each vessel, only 46 of these data were used for comparison with the manual method by selecting every 100th frame due to the limitation as indicated in "*Manual measurement"* section below.

3.3 Thresholding algorithms

Four histogram-based thresholding algorithms were considered, which include the minimum [90], intermodes [90], 2nd peak detection [107], and Otsu's algorithm [49, 85]. All the images would be expected to have a bimodal histogram. The bimodal histogram could be achieved by iteratively smoothing the histogram using the three-point mean filter until the histogram had only two local maxima [38]. The threshold level of the minimum method is determined by the valley of the histogram which represents the local minimum between two peaks of the histogram. The intermodes method is determined by averaging the 1st and 2nd peaks of the histogram. The second local maximum is used as the threshold level of 2nd peak method. The Otsu's method provides the optimal threshold level that maximizes the class variance between the object and background. All proposed thresholding algorithms were based on obtaining a global threshold level that can be used to convert an intensity image to a binary image. All intensity values higher than the threshold level were converted to 1 (white pixel) whereas those of smaller values were

converted to 0 (black pixel). This process produces a binary image that can be used for the image segmentation.

After binalizing the stacked gray level image, the CFL and RBC core were represented by the white and black pixels, respectively. Along the first row of the binary image, the number of white pixels was counted starting from the first pixel from either vessel wall location until a black pixel was encountered. The counted pixels from either vessel wall represent the distance (cell-free layer width in the number of pixels) from each inner wall location to the RBC core at a particular time point. The actual layer width (in μm) was then obtained by multiplying with a calibration factor (0.3125 μm/pixel). This procedure was repeated for the remaining rows to obtain temporal information of the layer width.

3.4 Manual measurement

To validate the automated determination of the CFL width, manual measurement was considered as the reference. All the CFL width measurements obtained with the four thresholding algorithms were compared with the manual measurement. The manual measurement was taken by three individuals to reduce the human measurement error. A total of nine measurements (three times by each individual) on each blood vessel were averaged and the mean value was used for the comparison with the thresholding methods. Since the manual measurement is extremely time consuming, only 46 frames were used for the measurement, which were taken from a total of 4500 frames by choosing every 100th frames. Contrast enhanced image (Figure II-1D) was used for all the

measurements with the manual and thresholding methods since the enhanced contrast image provided a more distinct edge of the RBC core, which allows the performer to detect the edge with greater ease.

3.5 Statistical analysis

Linear regression was performed with a commercial statistical software package (Prism 4.0, GraphPad). The Bland-Altman analysis was performed to compare measurements obtained between two different methods (manual and thresholding). Unpaired t-tests were used to compare measurements taken by the manual and automated methods.

4. Results and Discussion

Typical results acquired in an arteriole (ID 43 μm) are shown here. Figure II-2 shows the CFL width results obtained with the manual and automated methods. With our current microscopic system, the minimum algorithm (Figure II-2C) showed the best fit with the manual measurement as compared to the other algorithms. The 2nd peak algorithm (Figure II-2D) produced relatively good results. However, it seemed to slightly underestimate the CFL width since all the determined values were consistently lower than those measured manually. In contrast, the other two methods, the Otsu's algorithm (Figure II-2A) and intermodes algorithm (Figure II-2B), considerably overestimated the CFL width in comparison with values determined by the manual measurements. As can be seen in Table II-1, all the results obtained in the four different vessels (two arterioles and two venules) seemed to be consistent.

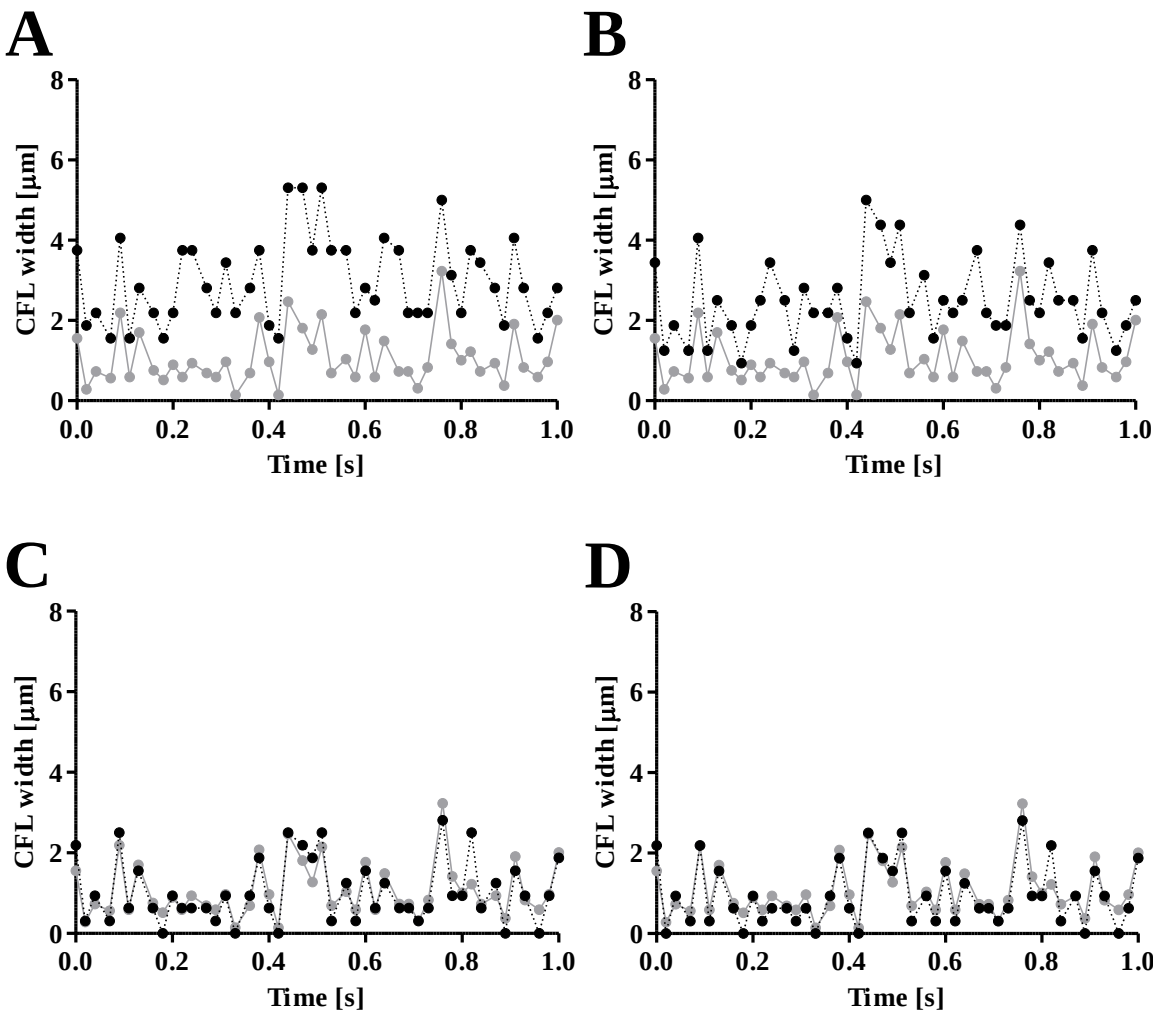

Figure II-2: CFL width data determined by automated and manual methods.
A: Otsu's method. B: Intermodes method. C: Minimum method. D: 2nd peak method. Black symbols represent automated measurements while gray symbols indicate manual measurements.

Table II-1: Comparison between manual and automated methods for CFL width determination

Methods	Arteriole		Venule	
	43 μm	45 μm	50 μm	67 μm
Manual	1.07 ± 0.67	0.46 ± 0.38	2.02 ± 0.27	1.57 ± 0.88
Otsu	2.97 ± 1.06***	3.21 ± 0.92***	3.02 ± 0.58***	3.61 ± 0.77***
Intermodes	2.48 ± 1.00***	2.11 ± 0.72***	2.68 ± 0.56***	2.67 ± 0.84***
Minimum	1.03 ± 0.79	0.39 ± 0.39	1.83 ± 0.31**	1.37 ± 0.93
2nd peak	0.94 ± 0.78	0.29 ± 0.35*	1.00 ± 0.75***	0.67 + 0.88***

* $P < 0.05$, ** $P < 0.005$, *** $P < 0.0001$

The Bland-Altman analysis (Figure II-3) was further used for a detailed statistical comparison of the CFL width data shown in Figure II-2. The bias was determined by subtracting the values of the manually measured CFL width data from the corresponding width data determined by the automated methods. Hence, any positive or negative value represents either overestimation or underestimation of the automated measurements, respectively. As shown in Figure II-3, the minimum algorithm (Figure II-3C) resulted in the closest measurements to the layer width values measured manually in comparison with the other methods, with a mean bias of -0.04 ± 0.34 μm. The 2nd peak algorithm (Figure II-3D) showed slight underestimation of the layer width (-0.13 ± 0.29 μm). In contrast, the other two algorithms overestimated the width, with Otsu's algorithm (Figure II-3A) giving a mean bias of 1.90 ± 0.71 μm and the intermodes algorithm (Figure II-3B) giving a mean bias of 1.41 ± 0.64 μm respectively. Figure II-4 shows the linear regression curve for comparison between the manual and automated measurements. The minimum algorithm shows the closest slope (1.062) to the unity, and the closest intercept (-0.104) to zero. This result also confirmed that the minimum algorithm provided the best agreement with manual measurement.

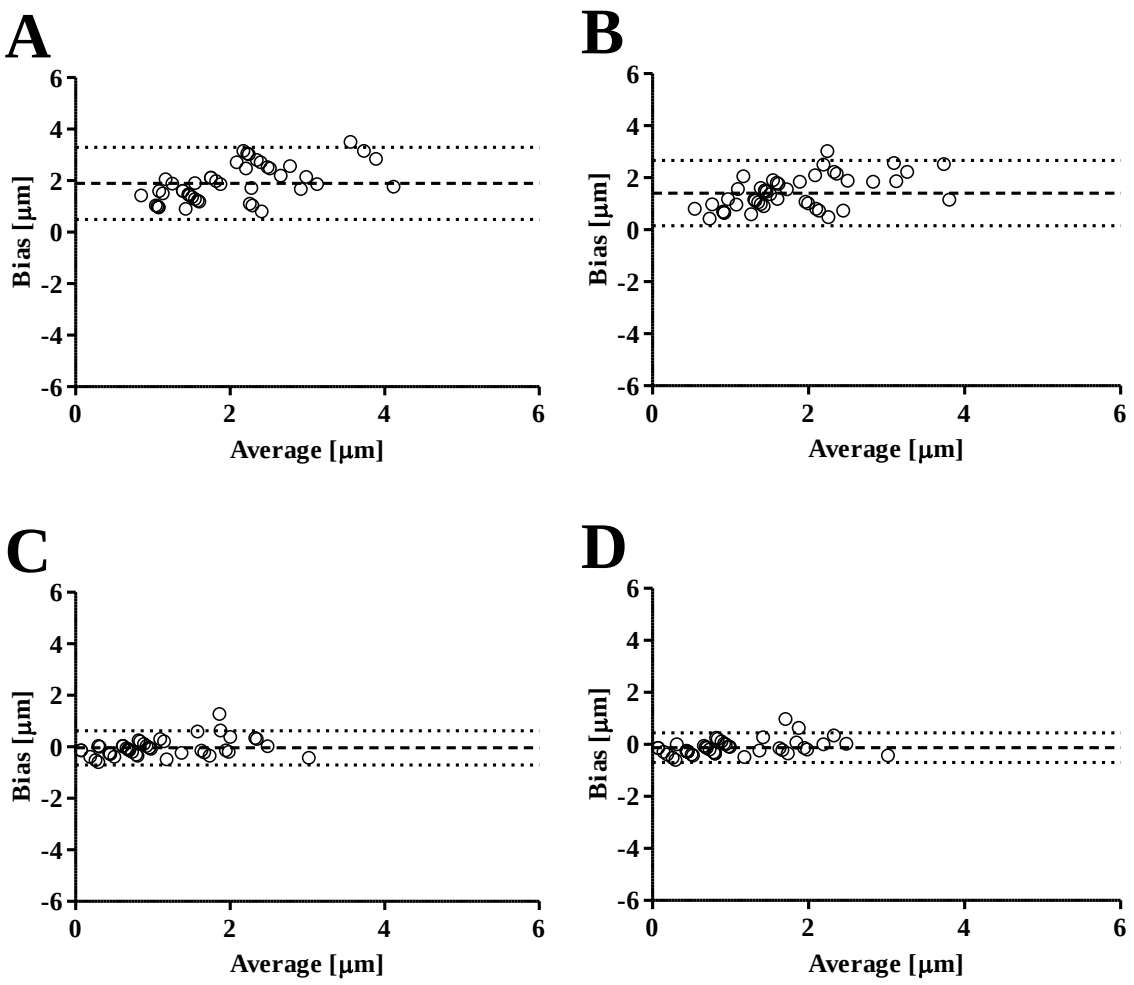

Figure II-3: The Bland-Altman analyses for comparison of automated and manual measurements.
A: Otsu's method. B: Intermodes method. C: Minimum method. D: 2nd peak method. Bold dashed lines represent the mean bias while dotted lines indicate 95% confidence limits of the bias.

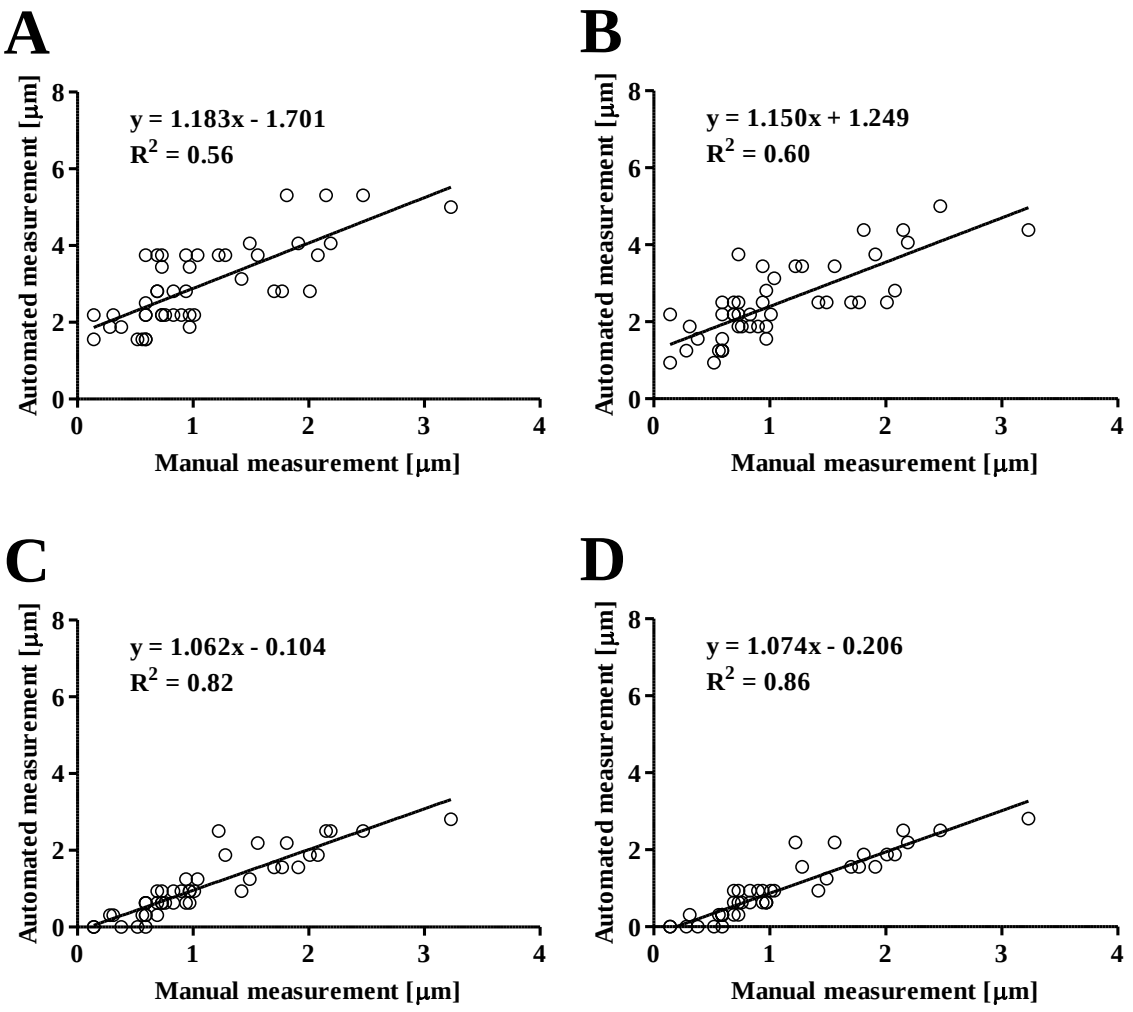

Figure II-4: Linear regression for comparison between automated and manual measurements.
A: Otsu's method. B: Intermodes method. C: Minimum method. D: 2nd peak method.

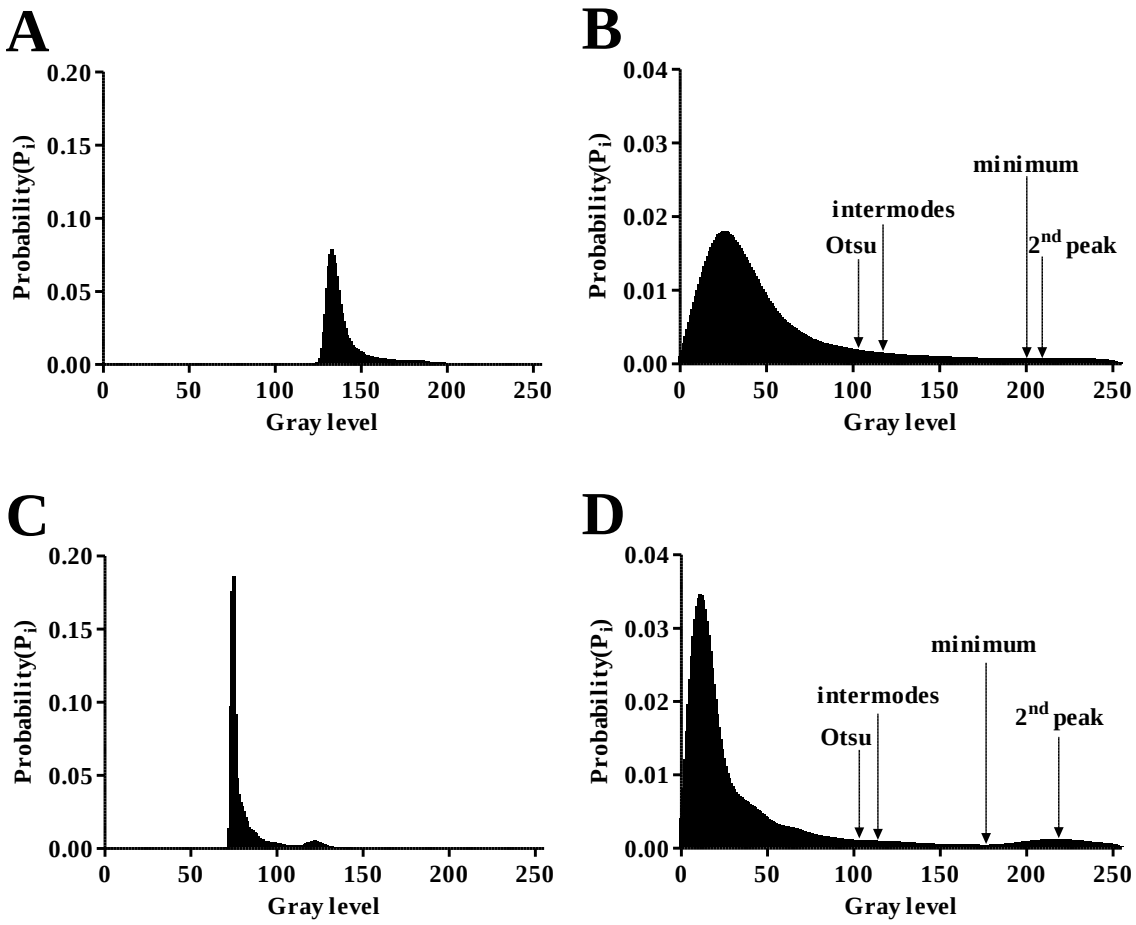

Figure II-5: Probability distribution (normalized histogram) of stacked image.
In a 43-μm arteriole (CFL width ≈ 1 μm), A: before contrast enhancement. B: after contrast enhancement. In a 50-μm venule (CFL width ≈ 2 μm), C: before contrast enhancement. D: after contrast enhancement. Arrows represent the threshold levels determined by the four algorithms.

To better understand how the thresholding levels are determined by the automated algorithms, the probability distribution (normalized gray-level histogram) is shown in Figure II-5. The probability can be calculated as follows:

$$P_i = n_i / N, \quad P_i \geq 0, \quad \sum_{i=0}^{L} P_i = 1 \tag{1}$$

where the L is gray levels (0 – 255), the number of pixels at gray level i is denoted by n_i, and total number of pixels in an image by N. As shown in Figure II-5A, the probability distribution may not have a distinct bimodal shape when the class of the prospective CFL (higher gray levels) was relatively smaller than that of the unwanted background (lower gray levels). This class imbalance between the higher and lower gray level regions reflected that the contrast of the image was not high enough to enable clear distinction between the CFL and RBC core. By digitally enhancing the contrast of the image, we managed to transform the bimodal probability distribution into one with a broader valley and reduced peak values. However, it is important to note that despite this enhancement, the class imbalance still existed.

The minimum algorithm finds the threshold level where the probability is a minimum in the normalized gray-level histogram which appears to lie in between the 1st and 2nd peaks but closer to the 2nd peak than the 1st peak. Under the circumstance shown in Figure II-5B, the intermodes algorithm would provide a lower threshold level than the minimum algorithm since the intermodes algorithm determines the threshold level based on the averaged value of the two local maxima. In contrast, the thresholding level of the 2nd peak algorithm is expected to be relatively higher than that of the minimum algorithm since the 2nd class is narrow and close to the maximal gray level (L_{max} = 255). Despite

the fact that Otsu's thresholding algorithm has been accepted as one of the most referenced thresholding algorithms, it may not provide a suitable optimized threshold level when an image has unequal local maxima or a broad and flat valley of the class like the case shown in Figure II-5B [60]. Since the Otsu's algorithm is based on maximizing the separability of the two classes, extremely unequal variance of the classes may cause a tendency of the threshold level to be located closer to a peak with larger population of probability [55, 96]. Thus in this study, the threshold level determined by the Otsu's algorithm consistently overestimated the CFL width compared with the results obtained manually. However, when the CFL is relatively thick, as shown in Figure II-5C and 5D, two peaks in the distribution can easily be identified. Thus, it is important to note that the Otsu's and intermodes methods would provide threshold levels similar to that determined by the minimum method when the image has two local maxima with similar shapes. Although the candidate algorithms examined in the present study were straightforward, they have advantages such as fast processing and easy implementation, which can be useful for on-line *in vivo* measurements.

CHAPTER III: CHARACTERISTIC CHANGES OF CELL-FREE LAYER WIDTH BY ERYTHROCYTE AGGREGATION IN A 25-μm TUBE

1. Introduction

As highlighted in many previous studies, the RBC aggregation is an important diagnostic parameter that is highly correlated with an inflammatory state [3], and is clinically relevant to human diseases including sepsis [11], hypertension [98], diabetes mellitus [26], and HIV [48]. However, the effect of RBC aggregation at its pathological levels on the dynamic changes of the CFL width is not fully understood. Previous *in vivo* studies [50, 83, 84] have provided information on the CFL width and its temporal variation at a specific location with use of an analysis line over a time period.

2. Motivation and Purpose

Although the time-dependent CFL width variation at the location of the analysis line was analyzed in the previous studies, the information was limited to the characteristic of the CFL in time domain. In addition, simple statistical analyses such as mean width of CFL and its standard deviation would be insufficient to fully describe the dynamic changes of CFL width since the CFL width varies spatially and temporally.

Therefore, the present study aims to provide the detailed insight into the dynamic changes of the CFL width and its relation to the RBC aggregation. *In vitro* experiments were performed by perfusing human RBCs in a circular micro-tube with diameter of 25

μm. The CFL in both spatial and temporal domains were obtained by adopting various analysis techniques. To better understand the effect of RBC aggregation on the CFL characteristics, the experiments were carried out at both physiological and pathological levels of RBC aggregation seen in humans.

In the following section, materials and method for *in vitro* experiment are described and detailed procedures for the quantification of CFL variation are presented. The results and discussion section covers the effect of RBC aggregation on the CFL formation.

3. Materials and Methods

3.1 Blood sample preparation

Human blood containing 7.5% K_2EDTA (I-DNA Biotechnology, Singapore) was centrifuged (Sigma 2-6, Goettingen, Germany) and washed with Phosphate Buffer Saline (PBS, Hanks). The buffy coat was gently removed after centrifugation and the blood sample was washed three times more before collecting red blood cells (RBCs). The levels of RBC aggregation in terms of M index given by the Myrenne aggregometer (Roentgen, Germany) were adjusted to physiological (M = 12-16) and pathological (M > 20) levels seen in humans [52, 83] by resuspending the RBCs in dextran-PBS solutions. Dextran 500 (average molecular mass of 460 kDa, Sigma) was dissolved in PBS at desired concentrations of 7.5 and 12.5 mg/ml for the physiological and pathological aggregating conditions, respectively. For non-aggregating conditions (M = 0.0), no dextran was used. Hematocrit of the blood samples was adjusted to be ~40%.

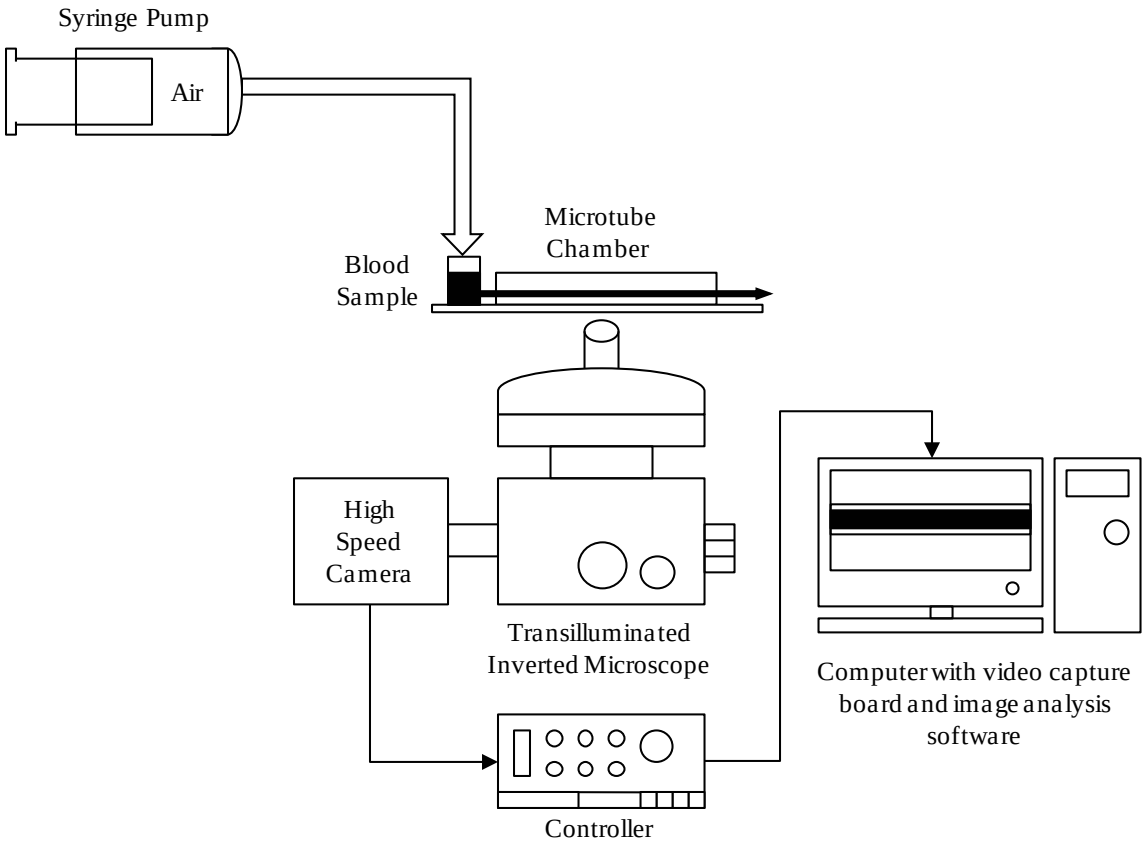

Figure III-1: Schematic diagram of experimental setup.

3.2 Experimental setup

Figure III-1 shows the schematic diagram of our experimental setup. A micro-tube (Hirakawa Hewtech, Ibaraki, Japan) with inner diameter of 25 μm and length of 150 mm was assembled with a chamber that consists of top and bottom acrylic plates (thickness = 1 mm) with a sealing rubber frame, and one end of the tube was connected to a reservoir. The tube was completely immersed in the distilled water inside the chamber which was placed horizontally on the stage of an inverted microscope (IX71, Olympus, Japan) with a 40X objective (UPlanSApo 40x, Olympus, Japan) and a long working distance condenser (WI-UCD, Olympus, Japan). The microtube was pre-flushed with autologous plasma to minimize adhesion of RBCs to the inner surface of the tube. A polytetrafluoroethylene (PTFF) coated small magnetic stirring bar (2 x 2 mm, Big Science Inc. USA) was used in the reservoir to prevent RBC sedimentation. A syringe pump (KDS 210, Holliston, USA) was used to control flow rates. The detailed description of the flow chamber can be found in a previous study [104]. The blood flow in the tube was recorded with a high-speed video camera (FASTCAM 1024PCI, Photron, USA) at 3000 frame/s for 1 s with a resolution of 512 x 512 pixels. A blue filter (B-390, HOYA, Japan) with peak transmittance at 394 ± 4 nm and spectral bandpass of 310-510 nm was used to enhance the contrast between RBCs and background. Seven experiments per each aggregating condition were performed at room temperature of 21 ℃.

3.3 CFL width and edge velocity measurement

The CFL width is defined by the distance from outermost edge of the RBC core to inner tubular wall. The detailed description of the layer width measurement can be found in the CHAPTER II. The spatial resolution of the layer width measurement in the present study was ~0.5 μm. The edge velocity (V_{edge}) of the RBC core was obtained by manually tracking the outermost cells across 10 digitalized frames [49]. Using the syringe pump, V_{edge} was adjusted to be ~2.7 mm/s which is similar to that used to simulate pathological flow conditions in our previous arteriolar flow studies [83].

3.4 Persistency of CFL

The persistency of the CFL pattern in downstream was characterized by using the cross-covariance which has commonly been used to find the similarity of two sequences. CFL data were obtained at two points along the length of the tube on each side. The first analysis line for the layer width measurement was established at a distance of ~80 mm from the inlet of the tube and considered as the baseline. The second analysis line was then placed at a distance 0.5D, 1.0D, 1.5D, or 2.0D from the baseline (0.0D) where D represents the inner diameter of the tube. The CFL width over a period of 1 s from each position of the second line was cross-correlated against the baseline measurement using the same software package (MATLAB). Based on this approach, the 3000 sequential variations of the CFL at each analysis line were treated as a time-dependent continuous signal. The correlation length (l) was determined as described by Silva and Intaglietta [111]. In brief, the correlation values were fitted by exponential equation of $y = e^{-kx}$.

The correlation length (l) is defined as the downstream distance from the baseline where the normalized correlation coefficient falls to $1/e$ (0.368).

3.5 Cell-free area (CFA) determination

To better illustrate the spatio-temporal variation of the CFL width, the CFA was determined in a particular region of interest (ROI). It was achieved by adopting image analysis techniques described in CHAPTER II. Blood flow in the ROI that has a length of $4.0D$ was cropped, and the cropped sequential images over the time period were then subjected to the minimum thresholding method to obtain binalized images. The CFA was determined by counting the number of pixels in the area with no RBCs near the tube wall, and it was normalized by the total area of the ROI.

3.6 Statistical analysis

All statistical comparisons were performed with a statistical software package (Prism 4.0, GraphPad). One-way ANOVA with Tukey's Post-Hoc test was used to determine significance of difference among the three different aggregating groups. All data are reported as means ± SD (standard deviation). For all statistical tests, $P < 0.05$ was considered to be statistically significant.

4. Results

4.1 Systemic parameters

The aggregation index (M) was 15.7 ± 1.3 and 24.6 ± 4.6 for physiological and pathological aggregating conditions respectively, whereas it was 0.0 for the non-aggregating condition. Hematocrit of all the blood samples was 40 ± 1%, and there was no significant difference among the aggregating conditions. The edge velocity (V_{edge}) was 2.7 ± 0.8, 2.7 ± 0.5 and 2.6 ± 0.4 mm/s for non-aggregating, normal-aggregating, and hyper-aggregating groups, respectively. There was no significant difference in V_{edge} among the three aggregating groups.

4.2 Effect of aggregation on mean and SD of the layer widths

Figure III-2 shows the mean width and standard deviation (SD) of the CFL in the three aggregating conditions. As shown in the Figure III-2A, the layer width became increased with elevating the aggregation level. The mean layer widths in the normal-aggregating and hyper-aggregating conditions were significantly larger ($P < 0.05$ and $P < 0.001$, respectively) than that in the non-aggregating condition. On the other hand, the SD of the CFL width appeared to be independent of the aggregation level (Figure III-2B). We found no significant difference in the SD among the different aggregating groups.

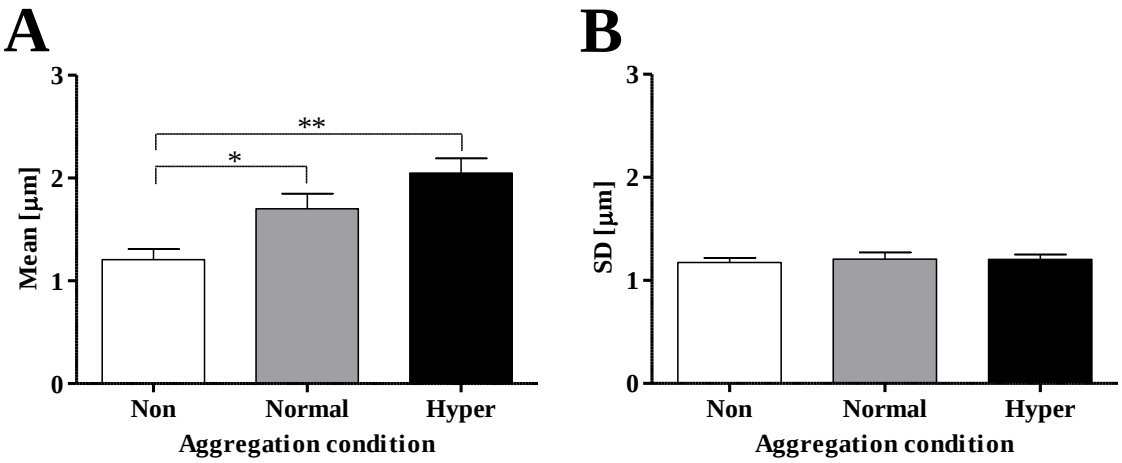

Figure III-2: Mean (A) and standard deviation (B) of the CFL width in different aggregating conditions.
SD represents standard deviation. * $P < 0.05$, ** $P < 0.001$

4.3 Persistency of the layer variation

The correlation length was used to examine the persistency of the CFL variation along downstream. No statistical difference was found between the non-aggregating (48.0 ± 5.5 μm) and normal-aggregating (47.2 ± 3.0 μm) conditions. Similarly, the correlation length in the hyper-aggregating (50.8 ± 5.0 μm) condition was not significantly different from that in either non-aggregating or normal-aggregating condition, confirming that aggregation has no effect on the persistency of CFL variation.

4.4 Effect of aggregation on RBC-wall contact frequency

Figure III-3A shows typical examples of RBC flow in a tube (ID = 25 μm) and an arteriole (ID = 31 μm) while the RBC-wall contact frequency results under the two different circumstances are shown in Figure III-3B. The CFL data obtained in the present study were compared with *in vivo* arteriolar data reported in our earlier study [83]. Ten sets of CFL data in small arterioles where the flow condition (V_{edge} = 2.7 ± 1.3 mm/s) is similar to those in the present study were used for the comparison.

Unlike the *in vivo* situation, in the present *in vitro* study, we observed a number of RBCs making contact with inner tube wall during the CFL measurements. To examine whether or not this RBC-wall contact can be influenced by the RBC aggregation, the number of zero values of the CFL width during its measurement (1 s) was compared under the three aggregating conditions. We assumed that the zero CFL width represents the instant contact between RBC and the tube wall. Figure III-3B shows the contact frequency results that were normalized by the total number of observations (3000 data).

The elevation in the aggregation level appeared to decrease the contact frequency. We found a significant decrease in the contact frequency under the normal-aggregating ($P < 0.01$) and hyper-aggregating ($P < 0.001$) conditions as compared with that in the non-aggregating condition in the current *in vitro* condition. On the other hand, the results obtained from our previous *in vivo* data showed no significant effect of aggregation on the contact frequency although a similar trend was apparent. Under all three aggregating conditions, the contact frequency in the *in vivo* condition was significantly smaller ($P < 0.05$) than that in the *in vitro* condition.

Figure III-3C compares normalized mean widths of CFL examined in this study (*in vitro*) and in our previous study (*in vivo*)[83]. The layer widths were normalized by radius of tube (or vessel). An increasing trend of the normalized CFL width due to aggregation was found in both cases. However, the *in vivo* CFL width was significantly greater ($P < 0.05$) than the *in vitro* CFL width in the same aggregating condition.

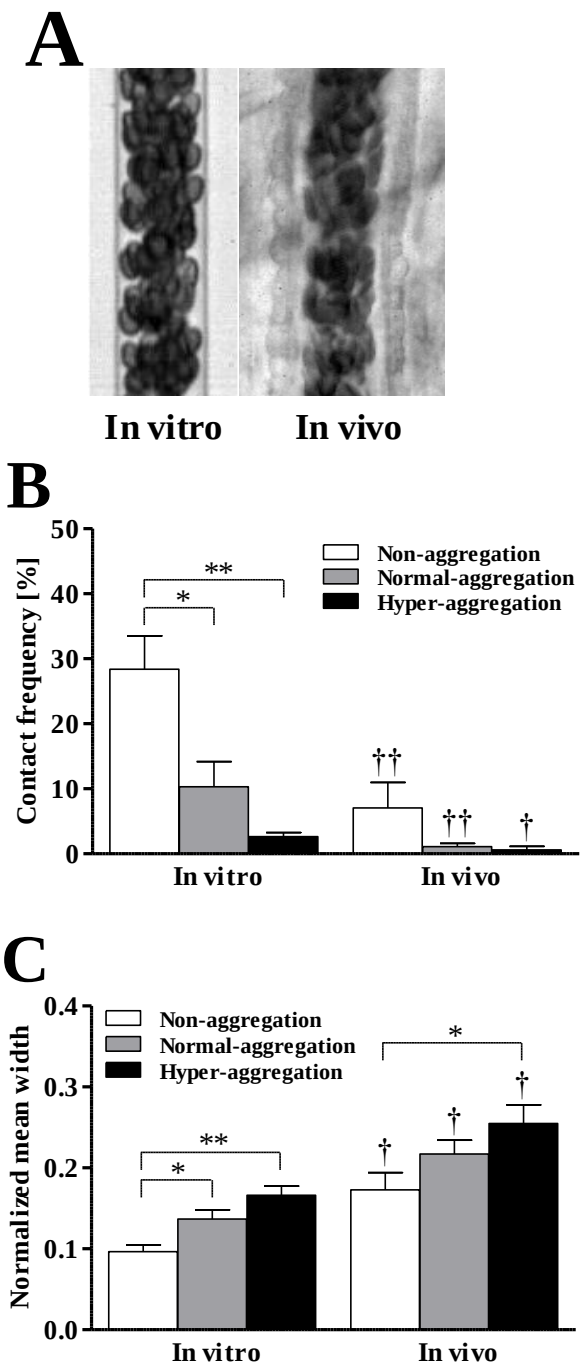

Figure III-3: Comparison of RBC-wall contact frequency between *in vitro* and *in vivo* conditions.
(A) shows typical examples of RBC flows under *in vitro* and *in vivo* conditions. **(B)** and **(C)** show the contact frequency and normalized mean layer width results for the three aggregating conditions, respectively.
* $P < 0.05$ and ** $P < 0.001$: statistical difference among aggregation groups. † $P < 0.05$ and †† $P < 0.01$: statistical difference between *in vitro* and *in vivo* data.

4.5 Effect of aggregation on CFA

Figure III-4A shows two-dimensional visualization of CFL formation at different time points. The figure illustrates two distinct regions (RBC core and CFA) in the ROI. The CFA varied with time and RBCs occasionally made contact with the tube wall. The CFA on each side of the wall (top and bottom) appeared to be asymmetric, thus the degree of asymmetry was examined by comparing the CFA on the two sides as follows:

$$\frac{\left|CFA_{top} - CFA_{bottom}\right|}{CFA_{top} + CFA_{bottom}} \times 100\% \quad (1)$$

The asymmetry of CFA seemed to decrease with elevating the aggregation level (non-aggregation:19.1% → normal: 15.2% → hyper: 14.7%), but no statistical difference was found (P = 0.36) (Fig. III-4B).

A typical example of time-dependent changes of the normalized-CFA (NCFA) over 1 s is shown in Fig. III-5A. The NCFA at higher levels of aggregation seemed greater than in lower aggregation levels (hyper > normal > none). However, the NCFA difference among the three aggregating conditions varied with time, thus all NCFAs were integrated over 1 s for better comparison (Fig. III-5B). The results showed that the mean NCFA in hyper-aggregating conditions were significantly greater than that in non-aggregating conditions (P < 0.01). Although no statistical difference was found between none and normal conditions or normal and hyper conditions, the mean NCFA seemed to increase with elevating the aggregation level.

To obtain more detailed information on the NCFA, probability of the NCFA was analyzed. Figure III-6A shows a typical example of the probability distribution of the

NCFA of which data correspond to those in Fig. III-5A, and definitions for the probability distribution is described in Fig. III-6B. As expected, the distribution was shifted to greater values as the aggregation level increased from none to hyper. All distributions did not follow the normal distribution. As shown in Fig. III-6C, both left and right tail widths from the mean NCFA appeared to have an increasing trend with elevating the aggregation level. However interestingly, there was a significant increase only in the right tail width in hyper-aggregating conditions compared to that in non-aggregating conditions ($P < 0.05$).

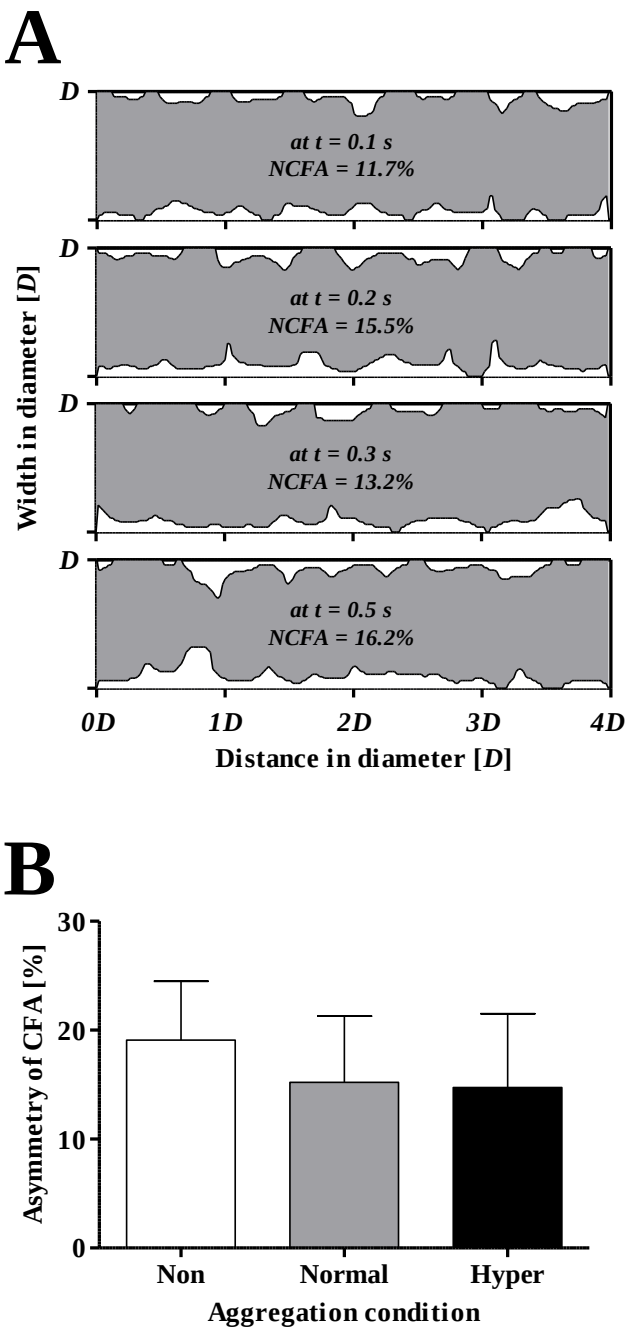

Figure III-4: (**A)** Two-dimensional visualization of CFA in a hyper-aggregating condition. Gray and white regions represent the RBC core and CFA, respectively. **(B)** Asymmetry of CFA on the two sides of the tube wall in three aggregating conditions.

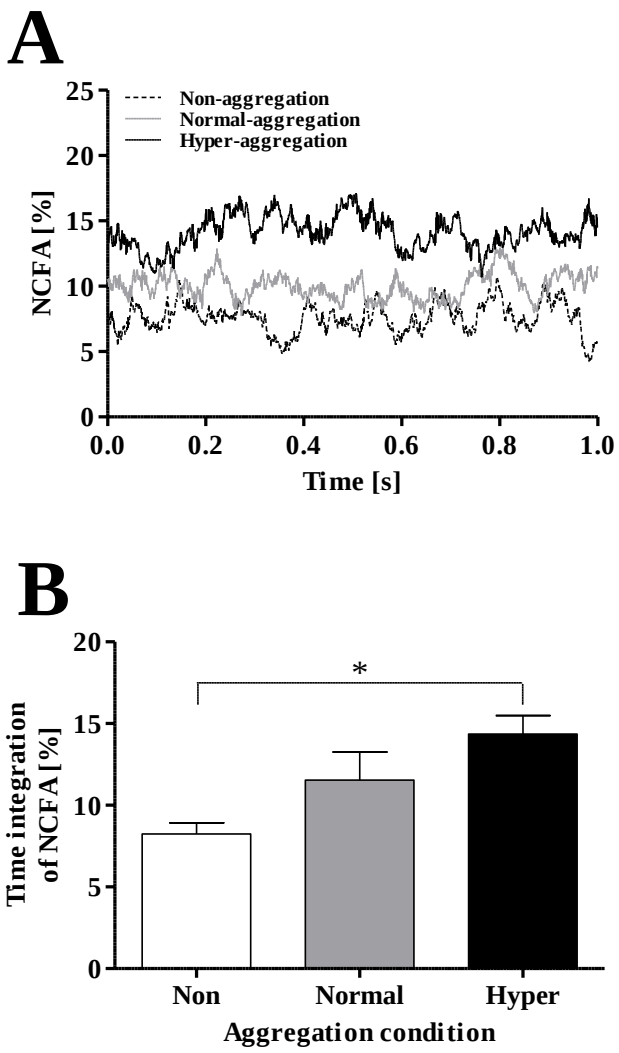

Figure III-5: (A): Time-dependent variation of NCFA in three aggregating conditions. **(B)**: Time integration of the NCFA over 1 s. $*P < 0.01$

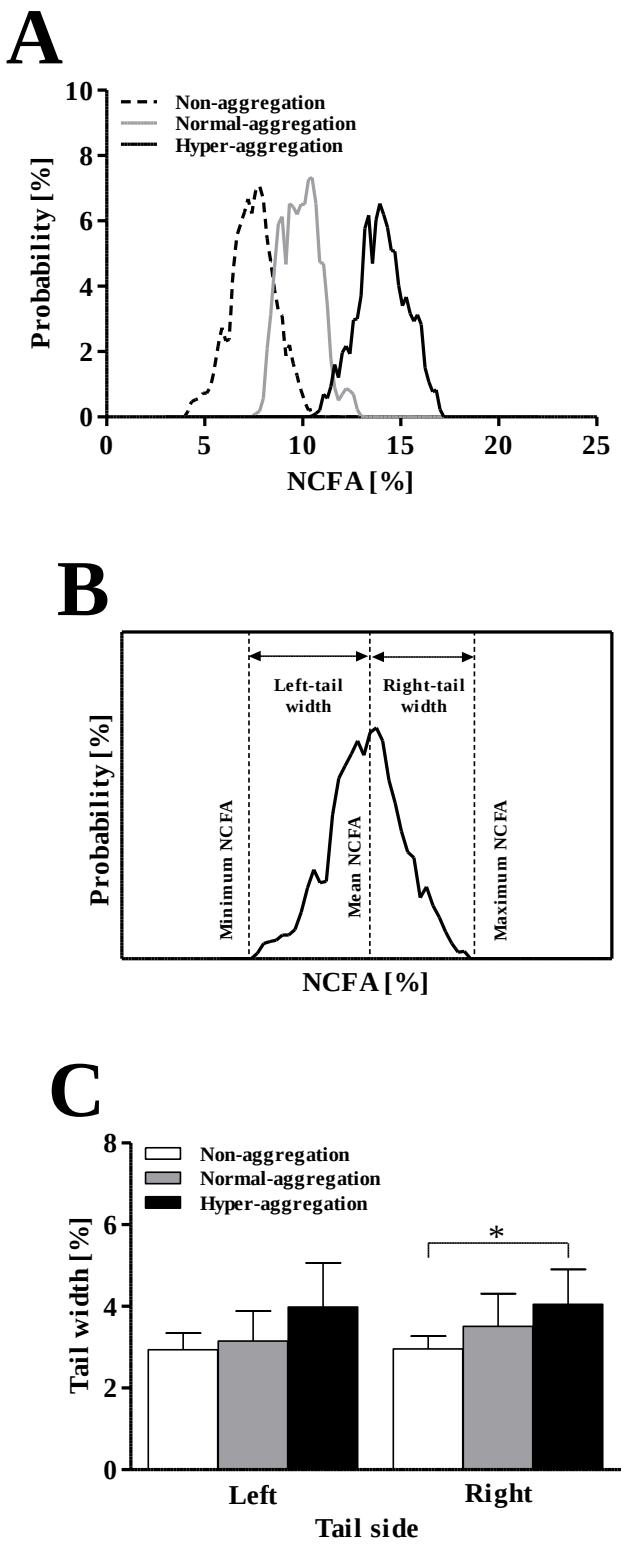

Figure III-6: (A): Probability distribution of NCFA obtained from the data shown in Fig. III-5A. **(B)**: Definition of left and right tail widths in the probability distribution. **(C)**: Aggregation effect on the left and right tail widths. * $P < 0.05$

5. Discussion

5.1 Effect of aggregation on the mean CFL width and its SD

The prominent increase in the CFL width with elevating the aggregation level in the present study is supported by previous *in vivo* and *in vitro* studies [2, 83]. An earlier *in vivo* study [83] has shown that the prominent CFL width can be formed in arterioles under pathological aggregating conditions (M = 21.6 ± 4.8). A similar effect was found in the present study in hyper-aggregating conditions (M = 24.6 ± 4.6) (Fig. III-2A). The mean CFL width results obtained in this study confirmed that pathological elevation of the aggregation level could lead to a prominent enhancement in the mean CFL width. However, the CFL width measured here was significantly thinner than that measured in arterioles in all aggregating conditions (See Fig. III-3C). The thicker CFL found in arterioles would allow more room for radial movement of outer most cells in blood flow. Thus, the relatively thin CFL width found in the present study compared to previous *in vivo* results might result in a low standard deviation (SD) [50, 84]. With the small CFL width, the aggregation effect on the SD could be diminished, resulting in no distinct difference in SD among the three aggregating conditions as shown in Fig. III-2B.

5.2 Persistency of CFL variation

The correlation length of the CFL width formed in arterioles (ID = 10 – 50 μm) of the rat cremaster muscle has been reported to be 32 ± 5.6 μm in non-aggregating conditions and 30 ± 4.0 μm in normal aggregating conditions at ~42% hematocrit [50], with no significant difference. Thus, the correlation length appeared to be independent of

aggregating condition. In another study by Silva and Intaglietta [111], the correlation length of ~16 µm was reported in a 25 µm ID arteriole at a pseudoshear rate of 124 s^{-1}. In the present study, the correlation length appeared to be also independent of aggregating condition. However, relatively greater correlation lengths (49 ± 5.1 µm) were obtained in this study as compared with those reported in the previous studies [50, 111]. This greater correlation length might be due to the different flow environment between the earlier *in vivo* and present *in vitro* studies. In the arteriolar flow, variations in flow velocity due to the arterial pulse would exist during the CFL width measurement. A previous study [43] reported that during the cardiac cycle, centerline velocity varied by a maximum of ± 6% – 7% from the mean value in arterioles of the cat omentum. Thus, the arteriolar pulsatile flow would shorten the correlation length. In addition, in the rat cremaster muscles, the interbifurcation distance has been reported to vary between 172 and 663 µm for arterioles of 12.5 – 104 µm [82], whereas the distance (80 mm) from the baseline (0.0*D*) of the CFL measurement to the inlet of the microtube in the present study was more than 120 times longer than the interbifurcation distance. The short interbifurcation distance would also contribute to shortening the arteriolar correlation length. Non-uniformity of luminal surface of arterioles leading to frequent changes of vessel diameter would also enhance this effect. All these *in vivo* factors may significantly cause the discrepancy in the persistency of CFL width between the current *in vitro* and previous *in vivo* studies. Therefore, direct comparison between *in vitro* and *in vivo* results would be limited.

5.3 RBC-wall contact frequency

For the *in vitro* case, the distinct attenuation of the contact frequency in the presence of RBC aggregates was expected since we found a significant increase ($P < 0.05$ in normal-aggregating conditions, $P < 0.001$ in hyper-aggregating conditions) in the CFL width due to aggregation compared to non-aggregating conditions (Fig. III-2A). The thicker CFL width formation that increases the distance between outer edge of cells and inner tube wall would reduce the chance for RBCs to make contact with the wall. Interestingly, despite the higher hematocrit (~47%) for the *in vivo* condition [83], the contact frequency in arterioles was significantly lower than that in microtubes (~40%) for all aggregating conditions. In particular, most of *in vivo* results with RBC aggregation showed that the RBC-wall contact was seldom observed during the measurement (1 s).

The compared *in vivo* data were selectively taken from our previous results [83] that have the V_{edge} similar to the *in vitro* V_{edge}. No significant difference was found in V_{edge} between *in vitro* (2.7 ± 0.6 mm/s) and *in vivo* (2.7 ± 1.3 mm/s) data. We also confirmed that aggregating conditions (M = 0.0, 12.9 ± 3.4, and 20.8 ± 5.8 for the three aggregating conditions) used in the *in vivo* study were not significantly different from the aggregating conditions used in this study. Therefore, the discrepancy in the contact frequency between *in vitro* and *in vivo* would be due mainly to the difference in the CFL mean width (see Fig. III-3C). It should be noted that the CFL width measured by the current method would include the glycocalyx layer thickness, in particular in arterioles if present [49]. The glycocalyx thickness has been reported to be ~0.38 μm in arterioles with diameter of ~20-70 μm [105]. Therefore, with existence of the glycocalyx layer in arterioles, the contact frequency between RBC and the endothelium should be zero. However, since the spatial resolution (~0.42 μm) of the CFL measurement in our

previous *in vivo* study [83] was greater than the arteriolar glycocalyx thickness (~0.38 μm), the low contact frequency data (Fig. III-3B) obtained from the previous study could be due to the limitation of the measurement system.

Figure III-3C compares normalized mean CFL width data obtained in the present *in vitro* study and our previous *in vivo* study [83]. In the current *in vitro* condition, the normalized mean width of CFL (0.10, 0.14 and 0.17 for the three aggregating conditions) was significantly smaller than that in arterioles (0.17, 0.22 and 0.26 for the three aggregating conditions). Even when we subtracted the glycocalyx thickness (~0.03 in the normalized width in a 25-μm vessel) from the *in vivo* data, the *in vivo* CFL width was still thicker than the *in vitro* CFL width. Another possible reason for the discrepancy in the mean CFL width might be the elasticity difference between the tube and vessel walls. As reported in an earlier study by Maeda et al. [66], the CFL width (~3.5 μm) in an elastic microvessel with diameter of 25 μm was ~20% greater than that (~2.8 μm) in a hardened microvessel. The microtube wall in the present study would be much more rigid than the arteriolar wall. Therefore, this difference in wall elasticity might also contribute to the greater mean CFL width in arterioles compared to that in microtubes.

5.4 Effect of aggregation on CFA

To quantify the spatio-temporal changes of CFL width, we provided the time-dependent CFA as new information. The CFA represents instantaneous morphological changes of CFL in spatial domain. The Figure 4 showed asymmetric CFL formed on the two sides of the tube wall. Such an asymmetry of CFL was also observed in a previous

in vivo study [50], which reported that the CFL width was substantially different on the two sides of vessel without RBC aggregation but the symmetry of CFL widths appeared to be recovered after inducing the aggregation. The same trend was found for the CFA in the present study (Fig. III-4B). This would be due to non-uniform distribution of RBCs in the core [32], and the non-uniformity would be attenuated by the aggregation due to compact formation of RBCs in the core.

The larger NCFA value (Fig. III-5A) indicates that more space can be occupied by CFL with elevating the RBC aggregation level. Not only the increase of the CFL width (one-dimensional parameter) at particular site (Fig. III-2A) but also the CFA (two-dimensional parameter) can be increased by aggregation. Those increases would be due to enhancement of capability of forming compact aggregates in the blood core. The time integrated NCFA results (Fig. III-5B) provides the accumulated information on the CFL variations both in space and time domains. The increase in tail width (Fig. III-6C) indicates that the NCFA can vary widely, which implies that temporal changes of the CFA can be promoted with elevating the aggregation level. In addition, the significant ($P < 0.05$) increase in the right tail width from non-aggregating to hyper-aggregating conditions suggests that the tendency of the CFL to extend into the RBC core away from its mean can be significantly enhanced by aggregation. This phenomenon would be important in hemodynamics since thicker CFL width due to the presence of RBC aggregates may result in a greater inward radial deviation of the CFL width into the RBC core, potentially leading to separation of the RBC core.

Under *in vivo* conditions, in particular in arteriolar flows, such a promoted CFA variation may result in an increase of wall shear stress and consequently an enhancement

of nitric oxide production rate in the endothelium as similarly found in our previous simulation studies [80, 81]. Moreover, the CFA of ~15% occupational fraction of blood flow particularly under pathological aggregating conditions would have a significant effect on the nitric oxide and/or oxygen diffusion in the microcirculation [57]. Although, in this study, it was feasible to visualize the CFA variations in ROI by using the image analysis technique [76], its *in vivo* application might be limited due to irregularity of the vessel wall and inconsistency of image contrast between RBCs and background along the vessel length [40, 110].

CHAPTER IV: TWO-PHASE MODEL FOR PREDICTION OF CELL-FREE LAYER WIDTH IN BLOOD FLOW

1. Introduction

As highlighted in many previous studies [31, 75, 109], formation of the CFL in the microcirculation is physiologically and pathophysiologically important. Thus, there have been attempts to predict the layer formation by using computational models. Sharan and Popel [109] have predicted the layer width as a function of tube diameter and hematocrit with a simplified two-phase continuum model. Later, Das *et al*. [30] have proposed a two-phase Casson model with consideration of the layer width changes in describing the RBC velocity profiles in venules at low flow rates. More recently, Moyers-Gonzalez and Owens [75] predicted the layer width as a function of pseudoshear rate and tube diameter using the kinetic theory modeling. Although those studies have provided relatively good predictions on the layer width, effects of RBC aggregation on the layer formation in different flow conditions have not been considered in their continuum models, which may be significant in pathological aggregating and flow conditions.

Alternatively, several numerical studies [36, 123] have proposed multi-particle flow models to simulate formation of RBC aggregates. In the model developed by Zhang *et al*. [123], three levels of RBC aggregation were considered by varying the intercellular interaction energy. However, the simulated levels of RBC aggregation in their study seemed rather arbitrary and thus might not be directly relevant to the levels found in physiological and pathological conditions. Fedosov *et al*. [36] have also predicted the

CFL formation in microtubes, but only under physiological aggregating conditions. Thus, their model may not be applicable to the layer width prediction in pathological aggregating conditions. Furthermore, it is of note that one of major drawbacks of the multi-particle simulation is its high computing cost.

2. Motivation and Purpose

Since the potential roles of the CFL in microcirculation have been of interest, many simulation studies have attempted to predict the layer formation by using different computational models.

- Although previous computational models have provided appropriate predictions on the layer formation in different rheological conditions, effects of RBC aggregation on the layer formation has not been considered in the continuum models.
- The empirical equation to describe the relative viscosity relation of blood in previous studies was limited to non-aggregating conditions. Although previous multi-particle flow models can consider the formation of RBC aggregates, the simulated levels of RBC aggregation were artificial and thus may not be relevant to levels found in physiological and pathological conditions.
- Clinical studies [3, 11, 48, 86, 98] have reported that abnormally intensified RBC aggregation is a common response to hemorheological disorders. Despite its significant influence on the CFL formation, information on how the altered aggregation affects the layer formation is limited.

Therefore, the present study aimed to develop a simple continuum model that requires a relatively low computing cost but is capable of predicting the CFL width under aggregating conditions. The initial goal of the model was to predict the change of the CFL width in narrow tubes as a function of flow rate and tube diameter at both physiological pathological levels of RBC aggregation. To achieve this, viscosity functions were empirically obtained from *in vitro* microtube experiments under physiological and pathophysiological flow conditions. These empirical relations were then utilized in our two-phase continuum model to predict the layer width change.

In the following section, materials and method for *in vitro* experiment are described and the mathematical derivation is also presented. The results and discussion section covers the relative apparent viscosity results from *in vitro* experiments and its effect on the simulation results is discussed.

3. Materials and Methods

3.1 Blood samples

Horse blood (Innovative Research, Novi, USA) was centrifuged and washed with Phosphate Buffer Saline (PBS, Hanks). After centrifugation, the buffy coat was gently removed and washed three times to collect packed red blood cells (RBCs) from the whole blood. The RBCs were then resuspended in PBS. The blood sample solutions were prepared at a hematocrit of ~40% which was verified with the Microhematocrit Centrifuge (Sigma 1-14, Goettingen, Germany). An optical aggregometer (Myrenne aggregometer MA1, Roentgen, Germany) was used to quantify the RBC aggregation in terms of the aggregation index (M). The aggregation tendency of the blood samples was adjusted to physiological (M = 12-16) and pathological (M > 20) levels seen in humans by adding Dextran 500 (average molecular mass of 460 kDa, Sigma) at concentration of 5.0 and 7.5 mg/ml, respectively [11, 48, 59].

3.2 Perfusion system and experimental procedure

Figure IV-1 shows the schematic diagram of our perfusion system used for the experiments. A pressure transducer (Biopac TSD 104A, Goleta, USA) was connected to a 1-ml syringe and an Inner-Lok connector (Polymicro Technologies, Phoenix, USA) via a three-way valve. The inner diameters of microtubes used in this study were 30, 50, and 100 μm with length of 50 ± 0.50 mm. The flow rate of blood sample was controlled with a syringe pump (KDS 210, Holliston, USA) while the pressure drop through the tube was monitored and recorded using the pressure transducer. The perfusion system was flushed

with plasma to reduce cell adhesion of RBCs to the internal surface of the tube, and then it was pre-filled with the blood sample to eliminate air bubbles trapped inside the system. Magnetic stirrers were inserted into the syringe and three-way valve to prevent sedimentation of RBCs during the experiment. The apparent viscosity of blood samples under non-aggregating conditions was determined over a range of pseudoshear rates approximately from 1 to 300 s^{-1} at room temperature (21℃). The viscosity determination was repeated at physiological and pathological levels of aggregation.

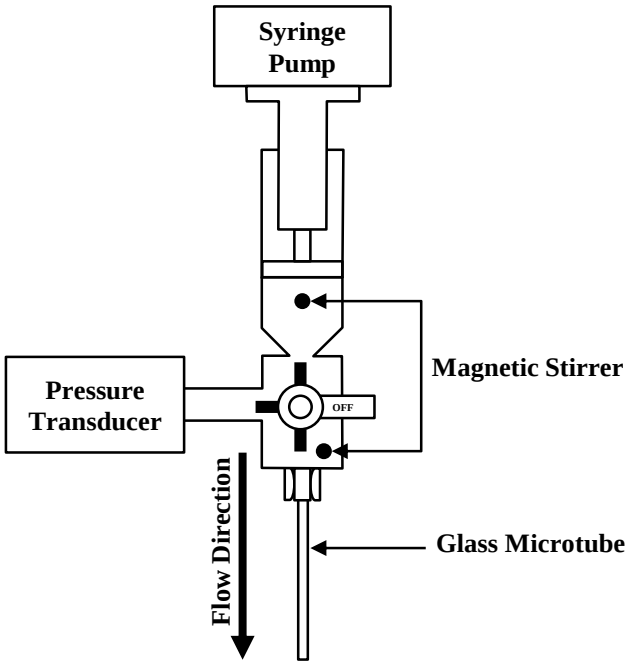

Figure IV-1: Schematic diagram of the perfusion system for the apparent viscosity measurement.

3.3 Numerical model

In the present study, we assumed that the CFL width would be constant at a given flow rate and under the same RBC aggregating condition. The relation between the aggregating tendency and CFL width was derived from experimental data of the apparent viscosity of blood in a microtube over a wide range of shear rates under different aggregating conditions.

Pseudoshear rate ($\bar{\gamma}$) was defined as the ratio of the mean velocity of flow ($\overline{V}$) to the inner diameter of tube (*D*):

$$\bar{\gamma} = \frac{\overline{V}}{D} \tag{1}$$

Apparent viscosity of blood samples (μ_{app}) was determined by using the Hagen Poiseuille's equation:

$$\mu_{app} = \frac{\Delta P \pi R^4}{8QL} \tag{2}$$

where ΔP = pressure drop across the tube, R and L = radius and length of the tube respectively, and Q = volumetric flow rate.

In the present study, the blood flow was assumed to be represented by a two-phase continuum model. The equations of motion for steady, laminar, incompressible, and fully-developed flow through a tube in cylindrical coordinates can be expressed as:

$$-\frac{\partial p}{\partial z} + \frac{\mu_c}{r}\frac{\partial}{\partial r}\left(r\frac{\partial u_c}{\partial r}\right) = 0, \quad (0 \le r < r_c\,; \text{RBC core region}) \tag{3a}$$

$$-\frac{\partial p}{\partial z}+\frac{\mu_o}{r}\frac{\partial}{\partial r}\left(r\frac{\partial u_o}{\partial r}\right)=0, \quad (r_c < r < R; \text{cell - free layer region}) \tag{3b}$$

where p = hydraulic pressure, u_c and u_o = velocity in RBC core and CFL regions respectively, μ_c and μ_o = viscosity of the core and CFL respectively, and r_c = distance from the tube centerline to the outmost edge of the RBC core. The blood flow is subjected to the following boundary conditions:

$$\frac{\partial u_c}{\partial r}=0 \quad at\ r=0 \tag{4a}$$

$$u_o=0 \quad at\ r=R \tag{4b}$$

$$u_c=u_o \quad at\ r=r_c \tag{4c}$$

$$\mu_c\frac{\partial u_c}{\partial r}=\mu_o\frac{\partial u_o}{\partial r} \quad at\ r=r_c \tag{4d}$$

Thus, the velocity profile of the blood flow can be derived as follows:

$$u_c(\xi)=\frac{PR^2}{4\mu_o}\left[1-\lambda^2+\frac{\mu_o}{\mu_c}\left(\lambda^2-\xi^2\right)\right], \quad (0\le\xi\le\lambda) \tag{5a}$$

$$u_o(\xi)=\frac{PR^2}{4\mu_o}\left[1-\xi^2\right], \quad (\lambda\le\xi\le 1) \tag{5b}$$

where $\xi=\frac{r}{R}, \lambda=\frac{r_c}{R}$, and $P=\frac{|\Delta p|}{L}$.

Then, the volumetric flow rate (Q) can be calculated from the velocity profile shown in Eqs. (5a, b) as follows:

$$Q = 2\pi R^2 \int_0^{\lambda} u_c(\xi)\xi d\xi + 2\pi R^2 \int_{\lambda}^{1} u_o(\xi)\xi d\xi$$
$$= \frac{\pi P R^4}{8\mu_o}\left[\frac{\mu_o}{\mu_c}\lambda^4 + 1 - \lambda^4\right] \quad (6)$$

The overall mass balance of RBCs in the tube can then be defined as:

$$QH_d = 2\pi R^2 \int_0^{\lambda} \xi u_c(\xi)h(\xi)d\xi + 2\pi R^2 \int_{\lambda}^{1} \xi u_o(\xi)h(\xi)d\xi$$
$$= \frac{\pi P R^4 H_c}{8\mu_o}\left[\frac{\mu_o}{\mu_c}\lambda^4 + 2\lambda^2(1-\lambda^2)\right] \quad (7)$$

where $h(\xi) = \begin{cases} H_c, & 0 \le \xi \le \lambda \\ 0, & \lambda < \xi \le 1 \end{cases}$, H_d and H_c = discharge and core hematocrit, respectively.

Using Eqs. (2) and (6), the apparent viscosity (μ_{app}) and relative viscosity (μ_{rel}) can be obtained as follows:

$$\mu_{app} = \mu_o\left[\frac{\mu_o}{\mu_c}\lambda^4 + 1 - \lambda^4\right]^{-1} \quad (8a)$$

$$\mu_{rel} = \frac{\mu_{app}}{\mu_m} = \frac{\mu_o}{\mu_m}\left[\frac{\mu_o}{\mu_c}\lambda^4 + 1 - \lambda^4\right]^{-1} \quad (8b)$$

where μ_m is suspending medium viscosity.

The tube hematocrit (H_t) is defined by:

$$H_t = 2\int_0^1 h(\xi)\xi d\xi = \lambda^2 H_c \quad (9)$$

where $h(\xi) = \begin{cases} H_c, & 0 \le \xi \le \lambda \\ 0, & \lambda < \xi \le 1 \end{cases}$. By eliminating Q from Eqs. (6) and (7), the hematocrit ratio (H_c/H_d) can be expressed as:

$$\frac{H_c}{H_d} = \frac{\frac{\mu_o}{\mu_c}\lambda^4 + 1 - \lambda^4}{\frac{\mu_o}{\mu_c}\lambda^4 + 2\lambda^2(1-\lambda^2)} \tag{10}$$

The detailed derivation steps for the above equations are available in Appendix D.

3.4 Viscosity analysis of experimental data

Relative viscosity

The μ_{rel} functions in terms of pseudoshear rate ($\bar{\gamma}$) and tube diameter (D) at the three different levels of aggregation were obtained by fitting the *in vitro* experimental data. We used the following functions (Eqs. (11a, b, c)) for the curve-fitting. Under aggregating conditions, reduction of μ_{app} in narrow tubes (D < 300 μm) in low shear conditions has been known and it is due mainly to the RBC aggregation leading to an enhanced formation of the CFL [2, 28]. In this study, since the μ_{rel} data under aggregating conditions appeared to have a distinct transition point at a particular pseudoshear rate, we divided the data into two groups (before and after the transition pseudoshear rate ($\bar{\gamma}_{transition}$) for the curve-fitting.

$$\mu_{rel} = P_1 \bar{\gamma}^{P_2}, \quad 1 \le \bar{\gamma} \le \bar{\gamma}_{transition} \tag{11a}$$

$$\mu_{rel} = P_3 e^{P_4 \bar{\gamma}}, \quad \bar{\gamma}_{transition} \le \bar{\gamma} \le 300 \tag{11b}$$

$$\mu_{rel} = min(P_1 \bar{\gamma}^{P_2}, P_3 e^{P_4 \bar{\gamma}}), \quad 1 \le \bar{\gamma} \le 300 \tag{11c}$$

where $P_i = a_i D^2 + b_i D + c_i \ (i = 1,2,3,4); a,b,c = \text{constant}$. All the coefficients were determined through the curve-fitting process.

Core viscosity

The core viscosity (μ_c) of blood in the microtube was estimated by measuring the blood viscosity with a cone-and-plate viscometer (DV-II+, Brookfield Engineering Laboratories, Inc., Middleboro, MA, USA). To obtain information on the core hematocrit (H_c) dependence of μ_c, blood samples were prepared at different hematocrits (~30% to ~60%) under the three different aggregating conditions and their viscosities were measured over a wide range of shear rates ($\dot{\gamma}_c$) (11.25 - 300 s^{-1}). The viscosity results were then fitted to the two-variable power-law model proposed by Walburn and Schneck [120].

$$\mu_c = K \cdot \dot{\gamma}_c^{\,n-1} \quad \begin{cases} K = C_1 e^{C_2 H_c} \\ n = C_4 + C_3 H_c \end{cases} \tag{12}$$

It is of note that the shear rate ($\dot{\gamma}_c$) in Eq. (12) needs to be converted into the pseudoshear rate ($\bar{\gamma}$) since all the equations used in the present study are described in terms of $\bar{\gamma}$.

In the RBC core region, velocity profile can be divided into two components; velocity at the edge of RBC core ($\xi = \lambda$) and velocity profile described by the power law model.

$$u_c(\xi) = u_o(\lambda) + u_c'(\xi) \quad (0 \le \xi \le \lambda) \tag{13}$$

Volumetric flow rate in the core region (Q_c) becomes

$$Q_c = \pi\lambda^2 R^2 u_o(\lambda) + Q_c' \tag{14}$$

where Q_c' = volumetric flow rate described by the power law model and it is

$$Q_c' = \frac{\pi r_c^3}{3 + 1/n}\left(\frac{Pr_c}{2K}\right)^{1/n} \tag{15}$$

where $r_c = \lambda R$ (radius of the core region).

To define the relationship between $\bar{\gamma}_c$ and $\dot{\gamma}_c$, $\bar{\gamma}_c$ can be expressed as follows:

$$\bar{\gamma}_c = \frac{\bar{u}_c}{2r_c} = \frac{Q_c'}{\pi r_c^2}\frac{1}{2r_c} = \frac{1}{2}\frac{1}{3 + 1/n}\left(\frac{Pr_c}{2K}\right)^{1/n} \tag{16}$$

where $\bar{u}_c$ = mean velocity of core region.

The power law model of μ_c is:

$$\mu_c = K \cdot \dot{\gamma}_c^{\,n-1}$$
$$\dot{\gamma}_c = \left(\frac{\mu_c}{K}\right)^{1/n-1} \tag{17}$$

Since μ_c can be expressed as $\mu_c = \frac{P\pi r_c^4}{8Q_c'}$, we can obtain the following relation.

$$\mu_c = \frac{Pr_c}{\frac{8}{3+1/n}\left(\frac{Pr_c}{2K}\right)^{1/n}} = \frac{Pr_c}{16\bar{\gamma}_c} \tag{18}$$

Eq. (17) can then be rewritten by substituting μ_c with Eq. (18) as follows:

$$\dot{\gamma}_c = \left(\frac{1}{K}\frac{Pr_c}{16\bar{\gamma}_c}\right)^{1/n-1} = \left(\frac{1}{8}\frac{1}{\bar{\gamma}_c}\frac{Pr_c}{2K}\right)^{1/n-1} = \left(\frac{1}{8}\frac{1}{\bar{\gamma}_c}(6+2/n)^n \bar{\gamma}_c^n\right)^{1/n-1} \tag{19}$$

Finally, we can obtained the following relation between $\bar{\gamma}_c$ and $\dot{\gamma}_c$.

$$\dot{\gamma}_c = \bar{\gamma}_c\left(\frac{1}{8}(6+2/n)^n\right)^{1/n-1} = \bar{\gamma}_c \cdot f(n) \tag{20}$$

The coefficient *n* determined from results obtained with the cone-and-plate viscometer was ranged from 0.64 to 0.84 under all aggregating conditions at ~30% - ~60% of core hematocrit. Although the *n* varied, its corresponding change of $f(n)$ was less than 0.05%. Thus, the averaged value of $f(n)$ in the range of *n* was used to simplify the relation between $\bar{\gamma}_c$ and $\dot{\gamma}_c$ as follows:

$$\dot{\gamma}_c \approx 6.31 \cdot \bar{\gamma}_c \tag{21}$$

In Eq. (21), $\bar{\gamma}_c$ can be determined by using the volumetric flow rate relationship as follows:

$$Q = Q_c + Q_o = \pi\lambda^2 R^2 u_o(\lambda) + Q_c' + Q_o \tag{22}$$

where Q_o = flow rate of CFL region. Each term of Eq. (22) can be represented as follows:

$$\pi\lambda^2 R^2 u_o(\lambda) = \pi\lambda^2 R^2 \frac{PR^2}{4\mu_o}[1-\lambda^2] = \frac{\pi PR^4}{4\mu_o}\left[\lambda^2 - \lambda^4\right] \tag{23a}$$

$$Q_c' = \pi r_c^2 \bar{u}_c = \pi(\lambda R)^2 \bar{\gamma}_c \lambda D = \pi\lambda^3 R^2 \bar{\gamma}_c D \tag{23b}$$

$$Q_o = 2\pi R^2 \int_\lambda^1 u_o(\xi)\xi d\xi = 2\pi R^2 \frac{PR^2}{\mu_o}\int_\lambda^1 \xi - \xi^3 d\xi = \frac{\pi PR^4}{8\mu_o}\left[1-2\lambda^2+\lambda^4\right] \tag{23c}$$

In Eq. (22), Q can be also represented as a function of $\bar{\gamma}$.

$$Q = \frac{\pi PR^4}{8\mu_{app}} = \pi R^2 \bar{u} = \pi R^2 \bar{\gamma} D \tag{24}$$

where $\bar{u}$ is mean velocity of overall flow. Thus, by using Eqs. (23a, b, c) and (24), we can express Q as a function of $\bar{\gamma}$ as follows:

$$Q = 2\pi R^2 \frac{\mu_{app}}{\mu_o}\bar{\gamma} D\left[\lambda^2 - \lambda^4\right] + \pi R^2 \frac{\mu_{app}}{\mu_o}\bar{\gamma} D\left[1-2\lambda^2+\lambda^4\right] + \pi\lambda^3 R^2 \bar{\gamma}_c D \tag{25}$$

By rearranging the above equation, the relationship between $\bar{\gamma}$ and $\bar{\gamma}_c$ can then be obtained as:

$$\bar{\gamma}_c = \frac{\bar{\gamma}}{\lambda^3}\left[1 - \frac{\mu_{app}}{\mu_o}\left[1-\lambda^4\right]\right] \tag{26}$$

Hematocrit function

H_t as a function of H_d and D was taken from a previous study by Sharan and Popel [109]. (Eq. (27)) In the present study, the H_d was fixed at 40% for all cases.

$$\frac{H_t}{H_d} = H_d + (1 - H_d)(1 + 0.3871e^{-0.1779D} - 0.603e^{-0.0111D} - 0.0187e^{-9.0610e^{-11D}}) \qquad (27)$$

3.5 Numerical solution

Based on the numerical model proposed by Sharan and Popel [109], μ_o was assumed to be higher than μ_m. Thus, by introducing a dimensionless parameter ($\beta = \mu_o/\mu_m$), the term of μ_o/μ_c in all equations was expressed by $\beta \cdot (\mu_m / \mu_c)$. Figure IV-2 briefly describes the analysis process for prediction of the cell-free layer width in a tube under different flow and aggregating conditions. The solution was obtained through the iteration process of evaluating our guess ($\hat{H}_c$) of the core hematocrit.

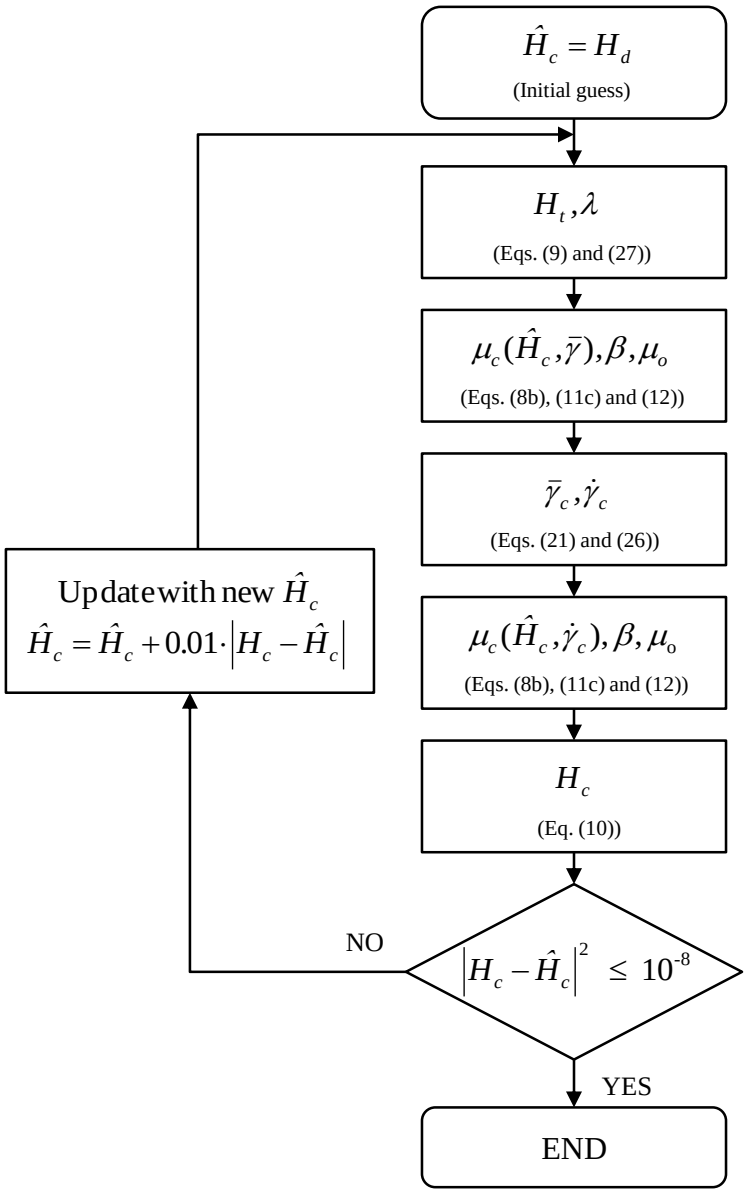

Figure IV-2: Flow chart of numerical analysis process.

4. Results and Discussion

4.1 Systemic parameters

The RBC aggregation index (M) and systemic hematocrit are listed in Table IV-1. There were no significant differences among the three groups for the parameters shown in the table. The M value was 0.0 in non-aggregating blood samples. For aggregating conditions, M values for blood samples only at 40% hematocrit are shown here. Although M values varied as changing hematocrit, we did not find any significant difference in the values at a particular hematocrit.

4.2 Relative viscosity (μ_{rel})

The primary goal of this study was to develop a new numerical method of predicting the CFL width as a function of tube diameter (D) and pseudoshear rate ($\bar{\gamma}$) under aggregating conditions. To achieve this, the relation between μ_{rel} and $\bar{\gamma}$ was needed first. Eqs. (11a, b, c) were used for the curve-fitting process to obtain μ_{rel} as a function of D and $\bar{\gamma}$, and the determined coefficients for the equation are listed in Table IV-2.

Figure IV-3 shows experimental data of μ_{rel} with the curve-fitting results. As expected, under the non-aggregating condition, the relation between μ_{rel} and $\bar{\gamma}$ showed a typical shear-thinning behavior for all tube diameters. R^2 of the fitted model for this condition was 0.93. Shown in Figure IV-3A indicates that the CFL effect on the viscosity becomes more pronounced with decreasing D, which has also been reported in previous studies [92, 99].

The experimental results in presence (normal- and hyper-aggregation) of aggregates (Figure IV-3B and 3C) showed that μ_{rel} exponentially increased with $\bar{\gamma}$ until approaching the transition point ($\bar{\gamma}_{transition}$). Reversely, it gradually decreased with increasing $\bar{\gamma}$ beyond the point. This trend was consistent for all tube diameters. The viscosity appeared to be elevated with increasing *D* and this effect became more prominent in low shear conditions (~10 s^{-1}) than in high shear conditions (~300 s^{-1}). This result was in accordance with the finding reported in a previous study [99] that suspended human blood in native plasma and Dextran 250 in a vertical glass tube with tube diameter of 30.2-132.3 μm. The curve-fitted results for μ_{rel} in aggregating conditions were in good agreement with experimental data. R^2 was 0.96 and 0.95 for normal- and hyper-aggregating conditions, respectively.

Table IV-1: Systemic parameters (mean ± SD)

Aggregating Condition	M value	Hematocrit (%)
Non	0.0	39.8 ± 0.8
Normal	13.3 ± 4.0	40.1 ± 0.6
Hyper	25.0 ± 4.1	40.4 ± 1.1

Table IV-2: Coefficients determined for Eq. (11c)

Aggregating Condition		P_1	P_2	P_3	P_4	R^2
Non	*a*	$5.42e^{-5}$	$-1.47e^{-5}$	-	-	0.93
	b	$1.28e^{-2}$	$2.43e^{-3}$	-	-	
	c	3.676	-0.224	100	100	
Normal	*a*	$7.27e^{-4}$	$-2.01e^{-5}$	$1.17e^{-3}$	$-1.07e^{-4}$	0.96
	b	$-3.92e^{-2}$	$1.96e^{-3}$	$-8.65e^{-2}$	$1.41e^{-2}$	
	c	4.145	-0.198	2.744	-0.294	
Hyper	*a*	$4.97e^{-4}$	$-2.61e^{-5}$	$4.95e^{-4}$	$-8.44e^{-6}$	0.95
	b	$-3.11e^{-2}$	$3.64e^{-3}$	$-2.47e^{-2}$	$1.42e^{-3}$	
	c	5.251	-0.291	1.490	$-8.71e^{-3}$	

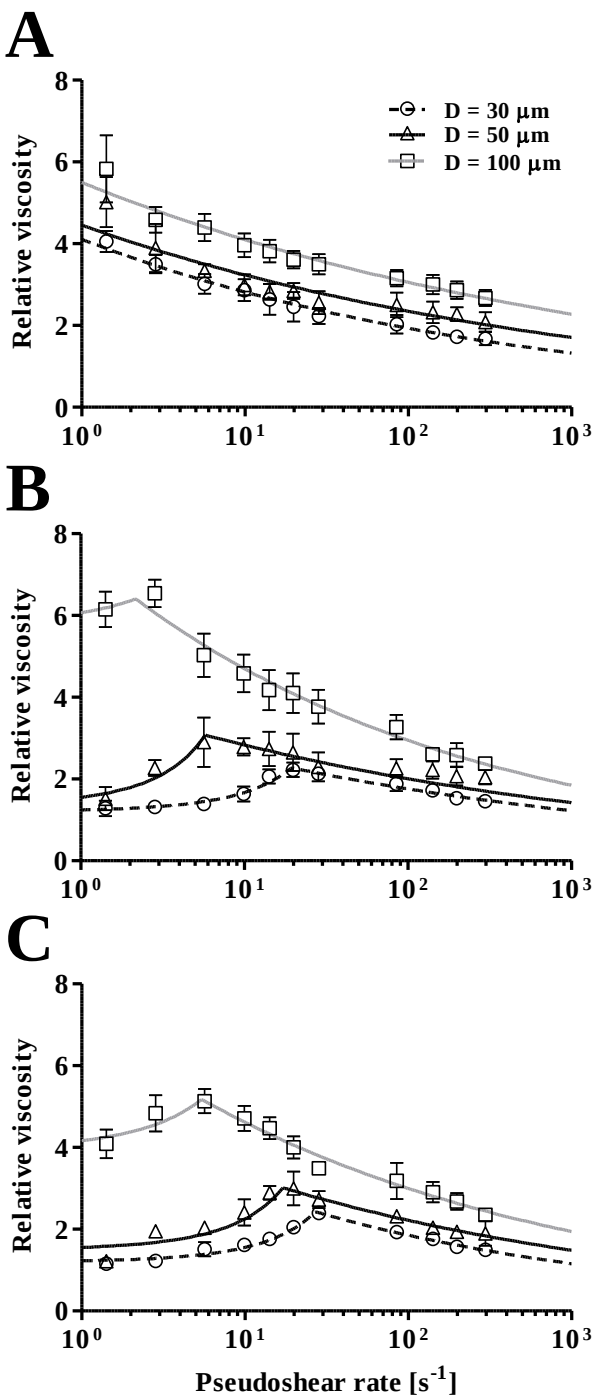

Figure IV-3: Experimental and curve-fitting results of the relative viscosity in three different aggregating conditions (Non-aggregation (A), Normal-aggregation (B) and Hyper-aggregation (C)).
Error bars of symbols represent SD of experimental data.

4.3 Core viscosity (μ_c)

The determined coefficients for μ_c model (Eq. (12)) are listed in Table IV-3, and its experimental data with the curve-fitting results are shown in Figure IV-4. The curve-fitting results for all aggregating conditions were in good agreement with experimental data (R^2 = 0.98). The relation between μ_c and $\dot{\gamma}_c$ showed a typical shear-thinning behavior for all aggregating conditions. The aggregation effect on μ_c was prominent in low shear conditions. In contrast, the aggregation effect was diminished in high shear conditions, which might be due to dissociation of aggregates under high shear forces [106]. As expected, the μ_c was proportional to the hematocrit.

The μ_c of the present study (Eq. (12)) were compared with those determined by a previously suggested model [33]. The previous model was derived from human blood viscosity measurements with the same cone-and-plate viscometer used in this study. Table IV-4 shows comparison of the μ_c from the two studies. Our non-aggregation and normal-aggregation conditions are comparable with 0.9% NaCl and autologous plasma conditions of the previous study, respectively. The viscosity difference between the two studies was 1.2 ± 0.7 cP in the non-aggregation condition and 0.8 ± 0.5 cP in the normal-aggregation condition over the shear rates. The viscosity in the hyper-aggregation condition was greater than the two conditions (0.9% NaCl and autologous plasma) of the previous study at low shear rates (< 150 s^{-1}), but it was a bit smaller at high shear rates. The higher viscosities in low shear conditions would be due to the enhanced RBC aggregation, whereas the viscosity discrepancy in high shear conditions would be resulting from the difference in suspending media used in the two studies. It should be noted that in this study, PBS was used as a suspending medium.

Table IV-3: Coefficients determined for Eq. (12)

Aggregating Condition	C_1	C_2	C_3	C_4	R^2
Non	1.66	5.50	-0.51	0.97	0.98
Normal	4.22	4.06	-0.26	0.83	0.98
Hyper	5.24	4.16	-0.29	0.81	0.98

Table IV-4: Comparison of the current μ_c [cP] with a previous study at 21℃.

Medium condition	Shear rate [s^{-1}]							Reference
	10	20	50	100	150	200	300	
0.9% NaCl	8.5	6.2	5.3	4.1	3.7	3.5	3.5	[33]
Autologous plasma	12.8	9.6	8.4	6.5	5.9	5.7	5.6	[33]
Non-aggregating	8.7	7.4	6.0	5.1	4.6	4.3	3.9	Present study
Normal-aggregating	11.4	9.4	7.3	6.1	5.4	5.0	4.5	Present study
Hyper-aggregating	13.7	11.1	8.4	6.8	6.0	5.5	4.8	Present study

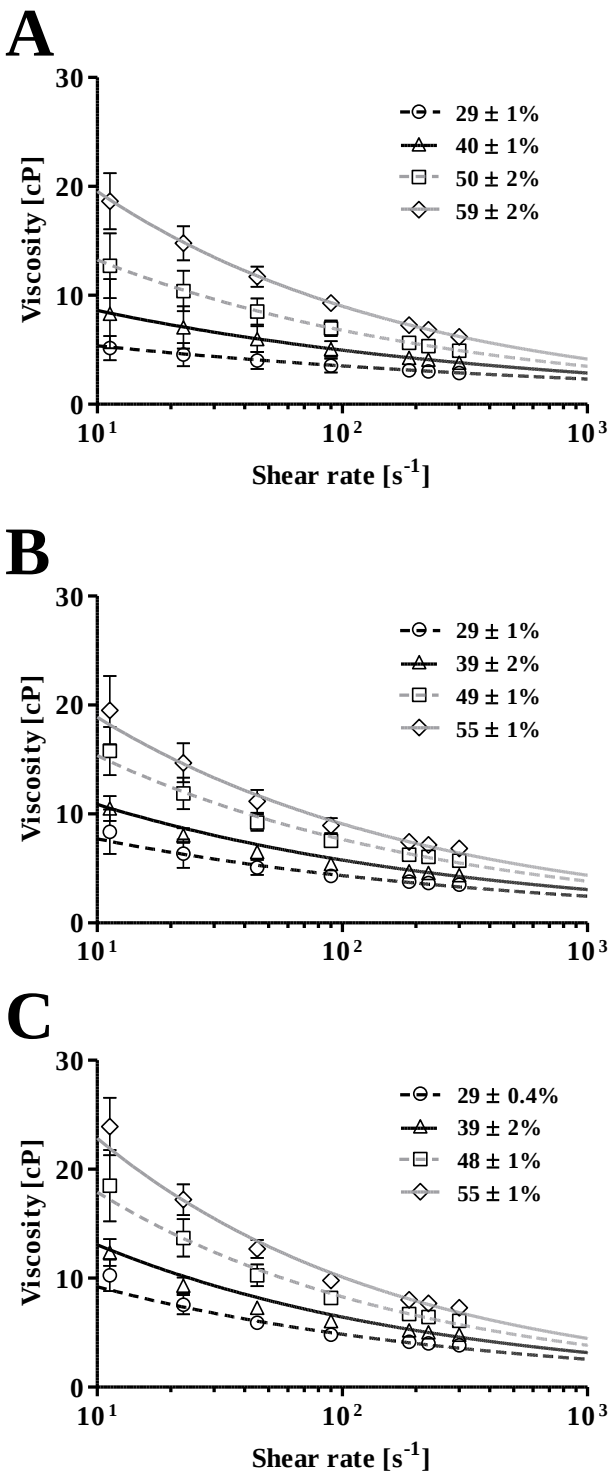

Figure IV-4: Experimental and curve-fitting results for the core viscosity in three different aggregating conditions (Non-aggregation (A), Normal-aggregation (B) and Hyper-aggregation (C)). Error bars of symbols represent SD of experimental data.

4.4 Relation between CFL width and relative viscosity

All numerical analyses were performed over a range of pseudoshear rates from 5 to 300 s^{-1} with tube diameter of 30, 50, and 100 μm at H_d = 40%. The CFL width predicted in this study was normalized by tube radius. Figure IV-5 shows the predicted layer width as a function of $\bar{\gamma}$ in tubes with inner diameter of 30 μm (Figure IV-5A), 50 μm (Figure IV-5B) and 100 μm (Figure IV-5C) for the three aggregating conditions. The layer width under aggregating conditions seemed to be increased below a particular $\bar{\gamma}$ which was identical to the transition point ($\bar{\gamma}_{transition}$) shown in Figures IV-3B and IV-3C, whereas it gradually decreased with increasing $\bar{\gamma}$ above the transition point. Furthermore, this tendency became more pronounced by elevating the degree of RBC aggregation from normal- to hyper-levels. However, in 100-μm tubes, this effect did not seem to be significant (Figure IV-5C). The viscosity has been reported to increase with decreasing the layer width and this relation becomes prominent when the layer width fall below ~10% of tube diameter [2]. Consequently, the attenuation of the viscosity below the $\bar{\gamma}_{transition}$ might result from a thicker layer width in the present study. As also reported in a previous study [123], the relative viscosity generally decreased with enhancing RBC aggregation tendency. In the present study, this effect was reconfirmed and it was prominent particularly below the $\bar{\gamma}_{transition}$ in tubes with diameter of 30 and 50 μm (Figure IV-5A-B).

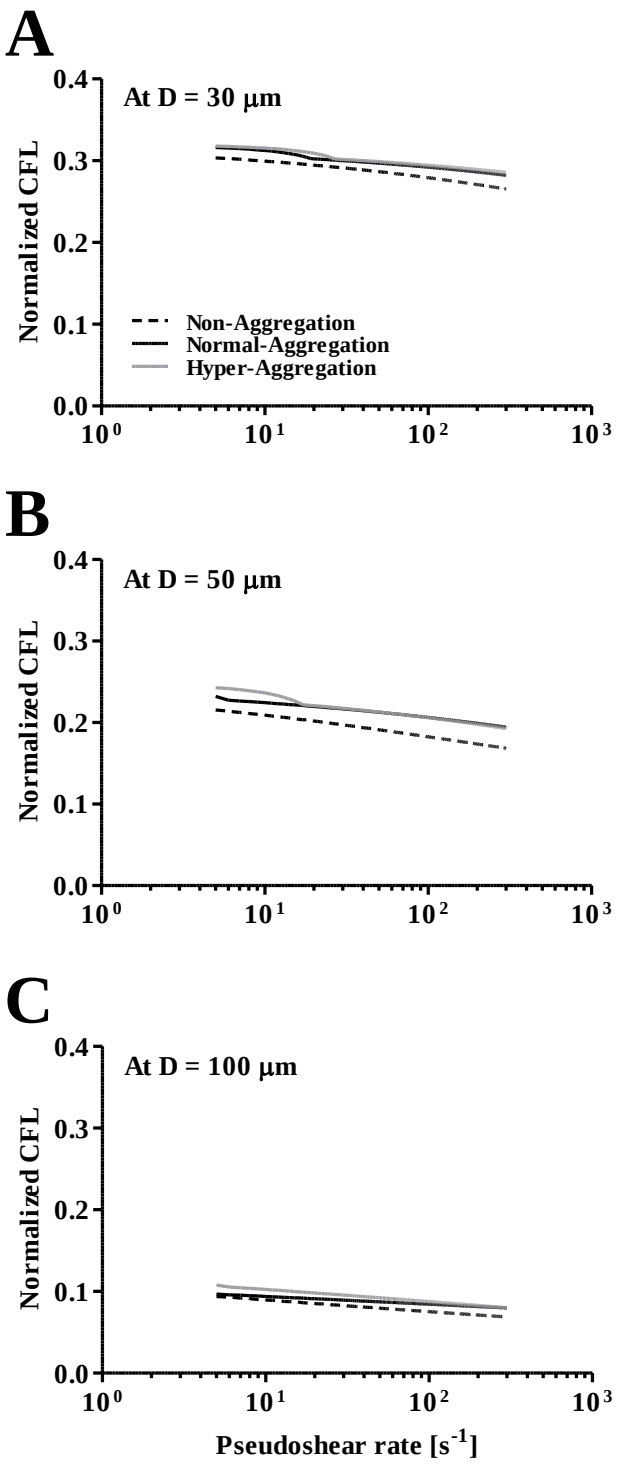

Figure IV-5: Numerical prediction of normalized CFL width as a function of pseudoshear rate in the three different aggregating conditions in tubes with diameter of 30 μm (A), 50 μm (B) and 100 μm (C).

4.5 Comparison with previous studies

Crowl and Fogelson [29] reported the normalized layer thickness (by radius) of 0.08-0.12 at 40% hematocrit in a tube with diameter of 50 μm at 1100 s^{-1}. The normalized layer width of the present study with the same tube diameter was in a range of 0.17-0.24 regardless of $\bar{\gamma}$. This simulated layer width was ~2-fold greater than Crowl and Fogelson's prediction. The discrepancy between the two studies would be due to the fact that they did not consider aggregation effects in their numerical simulation unlike our case. On the other hand, another study by Zhang *et al*. [123] examined the effect of RBC aggregation on formation of the CFL and reported the normalized layer width of 0.25, 0.28 and 0.33 for none, moderate and strong aggregation strengths between RBCs, respectively. This layer width prediction was obtained at ~40% hematocrit in a 19.5-μm tube at ~84 s^{-1} pseudoshear rate. They reported that the normalized layer width was proportional to the aggregation strength. A similar trend was found in the present study. The normalized layer width in presence of RBC aggregates was consistently greater than that without the aggregates (Figure IV-5). However, this effect seemed to be insignificant in comparing normal- and hyper-aggregating cases, in particular at high $\bar{\gamma}$ (> 50 s^{-1}). The normalized layer width with tube diameter of 30 μm in the present study were 0.28, 0.29 and 0.30 for non-, normal- and hyper-aggregating conditions at 84 s^{-1} pseudoshear rate, respectively.

To better illustrate the effects of tube diameter and RBC aggregation on the layer width variation, the predicted layer widths were plotted as a function of tube diameter in the three aggregating conditions at 300 s^{-1} (Figure IV-6A) and 5 s^{-1} (Figure IV-6B). In addition, the present results were compared with those previously reported from *in vitro*

tube experiments [17, 99] and computational simulations [5, 36, 109]. The aggregation effect on the layer formation appeared to be greater at low $\bar{\gamma}$ (5 s^{-1}) than at high $\bar{\gamma}$ (300 s^{-1}). This result was in agreement with previous studies [51, 84] that reported an enhancement of the CFL formation after reduction of flow rate. As expected, our simulated layer widths at 5 s^{-1} for all aggregating conditions were consistently thicker than those reported in the previous studies. This discrepancy would be due to the development of RBC aggregation in low shear conditions as discussed above. It should be noted that the previous studies were performed under normal-aggregating conditions and/or under the situation where the aggregation could be neglected. In addition, the RBC aggregation could make the flow velocity profile more blunted. A previous study [14] reported that the venular velocity profile in the rat spinotrapezius muscle at high $\bar{\gamma}$ became significantly blunted at low $\bar{\gamma}$ (< 40 s^{-1}) under normal aggregating conditions (M = 11.7 ± 5.5).

In a recent study by Sriram and co-workers [113], the regulatory response of arterioles to small changes in hematocrit was predicted by using a two-phase fluid model. The relation between systemic hematocrit and CFL width was utilized for their simulation to predict changes in the NO transport and autoregulatory response. However, unlike the present study, the effects of RBC aggregation were not considered in their study, in particular in determining the CFL width. On the other hand, in our simulation, although such regulatory responses were not considered, we focused more on developing the relation of the CFL width with RBC aggregating tendency based on the empirical relation between the apparent blood viscosity in microtubes and the aggregating tendency.

Moreover, recent computational studies on NO and O_2 transport showed that the CFL has significant impact on the bioavailability of the gases in arterioles by playing a diffusion barrier role [58, 114]. Although the NO/O_2 diffusion was not considered in the present study, our model can also be used for simulation of the gas diffusion with prediction of the CFL width under different aggregating conditions.

4.6 Potential limitations

The CFL width formed by horse blood might differ from that by human blood due to differences in the size of their RBCs. The size of horse cells (mean corpuscular volume ~49 μm^3) is smaller than that of human cells (~89 μm^3) [10]. However, our earlier study [83] reported that the mean magnitudes of the CFL widths obtained from the rats (~55 μm^3) were in good agreement with those found with the perfusion of human RBCs for similar sized microvessels. Thus, the cell size difference does not seem to be a major factor in determining the CFL width.

The RBC aggregation response to high molecular weight dextrans may vary among different species [8, 10]. A comparative study that measured RBC aggregation tendency (M index given by the Myrenne aggregometer) in horses, rats, and humans at 40% hematocrit reported that the horse blood showed ~3-fold higher aggregation tendency than rat blood and ~1.5-fold higher than human blood in the same 0.5% Dextran 500-PBS solution [8]. However, in the present study, the aggregation level of horse blood was adjusted to levels seen in normal and pathological human blood by varying the Dextran 500 concentrations, which was also based on the M index. It is of note that, since the

horse RBC is about 45% smaller in volume than the human RBC as mentioned above, the measured aggregation levels in blood samples from the horse and human may not be directly comparable based on the M indexes. However, this approach, by using the M index to match the aggregation tendency of animal RBCs to the human RBCs, has been well established by many previous studies [15, 53, 84] for investigating the influence of human levels of RBC aggregation in the microcirculation. Furthermore, the new methodology of predicting the CFL width under different aggregating and flow conditions that we propose in this study would be species-independent.

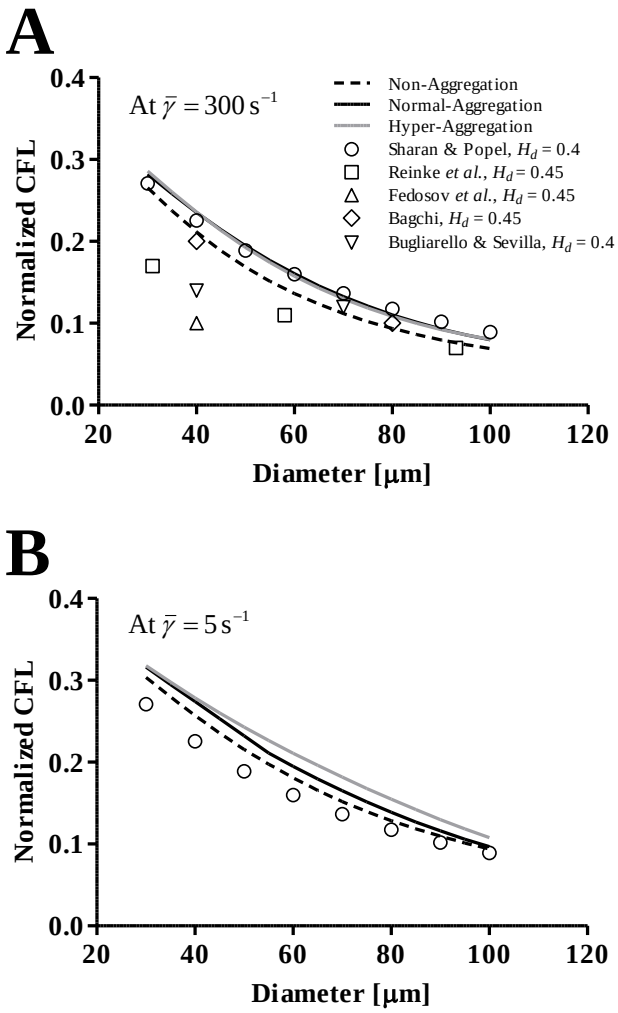

Figure IV-6: Comparison of the current predicted results with previous studies in high and low shear conditions (300 s^{-1} (A) and 5 s^{-1} (B)).
The lines indicate the present simulation results in the three different aggregating conditions. The symbols represent the previous *in vitro* experimental results in tubular flow [17, 99] and the previous computational predictions [5, 36, 109]. H_d represents the discharge hematocrit.

CHAPTER V: EFFECT OF CELL-FREE LAYER VARIATION ON ARTERIOLAR WALL SHEAR STRESS

1. Introduction

Arterioles are the primary regulator of blood flow in microvascular networks [72, 121, 124]. The arterioles play an important role in blood flow distribution to the capillary network to maintain efficient oxygen delivery to surrounding tissues. The arteriolar wall shear stress (WSS) has been of interest as a dominant mechanical force in regulating endothelial cell (EC) functions and vessel homeostasis [24, 102]. A significant role of the WSS is to stimulate release of endothelium-derived nitric oxide (NO) which is a mediator of smooth muscle relaxation [41, 102]. The production rate of NO in general relies on the exposed level of the WSS to ECs, and the relationship between them was reported to be proportional [46, 87]. In addition, the oxygen release from arterioles appears to be related to WSS since the latter was significantly increased by a reduction in oxygen concentration in the vessels [20].

Since the luminal shear stress is a dominant mechanical force on regulating nitric oxide synthase, its modulation by shear stress has been of interest in many studies both in experiments [23, 44, 56, 69] and computational models [46, 114]. A recent review highlighted that CFL width and its variation are important hemodynamic factors in balancing nitric oxide bioavailability in tissue by modulating wall shear stress [67]. In addition, a computational study by Sharan and Popel [109] suggested that roughness of the interface between RBC core and CFL may potentially lead additional energy

dissipation, which in turn causes an increase in the effective plasma viscosity in the CFL. This suggestion implies that elevation in the layer variation may lead augmentation of wall shear stress.

The CFL exhibits dynamic changes in its width. These temporal changes in the CFL width were evident from previous studies that were performed to simulate physiological and pathophysiological states of RBC aggregation [50, 84]. An increase in RBC aggregation coupled with a reduction in flow under pathophysiological conditions was found to result in a more irregular interface between the RBC core and CFL, providing evidence of greater layer variation under rheological abnormalities [84]. While the CFL itself is capable of attenuating WSS by lowering effective blood viscosity, the variation in the layer could potentially offset this effect to some extent through augmenting the WSS and this effect may be more pronounced under pathophysiological conditions [109].

2. Motivation and Purpose

Due to physiological importance of the WSS, there have been a large number of studies to estimate WSS in small vessels both *in vivo* [6, 61, 95] and *in vitro* [45, 100].

- However, *in vivo* information of the WSS under various rheological conditions has been very limited due to the technical difficulties associated with WSS measurement and complexity of the microvascular structure [101].
- Variation of WSS in microvessels could also be a critical determinant of EC response to blood flow since these cells are highly sensitive to microscale subcellular shear stress distribution [7].

- Despite the physiological implications that the CFL can impose through WSS changes in microvascular flow, *in vivo* quantitative information on how the layer variation can affect the WSS has not been available.

Therefore, as the CFL characteristics are dependent on RBC aggregation, we examined how such changes in the layer variation could influence the WSS *in vivo*. We hypothesized that the layer variation would induce an increase in WSS and this effect would be enhanced by RBC aggregation. To examine the hypothesis, a new method of approximating the WSS *in vivo* was proposed and validated by an *in vitro* microtube system. The rat cremaster muscle was exteriorized for visualization of the CFL formation in arteriolar blood flow, and Dextran 500 was used to induce RBC aggregation in the rat.

In the following section, materials and method for the *in vitro* and *in vivo* experiment are described. The results and discussion section covers the validation of and limitations of the WSS estimation. The effect of CFL variation on the WSS and its physiological implications are discussed.

3. Materials and Methods

3.1 Animal preparation

Animal handling procedures were provided according to the Guide for the Care and Use of Laboratory Animals (Institute for Laboratory Animal Research, National Research Council, Washington, DC: National Academy Press, 1996) and approved by the local

Animal Subjects Committee. A total of 12 arterioles in the cremaster muscles from Wistar-Furth rats (202.8 ± 18.5 g) were used in this study. The animal was placed on a heating pad to maintain body temperature at 37 ℃ during surgery, and a tracheal tube was inserted to assist ventilation. The femoral artery was catheterized for blood withdrawals and pressure measurements, whereas the jugular vein was catheterized for administration of anesthetic, Dextran 500 (average molecular mass of 460 kDa; Sigma) dissolved in saline (6%), and other solutions. The rat cremaster muscle was exteriorized and prepared for intravital microscopy. An *in vivo* metrics 1.5 mm ID pneumatic cuff was placed on the abdominal aorta to adjust arterial pressure to the muscle. A heating element maintained the muscle temperature at 35 ℃ during the entire experiment. The detailed information on the animal preparation and measurement procedure is available in Appendix A.

3.2 Hematocrit, Aggregation, and Arterial pressure measurements

The hematocrit was measured with a microhematocrit centrifuge (Readacrit, Clay Adams) and aggregation level of RBC was determined with an aggregometer (Myrenne aggregometer; Myrenne, Roetagen, Germany) periodically during the experiments. A physiological data-acquisition system (MP 100 System; BIOPAC Systems, Goleta, CA) was used to monitor arterial pressure in the femoral artery.

3.3 Experimental protocol

An unbranched region was selected for the study based on stable flow, clear focus, and contrast of the image. An intravital microscope (Ortholux II, Leitz) was used with a water-immersion objective (40X, Olympus) and a long working distance condenser (Instec, Boulder, CO), which has numerical apertures of 0.7 and 0.35, respectively. A blue filter (Spectra Physics, no. 59820) with peak transmission at 400 nm and spectral bandpass of 300-500 nm was used to enhance the contrast between RBCs and the background field. The blood flow was recorded at 1125-4500 frames/s with a high-speed video camera (FASTCOM ultima SE, Photron USA) for 1-4 s, depending on the flow rate in the vessel.

In this study, we obtained data from 4500 frames for all conditions, at normal and reduced arterial pressures before and after dextran infusion. The pneumatic cuff pressure was increased with an air-filled syringe to lower the femoral artery pressure to ~50 mmHg and maintained by manual adjustment. Dextran 500 was used to induce RBC aggregation. A total of 200 mg/kg body weight was infused over the time course of 1-2 min to achieve an estimated plasma dextran concentration of ~0.6%. Our previous studies [50, 52] reported that this concentration of Dextran 500 raised the aggregation level up to those seen in normal human blood. After dextran treatment, an additional blood sample was taken to determine hematocrit and aggregation level.

3.4 Pseudoshear rate determination

The edge velocity of the RBC core was determined by tracking movements of outermost cells manually across 10 digital frames using image analysis software (SigmaScan Pro 5). The pseudoshear rate ($\bar{\gamma}$) used in this study was defined as follows:

$$\bar{\gamma} = \frac{V_{edge}}{D} \tag{1}$$

where V_{edge} is the mean edge velocity of RBC core and *D* is the vessel diameter.

3.5 CFL width and its variability

The CFL width at a specific location was determined from the positions of the inner vessel wall and the outer edge of the RBC core. A typical example of the variation in the layer width is shown in the lower part of Figure V-1. The detailed image analysis method to determine the width of the layer is available in our earlier reports [49, 50]. To quantify the variation in the layer width by the definition of variability, the statistical concept of coefficient of variation was employed, which represents the ratio of the standard deviation of the layer width to its mean.

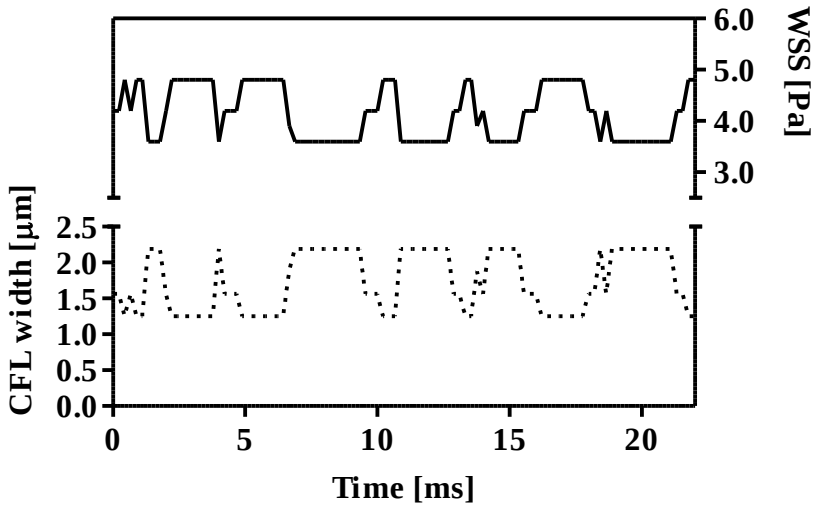

Figure V-1: Relationship between the CFL width and wall shear stress (WSS).
The solid and dotted lines represent the WSS and CFL width obtained in an arteriole (50 µm ID), respectively. Only 100 data selected from 4500 frames are shown here.

3.6 Wall shear stress estimation

In estimation of the WSS, we assumed that the plasma flow in the CFL is steady and the velocity gradient in the layer is linear. Thus, the WSS (τ_w) could be estimated with the plasma viscosity and slope of the linear velocity profile as follows:

$$\tau_w = \mu \frac{V_{edge}}{W} \tag{2}$$

where μ is the plasma viscosity and W is the CFL width. The dextran treatment increases plasma viscosity as well as level of RBC aggregation [54, 91, 95]. However, in our *in vivo* study, the plasma viscosity effect on the WSS was isolated by using the same plasma viscosity value (1.3 cP) [117] in determination of the WSS for all conditions. As shown in the upper part of Figure V-1, using Eq. (2), the WSS is inversely related to the CFL width. The WSS (τ^*) under the influence of the temporal variation in the layer width was obtained by averaging the individual WSS (τ_i) derived from each value of layer width (Eq. (3)) at respective time frames. The result was then compared to that obtained without consideration of the variation in the layer width. For the latter, the CFL widths over 4500 frames were averaged and the resultant mean width was used to estimate the WSS (Eq. (4)). In the Eqs. (3) and (4), *i* denote a frame number.

$$\begin{cases} \tau_i = \mu \dfrac{V_{edge}}{W_i} \\ \tau^* = \dfrac{1}{n}\displaystyle\sum_{i=1}^{n} \tau_i \end{cases} \qquad (i = 1,2,3,\ldots,n = 4500) \tag{3}$$

$$\tau = \mu \frac{V_{edge}}{\dfrac{1}{n}\displaystyle\sum_{i=1}^{n} W_i} \qquad (i = 1,2,3,\ldots,n = 4500) \tag{4}$$

3.7 In vitro setup

We constructed an *in vitro* microtube system to test our hypothesis that WSS may be estimated from the CFL width and plasma viscosity (Eq. (2)). The inner diameter of each glass microtube (Polymicro Technologies, Phoenix, USA) was determined from pressure-flow measurements with distilled water while the length of the tube was measured with the vernier caliper. The inner diameter and length were 50-52 μm and 55-60 mm, respectively. The ratio of length to inner diameter was over 1000:1 so that pressure drops in other parts of the system could be neglected. Reflective index (RI) of the glass tubes (fused silica) was 1.45 for the halogen light spectrum from 650 to 1050 nm and the tubes were immersed in kerosene (RI = 1.45) during blood flow visualization to minimize measurement error for the CFL width, which could be caused by the common RI problem in circular tubes. Heparinized rat blood samples were obtained from donor rats and all the measurements were completed within 1 hour after blood withdrawals. The estimated WSS values using Eq. (2) were compared with those calculated using Eq. (5) shown below with pressure drop information obtained with the differential pressure transducer (MP 100 System, CA, USA) and a syringe pump (Harvard Apparatus, MA, USA). The plasma viscosity was determined with a cone-and-plate viscometer (Brookfield Engineering Laboratories, Inc., MA, USA)

$$\tau_w = \frac{\Delta P \cdot D}{4L} \tag{5}$$

where ΔP is the pressure difference between inlet and outlet of the microtube and L and D are the length and inner diameter of the microtube, respectively.

3.8 Statistical analysis

A statistical software package (Prism 4.0, GraphPad) was used for all statistical analyses. An unpaired t-test was utilized to compare two groups before and after dextran treatment while linear and nonlinear regressions were performed to find a significant relation between the two parameters. All physiological and rheological values are represented as means ± SD. For all tests, $P < 0.05$ was considered to be statistically significant.

4. Results

4.1 In vitro validation

As shown in Figure V-2, the WSS estimated from the CFL width and plasma viscosity agreed within ± 20% with that determined with the pressure drop measurements and R^2 value for the linear regression was 0.76. The error range was similar to that reported with the μ-PIV method by Long *et al*. [63] using fluorescent nano-particles. The pseudoshear rate range used for this comparative study was 130-290 s^{-1}. The good agreement of the WSS estimated from the CFL method with that determined by the conventional pressure drop measurement indicates that the CFL method has promise for *in vivo* use and thus may provide valuable new information where it is currently lacking.

4.2 Systemic values of in vivo experiments

Control arterial pressure was 112 ± 13.7 and 108 ± 4.7 mmHg before and after dextran treatment, respectively. After arterial pressure reduction, the pressure fell to 47 ± 7.9 and 47 ± 5.5 mmHg in normal and dextran-treated rats, respectively. For both control and reduced pressure cases, there was no significant difference between the two pressure values before and after dextran treatment. The index of RBC aggregation (M) determined by the Myrenne aggregometer was 0.0 (no aggregation) before dextran treatment, whereas it increased to 9.9 ± 1.4 after dextran treatment, which is similar to levels found in normal human blood [50, 52]. Systemic hematocrit was 39 ± 1.8% and 38 ± 1.0% before and after dextran treatment respectively, with no significant changes. The diameter range of arterioles used in this study was 29.5-67.1 μm.

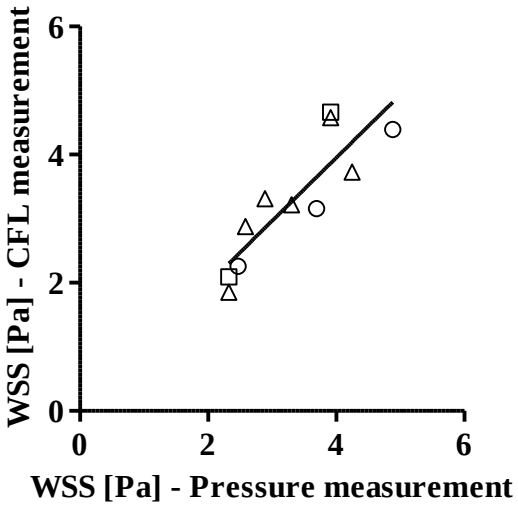

Figure V-2: *In vitro* validation of the WSS estimation with the CFL width and plasma viscosity.
The solid line represents the linear regression fit (y = 0.984x + 0.014; R2 = 0.76) for the combined group of three different conditions (○: without dextran treatment at 30% hematocrit, Δ: with dextran treatment at 30%, and □: without dextran treatment at 35%).

4.3 CFL characteristics

Pseudoshear rate in arterioles at normal arterial pressure was 187.9 ± 52.5 and 177.4 ± 32.8 s^{-1} before and after dextran treatment. After reduction of arterial pressure, the pseudoshear rate dropped to 34.0 ± 19.9 and 31.5 ± 18.4 s^{-1} before and after dextran treatment, respectively. A recent study [84] with similar pressure reduction to that in this study reported that flow velocity in arterioles might be nonuniformly reduced by the arterial pressure drop. Thus, to examine RBC aggregation effect on the CFL variability, we divided all the data into three different pseudoshear rate groups based on their mean values (< 10 s^{-1}, > 40 s^{-1} and < 60 s^{-1}, > 100 s^{-1}). Thus CFL data were grouped into three flow conditions, at 182.8 ± 43.8, 47.9 ± 3.0, and 9.2 ± 0.6 s^{-1}. There was no significant effect of dextran treatment on the CFL variability (Figure V-3) at relatively high pseudoshear rates (182.8 ± 43.8 and 47.9 ± 3.0 s^{-1}), whereas RBC aggregation significantly increased the layer variability ($P < 0.01$) at 9.2 ± 0.6 s^{-1}.

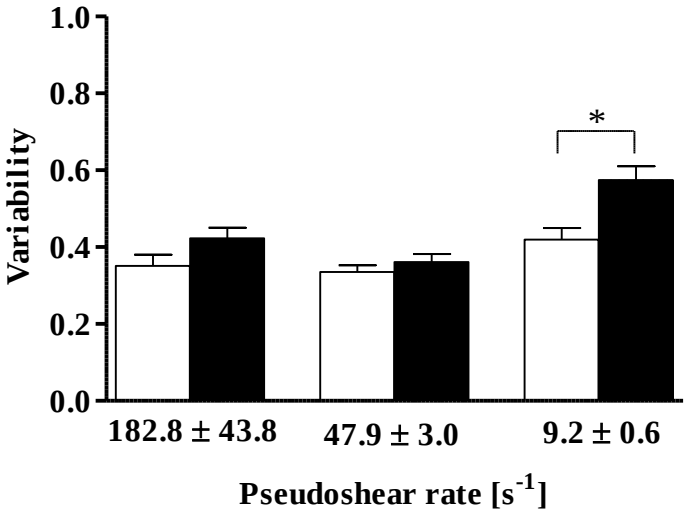

Figure V-3: Effect of RBC aggregation on variability of the CFL.
□: Before dextran infusion. ■: After dextran infusion. *: $P < 0.01$.

4.4 Wall shear stress

Figure V-4 shows the ratio of the WSS with consideration of the variation in the CFL (τ^*) to that when there are no variations in the layer width (τ). The ratio was higher than 1.0 regardless of pseudoshear rates, indicating that the layer variability enhances the WSS. The ratio also increased with an elevation of the variability at all pseudoshear rates and this effect became more pronounced at low shear rates based on the larger coefficient (B_2) that describes the steepness of the fitted curve. There was a slight shift in range of the layer variability from 0.26-0.67 to 0.34-0.81 after dextran treatment, which is not surprising according to the findings shown in Figure V-3.

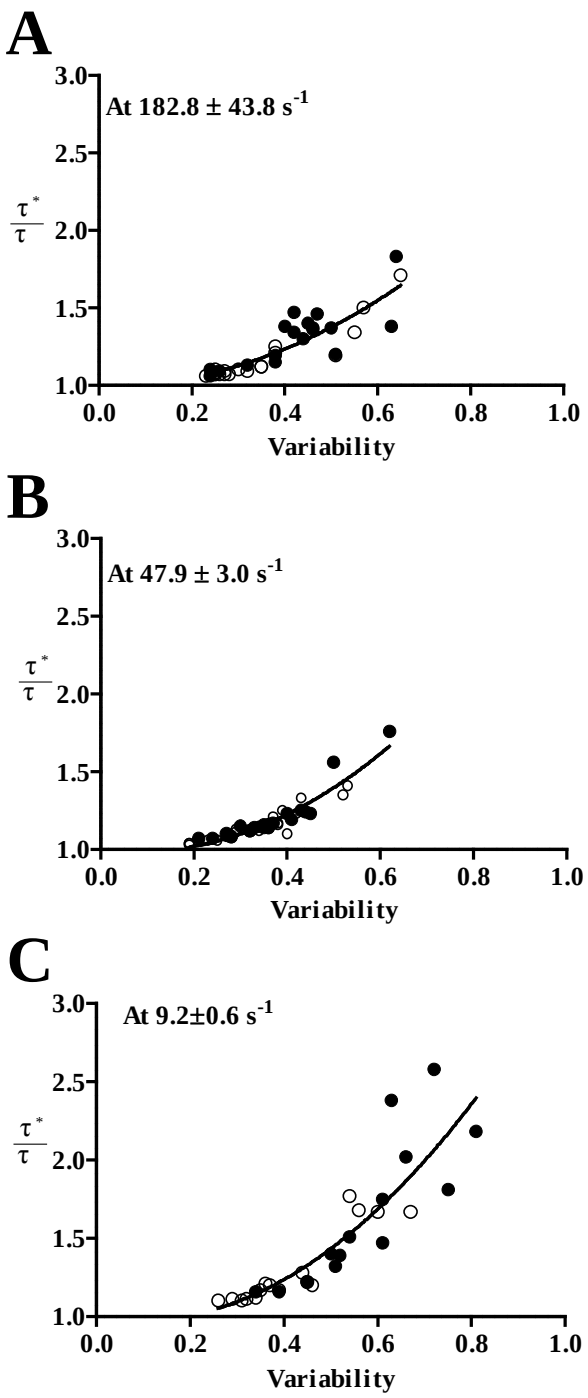

Figure V-4: Ratio between estimated WSS values with (τ^*) and without (τ) consideration of the variation in CFL as a function of the layer variability.
The non-linear regression was performed with a quadratic function ($y = B_0 + B_1x + B_2x^2$, where B_0 is 1) for the combined group (before (○) and after (●) dextran treatment). $y = 1 - 0.07x + 1.64x^2$; $R^2 = 0.76$ at 182.8 ± 43.8 s^{-1}. $y = 1 - 0.36x + 2.31x^2$; $R^2 = 0.88$ at 47.9 ± 3.0 s^{-1}. $y = 1 - 0.52x + 2.77x^2$; $R^2 = 0.77$ at 9.2 ± 0.6 s^{-1}.

5. Discussion

5.1 Limitations in WSS approximation

In this study, the averaged edge velocity of RBC core was used in estimation of the WSS although blood flow might still be unsteady in arterioles [88, 118]. We have previously pointed out that during the cardiac cycle, the edge velocity of the RBC core at normal arterial pressure might vary by ± 6%-7% from the mean value [50]. Therefore, by considering the pulsatile nature of the arteriolar flow, the actual variation of the WSS may differ from our estimation by a maximum of 6%-7%. However, under reduced flow conditions, the flow pulsatility would be much lower than that in normal flow conditions. Thus, effects of the unsteady flow on the WSS estimation in low shear conditions may not be as significant. The spatial resolution of the CFL width measurement with the current microscope system was reported to be ~0.4 μm [50, 84], which limits the accuracy of our WSS estimation since one of the key parameters in Eq. (2) determining the WSS is the width of the CFL. Thus, variability in the layer width smaller than the systemic spatial resolution cannot be detected with the current system.

5.2 Estimated arteriolar WSS

A number of studies have provided information on arteriolar WSS in a variety of species and tissues. The WSS in resting cat sartorius muscle arterioles (~60 μm ID) was estimated to be ~6 Pa with bulk viscosity of blood at 45% hematocrit [88]. A previous study carried out with the rat cremaster muscle estimated the WSS to be approximately

1.0-4.5 Pa in larger arterioles (160-220 μm ID) using 3.8 cP of blood viscosity [6]. In a recent review by Reneman and Hoeks [101], the WSS in mesenteric arterioles was found to be 0.51-5.0 Pa in rabbits and 4.71 ± 2.34 Pa in cats. Pries and coworkers [93] reported that the WSS of ~5 Pa with a substantial variation observed in rat mesenteric arterioles (>15 μm ID). In the present study, the mean arteriolar WSS varied from ~0.3 to 7.5 Pa under normal and reduced flow conditions, which is in agreement with the range of values reported in previous studies. However, since the WSS is a function of several rheological conditions such as vessel size, viscosity, and flow velocity, it may not be feasible to directly compare the WSS values under different physiological and rheological situations.

5.3 Effect of aggregation on CFL variability and WSS

As shown in Figure V-3, the variability of the CFL significantly ($P < 0.01$) increased after dextran treatment only at 9.2 ± 0.6 s^{-1}, which was reflected in a shift of the variability range towards higher magnitudes after dextran infusion in Figure V-4C. Although there were no statistical differences in the variability before and after dextran treatment at the other two shear rates (182.8 ± 43.8 and 47.9 ± 3.0 s^{-1}), it appeared to be consistent that the variability increased after dextran treatment. These findings were in consensus with those reported in previous *in vitro* [2] and *in vivo* studies [50, 84] performed in narrow vertical tubes (28-101 μm ID) perfused with human blood and in arterioles in rat cremaster muscle (10-60 μm ID), respectively. The results in the present study imply that RBC aggregation may play a major role in altering the CFL variability,

in particular at regions of blood flow characterized by low pseudoshear rates (< 10 s^{-1}). Similarly, our earlier *in vivo* studies [50, 84] have substantiated that apparent changes in CFL characteristics under similar aggregating conditions are only observed at low pseudoshear rates (< 50 s^{-1}). It should be noted that pseudoshear rates used in this study were based on the flow velocity near the vessel wall, whose magnitude would be less than that of mean cellular velocity. Therefore, for the same flow conditions, the pseudoshear rates reported here should be smaller than those in previous studies, which were based on the mean cellular velocity.

As shown in Figure V-4, the layer variability ranged approximately from 0.2 to 0.6 even without dextran induction under similar flow conditions. It should be noted that the variability data were obtained from 12 arterioles which can have different local hematocrits. Furthermore, it is well known that local hematocrits can take on a wide range of values even for vessels of the same order in the same arteriolar network [42]. Since CFL characteristics are dependent on hematocrit, it is expected that the CFL can exhibit a wide range of variability between similar diameter vessels even in the absence of RBC aggregation or under similar flow conditions.

The results shown in Figure V-4 suggest that the variability of the CFL can be an important parameter which causes an elevation of the WSS, particularly at low pseudoshear rates where RBC aggregation could enhance the layer variability. In a computational study by Sharan and Popel [109], they showed that the effective blood viscosity near the vessel wall increased with greater interface roughness between RBC core and the CFL in vessel ranges of 25-70 μm at 45% hematocrit. Their finding is qualitatively in agreement to that in the present study, as an increased effective viscosity

would lead to an augmentation in WSS. Therefore, we emphasize here the importance of considering the CFL variation in WSS determination which otherwise could result in an underestimation of the WSS, by as much as two folds, with high variability (~0.7) observed under aggregating condition at $9.2 \pm 0.6\ s^{-1}$ (see Figure V-4).

Figures V-5A and B represent respective conceptual sketches of flowing RBCs in a vessel illustrating the effect of temporal variation in the CFL on WSS. By keeping the mean CFL constant, we compared between two cases, one without variability of the layer (Figure V-5A) and another with variability of the layer (Figure V-5B). When the WSS was obtained from blood flow without variability of the layer, a mean WSS of lower magnitude was obtained as compared to the situation where variability of the layer is present. Previous studies [50, 84] have shown that a wider CFL would allow a higher degree of variability of the layer and vice versa. In the event where the magnitude of WSS is small due to a thick CFL, the corresponding large variability in the layer may partially compensate this effect by augmenting the WSS. It should be further noted that for there to be no change in WSS on the average, individual CFL width data points have to be symmetrically distributed about their mean value. As shown by our previous study [84], the layer width data points follow a non-Gaussian distribution and therefore are not symmetrical about their mean value, hence a change in WSS on the average is expected.

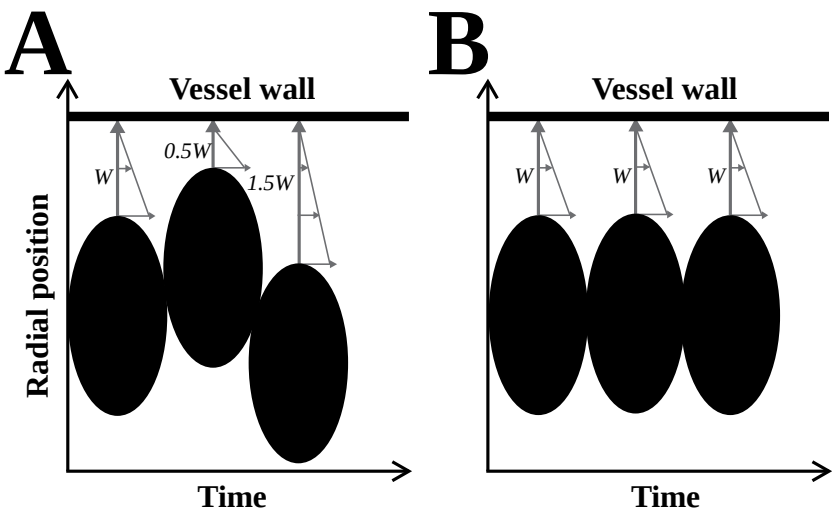

$Mean\,CFL = W$

$\tau^* = 1.22\mu \frac{V_{edge}}{W}$

$Mean\,CFL = W$

$\tau = \mu \frac{V_{edge}}{W}$

Figure V-5: Two-dimensional sketch of RBCs flowing in a vessel illustrating the effect of temporal variation in the CFL on wall shear stress.
A and B represent two different situations for τ^* (with consideration of the layer variation) and τ (without consideration of the layer variation). The same cellular velocity was assumed in the two situations. Black ellipsoids represent individual RBCs.

5.4 Physiological implication

The inverse relationship between the CFL width and the WSS suggests that NO production could be inevitably affected by the layer formation since WSS is a mechanical stimulus for endothelium-derived nitric oxide (NO) synthesis. However, overall NO bioavailability that ultimately influences vascular tone would also be dependent on other physiological aspects associated with the layer. The CFL could act as a diffusion barrier that could potentially minimize NO scavenging by the RBCs.[18, 47, 58] In addition, we presented here the possibility of CFL variability to improve NO preservation by enhancing the WSS. All of these factors may contribute to the local regulatory mechanism of vasodilation. In normal flow conditions, it is likely that the WSS can sufficiently stimulate the production of NO in the endothelium, in a way that could cancel out any potential scavenging effect of NO by the RBCs. On the contrary, in low flow conditions, the diminishing magnitude of the WSS acting on the endothelium due to the effects of lower hydrodynamic forces and more prominent CFL formation in the presence of aggregation can attenuate NO production. It has been demonstrated that enhanced RBC aggregation in suspensions used for perfusion of glass capillaries led to the down-regulation of NO synthesizing mechanisms in human umbilical vein ECs coating the capillaries.[122] In vivo studies have also supported this finding.[12] In contrast, our findings would suggest that an enhanced layer variability due to aggregation induction could oppose the above response on endothelial NO production by augmenting the WSS. It should be noted that this variability effect might be offset by reduction of WSS due to the thicker CFL.

CHAPTER VI: CONCLUSIONS AND RECOMMENDATIONS FOR FUTURE STUDIES

The study in CHAPTER II examined four different histogram-based threholding algorithms (Otsu's intermodes, minimum and 2nd peak) to provide a technical suggestion on the selection of a suitable thresholding algorithm for the CFL width measurement. The results showed that, with our current microscopic system, the CFL width determined by the minimum algorithm was in the best agreement with the manual measurement. However, it should be noted that the accuracy of the automated methods for determination of the CFL width would depend on the image quality, in particular the contrast between the RBC core and the background which would differ among microscopic systems. Therefore, one may need to examine several appropriate thresholding methods for selecting the best suitable algorithm based on their experimental conditions.

The study in CHAPTER III provided a detailed insight into the dynamic changes of CFL width in a circular microtube with 25-μm diameter at both physiological and pathological levels of RBC aggregation seen in humans. RBC aggregation at hyper-levels prominently enhanced the mean CFL width and attenuated the RBC-wall contact frequency. In addition, the enhanced aggregating tendency from none to hyper levels significantly enlarged the cell-free area (CFA) ($P < 0.01$). The RBC aggregation at pathological levels would promote not only the CFL formation (one-dimensional parameter) but also the CFA variation (two-dimensional parameter) in both spatial and temporal domains. The comparison of those results from *in vitro* with that obtained *in*

vivo showed significantly different results due to difference in flow environments such as the presence of glycocalyx and the limited distance for flow development.

The study in CHAPTER IV proposed a new numerical model capable of predicting changes in the CFL width in narrow tubes while considering RBC aggregation effects. The CFL width was strongly modulated by the relative viscosity function. Aggregation increased the CFL width and this effect became more pronounced at low shear rates. The CFL widths predicted in the present study at high shear conditions were in agreement with those reported in previous studies. Further improvement of the present model would be needed to consider effects of RBC deformability changes and particle interaction among RBCs. However, unlike previous multi-particle models, our model did not require a high computing cost. Moreover, it was capable of reproducing results for a thicker CFL width at low shear conditions, depending on RBC aggregation tendency.

The study in CHAPTER V examined the effect of CFL variation on the arteriolar WSS. The salient finding of this study was that the CFL variability in arterioles was significantly augmented by aggregation at reduced flow rates which in turn could potentially lead to an enhancement of WSS in the arterioles. The WSS estimated without taking into account the CFL variation showed an underestimation of its value than that considering the variation. Therefore, the CFL variation should be considered in WSS determination, particularly in the presence of RBC aggregation under reduced flow conditions. However, in this study, the glycocalyx layer on the endothelium was not considered in WSS determination. Hence, the glycocalyx layer requires further study in order to render the WSS information more relevant to clinical applications.

Conclusion & Future studies

In conclusion, the present dissertation provides detailed insight into the relationship between RBC aggregation and CFL width change using experimental and numerical approaches. Furthermore, the present dissertation proposes important rheological effects of CFL on arteriolar WSS and its modulation by RBC aggregation.

BIBLIOGRAPHY

1. Abkarian, M. and A. Viallat, Vesicles and red blood cells in shear flow. *Soft Matter*, 4(4): 653-657, 2008.
2. Alonso, C., A.R. Pries, and P. Gaehtgens, Time-dependent rheological behavior of blood at low shear in narrow vertical tubes. *The American journal of physiology*, 265(2 Pt 2): H553-61, 1993.
3. Ami, R.B., G. Barshtein, D. Zeltser, Y. Goldberg, I. Shapira, A. Roth, G. Keren, H. Miller, V. Prochorov, A. Eldor, S. Berliner, and S. Yedgar, Parameters of red blood cell aggregation as correlates of the inflammatory state. *American journal of physiology. Heart and circulatory physiology*, 280(5): H1982-8, 2001.
4. Baez, S., Open Cremaster Muscle Preparation for Study of Blood-Vessels by in-Vivo Microscopy. *Microvascular research*, 5(3): 384-394, 1973.
5. Bagchi, P., Mesoscale simulation of blood flow in small vessels. *Biophysical journal*, 92(6): 1858-77, 2007.
6. Bakker, E.N.T.P., J.P. Versluis, P. Sipkema, J.W.G.E. VanTeeffelen, T.M. Rolf, J.A.E. Spaan, and E. VanBavel, Differential structural adaptation to haemodynamics along single rat cremaster arterioles. *The Journal of physiology*, 548(Pt 2): 549-55, 2003.
7. Barbee, K.A., Role of subcellular shear-stress distributions in endothelial cell mechanotransduction. *Annals of biomedical engineering*, 30(4): 472-82, 2002.
8. Baskurt, O.K., M. Bor-Kucukatay, O. Yalcin, and H.J. Meiselman, Aggregation behavior and electrophoretic mobility of red blood cells in various mammalian species. *Biorheology*, 37(5-6): 417-28, 2000.
9. Baskurt, O.K., M. Bor-Kucukatay, O. Yalcin, H.J. Meiselman, and J.K. Armstrong, Standard aggregating media to test the "aggregability" of rat red blood cells. *Clin Hemorheol Microcirc*, 22(2): 161-6, 2000.
10. Baskurt, O.K., R.A. Farley, and H.J. Meiselman, Erythrocyte aggregation tendency and cellular properties in horse, human, and rat: a comparative study. *The American journal of physiology*, 273(6 Pt 2): H2604-12, 1997.

11. Baskurt, O.K., A. Temiz, and H.J. Meiselman, Red blood cell aggregation in experimental sepsis. *The Journal of laboratory and clinical medicine*, 130(2): 183-90, 1997.
12. Baskurt, O.K., O. Yalcin, S. Ozdem, J.K. Armstrong, and H.J. Meiselman, Modulation of endothelial nitric oxide synthase expression by red blood cell aggregation. *American journal of physiology. Heart and circulatory physiology*, 286(1): H222-9, 2004.
13. Ben-Ami, R., G. Sheinman, S. Yedgar, A. Eldor, A. Roth, A.S. Berliner, and G. Barshtein, Thrombolytic therapy reduces red blood cell aggregation in plasma without affecting intrinsic aggregability. *Thrombosis Research*, 105(6): 487-492, 2002.
14. Bishop, J.J., P.R. Nance, A.S. Popel, M. Intaglietta, and P.C. Johnson, Effect of erythrocyte aggregation on velocity profiles in venules. *American journal of physiology. Heart and circulatory physiology*, 280(1): H222-36, 2001.
15. Bishop, J.J., P.R. Nance, A.S. Popel, M. Intaglietta, and P.C. Johnson, Erythrocyte margination and sedimentation in skeletal muscle venules. *Am J Physiol Heart Circ Physiol*, 281(2): H951-8, 2001.
16. Bishop, J.J., A.S. Popel, M. Intaglietta, and P.C. Johnson, Effect of aggregation and shear rate on the dispersion of red blood cells flowing in venules. *American journal of physiology. Heart and circulatory physiology*, 283(5): H1985-96, 2002.
17. Bugliarello, G. and J. Sevilla, Velocity distribution and other characteristics of steady and pulsatile blood flow in fine glass tubes. *Biorheology*, 7(2): 85-107, 1970.
18. Butler, A.R., I.L. Megson, and P.G. Wright, Diffusion of nitric oxide and scavenging by blood in the vasculature. *Biochimica et biophysica acta*, 1425(1): 168-76, 1998.
19. Buxbaum, K., E. Evans, and D.E. Brooks, Quantitation of Surface Affinities of Red-Blood-Cells in Dextran Solutions and Plasma. *Biochemistry*, 21(13): 3235-3239, 1982.

20. Cabrales, P., A.G. Tsai, P.C. Johnson, and M. Intaglietta, Oxygen release from arterioles with normal flow and no-flow conditions. *Journal of applied physiology (Bethesda, Md. : 1985)*, 100(5): 1569-76, 2006.
21. Chan, R.H., C.-W. Ho, and M. Nikolova, Salt-and-Pepper noise removal by median-type noise detectors and detail-preserving regularization. *IEEE transactions on image processing : a publication of the IEEE Signal Processing Society*, 14(10): 1479-85, 2005.
22. Chen, X., D. Jaron, K.A. Barbee, and D.G. Buerk, The influence of radial RBC distribution, blood velocity profiles, and glycocalyx on coupled NO/O2 transport. *Journal of applied physiology (Bethesda, Md. : 1985)*, 100(2): 482-92, 2006.
23. Cheng, C., D. Tempel, A. Oostlander, F. Helderman, F. Gijsen, J. Wentzel, R. van Haperen, D.B. Haitsma, P.W. Serruys, A.F. van der Steen, R. de Crom, and R. Krams, Rapamycin modulates the eNOS vs. shear stress relationship. *Cardiovasc Res*, 78(1): 123-9, 2008.
24. Chien, S., Mechanotransduction and endothelial cell homeostasis: the wisdom of the cell. *American journal of physiology. Heart and circulatory physiology*, 292(3): H1209-24, 2007.
25. Chien, S., S. Usami, R.J. Dellenback, and M.I. Gregersen, Shear-dependent deformation of erythrocytes in rheology of human blood. *The American journal of physiology*, 219(1): 136-42, 1970.
26. Cho, Y.I., M.P. Mooney, and D.J. Cho, Hemorheological disorders in diabetes mellitus. *Journal of diabetes science and technology*, 2(6): 1130-8, 2008.
27. Cicco, G., P. Vicenti, G.D. Stingi, M.S. Tarallo, and A. Pirrelli, Hemorheology in complicated hypertension. *Clinical hemorheology and microcirculation*, 21(3-4): 315-319, 1999.
28. Cokelet, G.R. and H.L. Goldsmith, Decreased hydrodynamic resistance in the two-phase flow of blood through small vertical tubes at low flow rates. *Circulation research*, 68(1): 1-17, 1991.
29. Crowl, L.M. and A.L. Fogelson, Computational model of whole blood exhibiting lateral platelet motion induced by red blood cells. *Int j numer method biomed eng*, 26(3-4): 471-487, 2010.

30. Das, B., J.J. Bishop, S. Kim, H.J. Meiselman, P.C. Johnson, and A.S. Popel, Red blood cell velocity profiles in skeletal muscle venules at low flow rates are described by the Casson model. *Clin Hemorheol Microcirc*, 36(3): 217-33, 2007.
31. Das, B., G. Enden, and A.S. Popel, Stratified multiphase model for blood flow in a venular bifurcation. *Annals of biomedical engineering*, 25(1): 135-53, 1997.
32. Das, B., P.C. Johnson, and A.S. Popel, Effect of nonaxisymmetric hematocrit distribution on non-Newtonian blood flow in small tubes. *Biorheology*, 35(1): 69-87, 1998.
33. Eckmann, D.M., S. Bowers, M. Stecker, and A.T. Cheung, Hematocrit, volume expander, temperature, and shear rate effects on blood viscosity. *Anesth Analg*, 91(3): 539-45, 2000.
34. El-Farra, N.H., P.D. Christofides, and J.C. Liao, Analysis of nitric oxide consumption by erythrocytes in blood vessels using a distributed multicellular model. *Annals of biomedical engineering*, 31(3): 294-309, 2003.
35. Falcó, C., A. Vayá, M. Simó, T. Contreras, M. Santaolaria, and J. Aznar, Influence of fibrinogen levels on erythrocyte aggregation determined with the Myrenne aggregometer and the Sefam erythro-aggregometer. *Clinical hemorheology and microcirculation*, 33(2): 145-51, 2005.
36. Fedosov, D.A., B. Caswell, A.S. Popel, and G.E. Karniadakis, Blood flow and cell-free layer in microvessels. *Microcirculation (New York, N.Y. : 1994)*, 17(8): 615-28, 2010.
37. Fung, Y.C., W.C. Tsang, and P. Patitucci, High-resolution data on the geometry of red blood cells. *Biorheology*, 18(3-6): 369-85, 1981.
38. Glasbey, C.A., An analysis of histogram based thresholding algorithms. *CVGIP: Graphical models and image processing*, 55(6): 532-537, 1993.
39. Goldsmith, H.L., The Microcirculatory Society Eugene M. Landis Award lecture. The microrheology of human blood. *Microvascular research*, 31(2): 121-42, 1986.
40. Greensmith, J.E. and B.R. Duling, Morphology of the constricted arteriolar wall: physiological implications. *The American journal of physiology*, 247(5 Pt 2): H687-98, 1984.

41. Horiuchi, T., H.H. Dietrich, K. Hongo, T. Goto, and R.G. Dacey, Role of endothelial nitric oxide and smooth muscle potassium channels in cerebral arteriolar dilation in response to acidosis. *Stroke; a journal of cerebral circulation*, 33(3): 844-9, 2002.

42. House, S.D. and H.H. Lipowsky, Microvascular hematocrit and red cell flux in rat cremaster muscle. *The American journal of physiology*, 252(1 Pt 2): H211-22, 1987.

43. Intaglietta, M., D.R. Richardson, and W.R. Tompkins, Blood pressure, flow, and elastic properties in microvessels of cat omentum. *The American journal of physiology*, 221(3): 922-8, 1971.

44. Kanai, A.J., H.C. Strauss, G.A. Truskey, A.L. Crews, S. Grunfeld, and T. Malinski, Shear stress induces ATP-independent transient nitric oxide release from vascular endothelial cells, measured directly with a porphyrinic microsensor. *Circulation research*, 77(2): 284-93, 1995.

45. Katritsis, D., L. Kaiktsis, A. Chaniotis, J. Pantos, E.P. Efstathopoulos, and V. Marmarelis, Wall shear stress: theoretical considerations and methods of measurement. *Progress in cardiovascular diseases*, 49(5): 307-29, 2007.

46. Kavdia, M. and A.S. Popel, Wall shear stress differentially affects NO level in arterioles for volume expanders and Hb-based O2 carriers. *Microvascular research*, 66(1): 49-58, 2003.

47. Kavdia, M., N.M. Tsoukias, and A.S. Popel, Model of nitric oxide diffusion in an arteriole: impact of hemoglobin-based blood substitutes. *American journal of physiology. Heart and circulatory physiology*, 282(6): H2245-53, 2002.

48. Kim, A., H. Dadgostar, G.N. Holland, R. Wenby, F. Yu, B.G. Terry, and H.J. Meiselman, Hemorheologic abnormalities associated with HIV infection: altered erythrocyte aggregation and deformability. *Investigative ophthalmology & visual science*, 47(9): 3927-32, 2006.

49. Kim, S., R.L. Kong, A.S. Popel, M. Intaglietta, and P.C. Johnson, A computer-based method for determination of the cell-free layer width in microcirculation. *Microcirculation (New York, N.Y. : 1994)*, 13(3): 199-207, 2006.

50. Kim, S., R.L. Kong, A.S. Popel, M. Intaglietta, and P.C. Johnson, Temporal and spatial variations of cell-free layer width in arterioles. *American journal of physiology. Heart and circulatory physiology*, 293(3): H1526-35, 2007.

51. Kim, S., P.K. Ong, O. Yalcin, M. Intaglietta, and P.C. Johnson, The cell-free layer in microvascular blood flow. *Biorheology*, 46(3): 181-9, 2009.

52. Kim, S., A.S. Popel, M. Intaglietta, and P.C. Johnson, Effect of erythrocyte aggregation at normal human levels on functional capillary density in rat spinotrapezius muscle. *American journal of physiology. Heart and circulatory physiology*, 290(3): H941-7, 2006.

53. Kim, S., A.S. Popel, M. Intaglietta, and P.C. Johnson, Effect of erythrocyte aggregation at normal human levels on functional capillary density in rat spinotrapezius muscle. *Am J Physiol Heart Circ Physiol*, 290(3): H941-7, 2006.

54. Kim, S., S. Yang, and D. Lim, Effect of dextran on rheological properties of rat blood. *Journal of Mechanical Science and Technology*, 23: 868, 2009.

55. Kittler, J. and J. Illingworth, On threshold selection using clustering criteria. *IEEE transactions on systems, man, and cybernetics*, 15(5): 652-654, 1985.

56. Kuchan, M.J. and J.A. Frangos, Role of calcium and calmodulin in flow-induced nitric oxide production in endothelial cells. *The American journal of physiology*, 266(3 Pt 1): C628-36, 1994.

57. Lamkin-Kennard, K.A., D. Jaron, and D.G. Buerk, Impact of the Fahraeus effect on NO and O2 biotransport: a computer model. *Microcirculation (New York, N.Y. : 1994)*, 11(4): 337-49, 2004.

58. Lamkin-Kennard, K.A., D. Jaron, and D.G. Buerk, Impact of the Fåhraeus effect on NO and O2 biotransport: a computer model. *Microcirculation (New York, N.Y. : 1994)*, 11(4): 337-49, 2004.

59. Lee, B.K., A. Durairaj, A. Mehra, R.B. Wenby, H.J. Meiselman, and T. Alexy, Microcirculatory dysfunction in cardiac syndrome X: role of abnormal blood rheology. *Microcirculation (New York, N.Y. : 1994)*, 15(5): 451-9, 2008.

60. Lee, H. and R.-H. Park, Comments on an optimal multiple threshold scheme for image segmentation. *IEEE transactions on systems, man, and cybernetics*, 20(3): 741-2, 1990.

61. Lipowsky, H.H., S. Kovalcheck, and B.W. Zweifach, The distribution of blood rheological parameters in the microvasculature of cat mesentery. *Circulation research*, 43(5): 738-49, 1978.

62. Lominadze, D., I.G. Joshua, and D.A. Schuschke, Increased erythrocyte aggregation in spontaneously hypertensive rats. *American Journal of Hypertension*, 11(7): 784-789, 1998.

63. Long, D.S., M.L. Smith, A.R. Pries, K. Ley, and E.R. Damiano, Microviscometry reveals reduced blood viscosity and altered shear rate and shear stress profiles in microvessels after hemodilution. *Proceedings of the National Academy of Sciences of the United States of America*, 101(27): 10060-5, 2004.

64. Luquita, A., L. Urli, M.J. Svetaz, A.M. Gennaro, R. Volpintesta, S. Palatnik, and M. Rasia, Erythrocyte aggregation in rheumatoid arthritis: Cell and plasma factor's role. *Clin Hemorheol Microcirc*, 41(1): 49-56, 2009.

65. Maeda, N., Erythrocyte rheology in microcirculation. *The Japanese journal of physiology*, 46(1): 1-14, 1996.

66. Maeda, N., Y. Suzuki, J. Tanaka, and N. Tateishi, Erythrocyte flow and elasticity of microvessels evaluated by marginal cell-free layer and flow resistance. *The American journal of physiology*, 271(6 Pt 2): H2454-61, 1996.

67. Makena Hightower, C., B.Y. Salazar Vazquez, S. Woo Park, K. Sriram, J. Martini, O. Yalcin, A.G. Tsai, P. Cabrales, D.M. Tartakovsky, P.C. Johnson, and M. Intaglietta, Integration of cardiovascular regulation by the blood/endothelium cell-free layer. *Wiley Interdiscip Rev Syst Biol Med*, 3(4): 458-70, 2011.

68. Marton, Z., G. Kesmarky, J. Vekasi, A. Cser, R. Russai, B. Horvath, and K. Toth, Red blood cell aggregation measurements in whole blood and in fibrinogen solutions by different methods. *Clinical hemorheology and microcirculation*, 24(2): 75-83, 2001.

69. Mashour, G.A. and R.J. Boock, Effects of shear stress on nitric oxide levels of human cerebral endothelial cells cultured in an artificial capillary system. *Brain Res*, 842(1): 233-8, 1999.

70. McDonald, D.A., Hemodynamics. *Annu Rev Physiol*, 30: 525-56, 1968.

71. McHedlishvili, G. and N. Maeda, Blood flow structure related to red cell flow: A determinant of blood fluidity in narrow microvessels. *The Japanese journal of physiology*, 51(1): 19-30, 2001.

72. Meininger, G.A., K.L. Fehr, and M.B. Yates, Anatomic and hemodynamic characteristics of the blood vessels feeding the cremaster skeletal muscle in the rat. *Microvascular research*, 33(1): 81-97, 1987.

73. Meiselman, H.J., Red blood cell aggregation: 45 years being curious. *Biorheology*, 46(1): 1-19, 2009.

74. Monsuez, J.J., J. Dufaux, D. Vittecoq, P. Flaud, and E. Vicaut, Hemorheology in asymptomatic HIV-infected patients. *Clin Hemorheol Microcirc*, 23(1): 59-66, 2000.

75. Moyers-Gonzalez, M.A. and R.G. Owens, Mathematical modelling of the cell-depleted peripheral layer in the steady flow of blood in a tube. *Biorheology*, 47(1): 39-71, 2010.

76. Namgung, B., P.K. Ong, Y.H. Wong, D. Lim, K.J. Chun, and S. Kim, A comparative study of histogram-based thresholding methods for the determination of cell-free layer width in small blood vessels. *Physiological measurement*, 31(9): N61-N70, 2010.

77. Nash, G.B. and H.J. Meiselman, Effects of Dextran and Polyvinylpyrrolidone on Red-Cell Geometry and Membrane Elasticity. *Annals of the New York Academy of Sciences*, 416(Dec): 255-262, 1983.

78. Neu, B., J.K. Armstrong, T.C. Fisher, and H.J. Meiselman, Aggregation of human RBC in binary dextran-PEG polymer mixtures. *Biorheology*, 38(1): 53-68, 2001.

79. Ohta, K., F. Gotoh, M. Tomita, N. Tanahashi, M. Kobari, T. Shinohara, Y. Terayama, B. Mihara, and H. Takeda, Animal Species-Differences in Erythrocyte Aggregability. *American Journal of Physiology*, 262(4): H1009-H1012, 1992.

80. Ong, P.K., S. Jain, and S. Kim, Modulation of NO Bioavailability by Temporal Variation of the Cell-Free Layer Width in Small Arterioles. *Annals of biomedical engineering*, 39(3): 1012-1023, 2011.

81. Ong, P.K., S. Jain, and S. Kim, Temporal variations of the cell-free layer width may enhance NO bioavailability in small arterioles: Effects of erythrocyte aggregation. *Microvascular research*, 81(3): 303-12, 2011.

82. Ong, P.K., S. Jain, and S. Kim, Spatio-temporal variations in cell-free layer formation near bifurcations of small arterioles. *Microvascular research*, 83(2): 118-25, 2012.

83. Ong, P.K., S. Jain, B. Namgung, Y.I. Woo, and S. Kim, Cell-free layer formation in small arterioles at pathological levels of erythrocyte aggregation. *Microcirculation (New York, N.Y. : 1994)*, 18(7): 541-51, 2011.

84. Ong, P.K., B. Namgung, P.C. Johnson, and S. Kim, Effect of erythrocyte aggregation and flow rate on cell-free layer formation in arterioles. *American journal of physiology. Heart and circulatory physiology*, 298(6): H1870-8, 2010.

85. Otsu, N., A threshold selection method from gray-level histograms. *IEEE transactions on systems, man, and cybernetics*, 9(1): 62-66, 1979.

86. Ozanne, P., R.B. Francis, and H.J. Meiselman, Red blood cell aggregation in nephrotic syndrome. *Kidney international*, 23(3): 519-25, 1983.

87. Pittner, J., M. Wolgast, D. Casellas, and A.E.G. Persson, Increased shear stress-released NO and decreased endothelial calcium in rat isolated perfused juxtamedullary nephrons. *Kidney international*, 67(1): 227-36, 2005.

88. Popel, A.S. and P.C. Johnson, Microcirculation and Hemorheology. *Annual review of fluid mechanics*, 37: 43-69, 2005.

89. Popel, A.S., P.C. Johnson, M.V. Kameneva, and M.A. Wild, Capacity for red blood cell aggregation is higher in athletic mammalian species than in sedentary species. *Journal of applied physiology (Bethesda, Md. : 1985)*, 77(4): 1790-4, 1994.

90. Prewitt, J.M. and M.L. Mendelsohn, The analysis of cell images. *Annals of the New York Academy of Sciences*, 128(3): 1035-53, 1966.

91. Pribush, A., D. Zilberman-Kravits, and N. Meyerstein, The mechanism of the dextran-induced red blood cell aggregation. *European biophysics journal : EBJ*, 36(2): 85-94, 2007.

92. Pries, A.R., D. Neuhaus, and P. Gaehtgens, Blood viscosity in tube flow: dependence on diameter and hematocrit. *The American journal of physiology*, 263(6 Pt 2): H1770-8, 1992.

93. Pries, A.R., T.W. Secomb, and P. Gaehtgens, Design principles of vascular beds. *Circulation research*, 77(5): 1017-23, 1995.

94. Pries, A.R., T.W. Secomb, and P. Gaehtgens, Biophysical aspects of blood flow in the microvasculature. *Cardiovasc Res*, 32(4): 654-67, 1996.

95. Pries, A.R., T.W. Secomb, T. Gessner, M.B. Sperandio, J.F. Gross, and P. Gaehtgens, Resistance to blood flow in microvessels in vivo. *Circulation research*, 75(5): 904-15, 1994.

96. Qiao, Y., Q. Hu, G. Qian, S. Luo, and W.L. Nowinski, Thresholding based on variance and intesity contrast. *Pattern recognition*, 40: 596-608, 2007.

97. Rad, S., J. Gao, H.J. Meiselman, O.K. Baskurt, and B. Neu, Depletion of high molecular weight dextran from the red cell surface measured by particle electrophoresis. *Electrophoresis*, 30(3): 450-6, 2009.

98. Razavian, S.M., M. Del Pino, A. Simon, and J. Levenson, Increase in erythrocyte disaggregation shear stress in hypertension. *Hypertension*, 20(2): 247-52, 1992.

99. Reinke, W., P. Gaehtgens, and P.C. Johnson, Blood viscosity in small tubes: effect of shear rate, aggregation, and sedimentation. *The American journal of physiology*, 253(3 Pt 2): H540-7, 1987.

100. Reneman, R.S., T. Arts, and A.P.G. Hoeks, Wall shear stress--an important determinant of endothelial cell function and structure--in the arterial system in vivo. Discrepancies with theory. *Journal of vascular research*, 43(3): 251-69, 2006.

101. Reneman, R.S. and A.P.G. Hoeks, Wall shear stress as measured in vivo: consequences for the design of the arterial system. *Medical & biological engineering & computing*, 46(5): 499-507, 2008.

102. Resnick, N., H. Yahav, A. Shay-Salit, M. Shushy, S. Schubert, L.C.M. Zilberman, and E. Wofovitz, Fluid shear stress and the vascular endothelium: for better and for worse. *Progress in biophysics and molecular biology*, 81(3): 177-99, 2003.

103. Robertson, A.M., A. Sequeira, and M.V. Kameneva, Hemodynamical Flows, in Hemorheology, *Birkhäuser Basel*, 37: 63-120, 2008.

104. Sakai, H., A. Sato, N. Okuda, S. Takeoka, N. Maeda, and E. Tsuchida, Peculiar flow patterns of RBCs suspended in viscous fluids and perfused through a narrow tube (25 μm). *American journal of physiology. Heart and circulatory physiology*, 297(2): H583-9, 2009.

105. Savery, M.D. and E.R. Damiano, The endothelial glycocalyx is hydrodynamically relevant in arterioles throughout the cardiac cycle. *Biophysical journal*, 95(3): 1439-47, 2008.

106. Schmid-Schönbein, H., P. Gaehtgens, and H. Hirsch, On the shear rate dependence of red cell aggregation in vitro. *The Journal of clinical investigation*, 47(6): 1447-1454, 1968.

107. Sezan, M.I., A peak detection algorithm and its application to histogram-based image data reduction. *Computer Vision, Graphics, and Image Processing*, 29: 47-59, 1985.

108. Sezgin, M. and B. Sankur, Survey over image thresholding techniques and quatitative performance evaluation. *Journal of Electronic Imaging*, 13(1): 146-165, 2004.

109. Sharan, M. and A.S. Popel, A two-phase model for flow of blood in narrow tubes with increased effective viscosity near the wall. *Biorheology*, 38(5-6): 415-28, 2001.

110. Shen, Z. and H.H. Lipowsky, Image enhancement of the in vivo leukocyte-endothelium contact zone using optical sectioning microscopy. *Annals of biomedical engineering*, 25(3): 521-35, 1997.

111. Silva, J. and M. Intaglietta, The correlation of photometric signals derived from in vivo red blood cell flow in microvessels. *Microvascular research*, 7(2): 156-69, 1974.

112. Soutani, M., Y. Suzuki, N. Tateishi, and N. Maeda, Quantitative evaluation of flow dynamics of erythrocytes in microvessels: influence of erythrocyte aggregation. *The American journal of physiology*, 268(5 Pt 2): H1959-65, 1995.

113. Sriram, K., B.Y. Salazar Vazquez, A.G. Tsai, P. Cabrales, M. Intaglietta, and D.M. Tartakovsky, Autoregulation and mechanotransduction control the arteriolar response to small changes in hematocrit. *American journal of physiology. Heart and circulatory physiology*, doi:10.1152/ajpheart.00438.2012, 2012.

114. Sriram, K., B.Y. Vazquez, O. Yalcin, P.C. Johnson, M. Intaglietta, and D.M. Tartakovsky, The effect of small changes in hematocrit on nitric oxide transport in arterioles. *Antioxid Redox Signal*, 14(2): 175-85, 2011.

115. Suzuki, Y., N. Tateishi, and N. Maeda, Electrostatic repulsion among erythrocytes in tube flow, demonstrated by the thickness of marginal cell-free layer. *Biorheology*, 35(2): 155-70, 1998.

116. Tateishi, N., Y. Suzuki, M. Soutani, and N. Maeda, Flow dynamics of erythrocytes in microvessels of isolated rabbit mesentery: cell-free layer and flow resistance. *Journal of biomechanics*, 27(9): 1119-25, 1994.

117. Tomiyama, Y., J.E. Brian, and M.M. Todd, Plasma viscosity and cerebral blood flow. *American journal of physiology. Heart and circulatory physiology*, 279(4): H1949-54, 2000.

118. Tsukada, K., H. Minamitani, E. Sekizuka, and C. Oshio, Image correlation method for measuring blood flow velocity in microcirculation: correlation 'window' simulation and in vivo image analysis. *Physiological measurement*, 21(4): 459-71, 2000.

119. Vaughn, M.W., L. Kuo, and J.C. Liao, Effective diffusion distance of nitric oxide in the microcirculation. *The American journal of physiology*, 274(5 Pt 2): H1705-14, 1998.

120. Walburn, F.J. and D.J. Schneck, A constitutive equation for whole human blood. *Biorheology*, 13(3): 201-10, 1976.

121. Williams, D.A. and S.S. Segal, Feed artery role in blood flow control to rat hindlimb skeletal muscles. *The Journal of physiology*, 463: 631-46, 1993.

122. Yalcin, O., P. Ulker, U. Yavuzer, H.J. Meiselman, and O.K. Baskurt, Nitric oxide generation by endothelial cells exposed to shear stress in glass tubes perfused with red blood cell suspensions: role of aggregation. *American journal of physiology. Heart and circulatory physiology*, 294(5): H2098-105, 2008.

123. Zhang, J., P.C. Johnson, and A.S. Popel, Effects of erythrocyte deformability and aggregation on the cell free layer and apparent viscosity of microscopic blood flows. *Microvascular research*, 77(3): 265-72, 2009.

124. Zweifach, B.W., S. Kovalcheck, F. De Lano, and P. Chen, Micropressure-flow relationships in a skeletal muscle of spontaneously hypertensive rats. *Hypertension*, 3(5): 601-14, 1981.

APPENDICES

Appendix A: Surgical preparation for in vivo study

The detailed procedure of the surgical preparation for rat *in vivo* study is described below and illustrated in Figure A-1. An open cremaster muscle preparation is referred to a report by Baez [4]. In addition, the feeding blood vessels of the cremaster muscle in the rat is referred to a report by Meininger *et al*. [72].

- Pentobarbital sodium (50 mg/kg ip) is used to anesthetize the rat. When an adequate level of anesthesia is attained as determined from lack of motor response to tail and toe pinch, the animal is placed on a rubber heating pad circulated with warm water
- The body temperature of the animal is maintained at 37℃ during surgery. While the jugular vein is catheterized for infusion of additional anesthetic (10 mg/kg) or dextran solutions, the femoral artery is catheterized for blood pressure monitoring and for blood samples withdrawing. All catheters are heparinised with heparin 30 IU/ml saline solution to prevent blood clotting.
- A polyethylene tube is used to intubate the trachea. Fluid and muscus is aspirated from the airway with vacuum.
- The abdomen is opened with a mid-line incision and the abdominal aorta freed from surrounding tissue. An *in vivo* metrics 1.5-mm ID pneumatic cuff is placed around the abdominal aorta and tied in place. The abdominal incision is closed and sutured.
- The rat cremaster muscle is exposed through a skin incision and freed from surrounding tissue. Warm Plasma-Lyte A (Baxter) adjusted to ph 7.4 is

continuously applied to the surgically exposed muscle to keep it moist. Surrounding connective tissues are removed from the muscle while the nerves and blood vessels are kept intact. The muscle is cleaned, stretched and secured onto a Plexiglas platform whose temperature is maintained at 35℃ by a heating element attached beneath it.

- Finally the microcirculation in the muscle is visualized through an intravital microscopic system. After the experiment, the rat is euthanized.

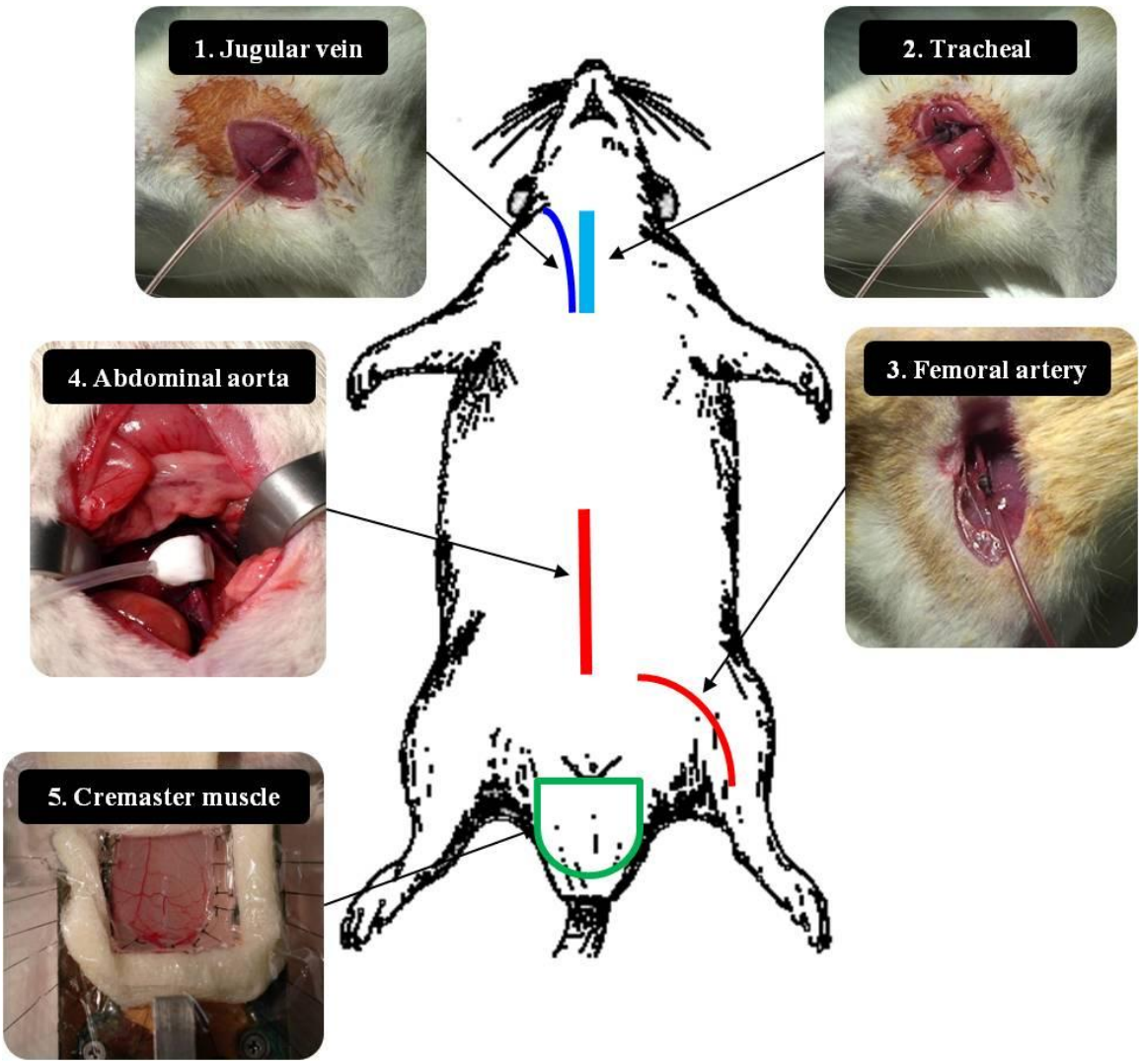

1. Jugular vein	Administration of additional anesthetic Administration of Dextran 500 solution
2. Tracheal	Ventilation
3. Femoral artery	Withdrawing blood sample Pressure monitoring
4. Abdominal aorta	Flow reduction
5. Cremaster muscle	Blood flow observation

Figure A-VI-1: Illustration of surgical preparation for *in vivo* study.

Appendix B: MATLAB code for histogram-based minimum algorithm in CHPTAER II

```
% CFL measurement based on minimum algorithm (histogram-based)

function CFLmeasurement()
close all
cDir = cd; %get current directory path
%*********************************************************************%
[Input field]
%*********************************************************************
LVW = xxx;   %x-position of left vessel wall
RVW = xxx;   %x-position of right vessel wall
lineY = xxx; %y-position of analysis line
totframe = xxxx; %total number of frames
pixelResolution = xxxx; %pixel resolution
%location of target images
Imdir = strcat(cDir,'\extracted_image_source');
%*********************************************************************

%*********************************************************************
%% step 1: Image reconstruction
%*********************************************************************
%total x-direction length of the analysis image
xDistance = RVW - LVW + 1;
ReconI = zeros(totframe,xDistance); %matrix allocation for image
h = waitbar(0,'In Progress...'); % give waitbar title
num2 = 1;
for framenum = 1:totframe
    str = strcat(Imdir,'\',num2str(framenum),'.bmp');
    I = imread(str,'bmp');
    I = medfilt2(I); %median filter
    I = im2single(I); %convert image into single
    num = 1;
    waitbar(framenum/totframe);
    for m = LVW:1:RVW
        ReconI (num2, num) = I (lineY, m);
        num = num + 1;
    end
    num2 = num2+1;
end
delete(h); %close waitbar

% save reconstructed image
filename = 'recon_image.bmp';
str = strcat(cDir,'\',filename);
imwrite(ReconI,str,'bmp');

%call step2 function for CFL obtainment
step2histogram(ReconI, pixelResolution, filename);
%*********************************************************************
% continues…
```

```
%*********************************************************************
% step 2: Image segmentation for CFL width measurement
% from reconstructed image based on minimum algorithm
%*********************************************************************
function step2histogram(I, pixelResolution, filename)
Isize = size(I); %image size
Current_filename = filename(1:end-4); %exclude ".bmp"
vesselDiameter = Isize(2)*pixelResolution;

center = round(Isize(2)/2);
IL = imcrop(I, [1, 1, center, Isize(1)]);
IR = imcrop(I, [center, 1, Isize(2), Isize(1)]);

IL = imadjust(IL); %contrast adjustment
IR = imadjust(IR);
LeftThreshold = minimumthresh(IL); %thresholding
RightThreshold = minimumthresh(IR);

LeftBinary = im2bw(IL,LeftThreshold); %binarizaion
RightBinary = im2bw(IR,RightThreshold);

% Save images
str = strcat(Current_filename,'_Left.bmp');
imwrite(IL, str,'bmp');
str = strcat(Current_filename,'_Right.bmp');
imwrite(IR, str,'bmp');
str = strcat(Current_filename,'_Left_Binary.bmp');
imwrite(LeftBinary, str,'bmp');
str = strcat(Current_filename,'_Right_Binary.bmp');
imwrite(RightBinary, str,'bmp');

% CFL count
Result(:,1)=countCFL(LeftBinary,1);
Result(:,2)=countCFL(RightBinary,2);
realResult = Result * pixelResolution; %real CFL
NrealResult = (realResult/(vesselDiameter/2))*100;
meanLCFL = mean(realResult(:,1));
meanRCFL = mean(realResult(:,2));
sdLCFL = std(realResult(:,1));
sdRCFL = std(realResult(:,2));

% Save data
str2 = strcat(Current_filename,'.txt');
save (str2, 'realResult', '-ascii','-tabs');

% Display
disp('************************************************');
disp(['Vessel diameter:',num2str(vesselDiameter),'um']);
disp(['Left CFL mean: ', num2str(meanLCFL),'um']);
disp(['Left CFL SD: ', num2str(sdLCFL),'um']);
disp(['Right CFL mean: ', num2str(meanRCFL),'um']);
disp(['Right CFL SD: ', num2str(sdRCFL),'um']);
disp('************************************************');

% Plot figures
```

```
endtime = 1/3000 * Isize(1);
time = linspace(0,endtime,Isize(1));
maxCFL = max(max(realResult));
yLimit = ceil(maxCFL)+2;

figure, subplot(2,1,1);
plot(time,realResult(:,1));
axis([0,endtime,0,yLimit]);
title('Left');
ylabel('Cell-free layer [um]');
hold on
plot(time,meanLCFL,'-c');
hold off
subplot(2,1,2);

plot(time,realResult(:,2),'r');
axis([0,endtime,0,yLimit]);
title('Right');
xlabel('Time [s]');
ylabel('Cell-free layer [um]');
hold on
plot(time,meanRCFL,'-c');
hold off

figure
subplot(1,2,1)
totframe = length(IL);
imshow(IL,'Border','tight');
hold on
scatter(Result(:,1),1:totframe,2,'o','b')
title('Left');
hold off

subplot(1,2,2)
right_end = size(IR);
imshow(IR,'Border','tight');
hold on
scatter(right_end(2)-Result(:,2),1:totframe,2,'o','r')
title('Right');

% Message box for the results
Message = {['Vessel diameter:',num2str(vesselDiameter),'um'],...
    ['Left CFL mean: ', num2str(meanLCFL),'um'],...
    ['Left CFL SD: ', num2str(sdLCFL),'um'],...
    ['Right CFL mean: ', num2str(meanRCFL),'um'],...
    ['Right CFL SD: ', num2str(sdRCFL),'um']};
msgbox(Message);
%**********************************************************************
% continues…
```

```
%************************************************************************
% Measuring CFL layer width
%************************************************************************
function vessel = countCFL(BW,n)
ImSize = size(BW);
totframe = ImSize(1);
vessel = zeros(totframe, 1);

if n == 2 %Right image
    BW = fliplr(BW); %flip right to left
end

%counting
for  framenum = 1:totframe
    m =1;
    pixcount = 0;
    while BW(framenum,m) == 1 && (m < ImSize(2))
        pixcount = pixcount + 1;
        m = m + 1;
    end
    vessel(framenum,1)= pixcount;
end
%************************************************************************

%************************************************************************
% Minimum thresholding algorithm
%************************************************************************
function T = minimumthresh(I,n)
if nargin == 1
    n = 255;
end
I = floor(I*255);
% Calculate the histogram.
y = hist(I(:),0:n);
% Smooth the histogram by iterative three point mean filtering.
iter = 0;
while ~bimodtest(y)
    h = ones(1,3)/3; %low pass filter
    y = conv2(y,h,'same'); %2D convolution
    iter = iter+1;
    % If the histogram turns out not to be bimodal, set T to zero.
    if iter > 10000;
        T = 0;
        return
    end
end
% The threshold is the minimum between the two peaks.
for k = 2:n
    if y(k-1) > y(k) && y(k+1) > y(k)
        T = k-1;
    end
end
T = T/255;

function b = bimodtest(y)
% Test if a histogram is bimodal.
```

```
% y: histogram
% b: true if histogram is bimodal, false otherwise
len = length(y);
b = false;
modes = 0;
% Count the number of modes of the histogram in a loop. If the number
% exceeds 2, return with boolean return value false.
for k = 2:len-1
    if y(k-1) < y(k) && y(k+1) < y(k)
        modes = modes+1;
        if modes > 2
            return
        end
    end
end
% The number of modes could be less than two here
if modes == 2
    b = true;
end
%**************************************************************************
% code ended
```

Appendix C: Typical CFL widths obtained from experiments in CHAPTER III

The following pages include raw data of CFL widths (μm) obtained under a **non-aggregating condition** for 1 s. The time interval between each measurement was 1/3000 s.

0.5	3.0	0.5	3.0	1.5	2.5	1.0	0.0	0.0	0.5	1.0	3.5
0.5	2.5	0.5	2.0	1.5	2.0	1.0	0.0	0.0	0.5	3.5	4.0
0.5	2.0	1.0	1.5	1.5	1.5	1.5	0.5	1.0	0.0	4.0	4.0
0.5	1.5	1.0	1.0	1.5	1.0	2.0	1.0	2.0	0.0	4.5	4.0
1.0	1.0	2.0	1.0	1.5	1.0	2.0	1.5	2.5	0.0	5.0	3.5
1.5	1.0	2.5	0.5	1.5	1.0	2.5	1.5	2.5	0.0	4.5	2.5
2.0	0.5	2.5	0.5	1.5	1.5	2.5	2.0	2.5	0.0	3.0	2.0
1.5	0.5	2.0	0.5	1.5	1.5	2.5	2.5	2.5	0.0	2.5	1.5
1.0	0.5	2.0	0.5	1.5	1.5	2.5	3.0	2.0	0.5	2.0	1.5
1.0	1.0	1.5	0.5	1.5	2.0	2.0	2.0	1.5	1.0	2.0	1.5
0.5	1.0	1.5	1.0	1.5	3.0	2.0	1.0	1.5	1.5	1.5	1.5
0.5	1.0	1.0	2.0	1.5	2.5	2.0	0.5	1.0	2.0	1.5	1.5
0.5	1.5	0.5	3.0	1.5	2.0	2.0	0.0	1.0	2.0	1.5	1.5
0.5	1.5	0.0	3.5	2.0	1.5	2.5	0.5	1.0	2.0	1.5	2.5
0.5	2.0	0.0	4.0	2.0	1.5	2.5	0.5	1.0	2.0	1.5	3.0
0.5	2.0	0.0	3.5	3.0	1.5	2.5	0.5	1.0	2.0	1.5	2.5
0.5	1.5	0.0	3.5	4.0	1.5	2.5	1.0	1.0	2.5	1.0	2.0
0.5	1.5	0.0	3.5	3.0	1.0	2.5	1.0	1.0	3.0	1.0	1.5
0.5	1.5	0.0	3.5	2.5	1.5	2.5	1.5	1.0	3.0	1.0	1.0
0.5	1.0	0.0	2.5	1.5	1.0	2.5	2.0	1.0	2.5	1.0	1.0
1.0	1.0	0.0	2.0	1.5	1.0	2.5	2.0	1.0	2.0	1.0	1.0
1.5	1.0	1.0	1.5	1.5	1.0	2.5	1.5	1.5	1.5	1.0	1.0
2.0	1.0	4.0	1.0	1.5	0.5	2.5	1.5	1.5	1.5	1.5	1.0
2.5	1.0	3.5	1.0	1.5	0.5	2.0	1.0	1.5	1.5	2.0	1.0
3.5	1.0	3.0	0.5	1.5	0.5	1.5	1.0	1.5	1.5	2.5	1.0
3.5	1.0	2.0	0.5	2.0	0.5	1.0	0.5	1.5	1.5	2.5	1.5
3.0	1.0	1.5	0.5	2.5	0.0	0.5	0.5	2.5	1.0	2.0	2.0
2.5	0.5	1.0	0.5	2.5	0.0	0.5	1.0	3.0	1.0	2.0	2.5
2.0	0.5	1.0	0.5	2.5	0.5	0.0	1.5	3.5	1.0	1.5	2.5
1.5	0.5	0.5	1.0	2.0	0.5	0.0	1.5	2.5	1.0	1.5	2.0
1.5	0.5	0.5	1.5	1.5	0.5	0.0	1.5	1.5	1.0	1.0	1.5
1.0	1.0	1.0	2.5	1.5	1.0	0.5	1.5	1.0	1.0	1.5	1.5
1.0	1.0	1.0	2.5	1.0	1.5	1.0	1.5	1.0	1.0	1.5	1.5
1.0	1.0	1.0	2.5	1.0	2.0	1.5	1.5	1.0	2.5	1.0	1.5
1.0	1.0	1.0	2.5	1.5	2.0	2.0	1.5	1.0	3.0	1.0	1.5
1.0	1.0	1.0	2.5	1.5	1.5	2.0	1.5	0.5	3.0	1.0	1.5
1.0	1.0	1.0	2.5	2.0	1.5	1.5	1.0	1.0	2.5	1.5	1.5
1.0	1.0	1.0	2.5	2.0	1.5	1.0	0.5	1.0	1.5	1.5	1.5
1.0	1.0	1.0	2.5	2.5	1.5	1.0	0.0	1.5	1.0	1.5	1.5
1.0	1.5	1.0	2.5	2.5	1.0	1.0	0.0	2.5	0.5	1.0	1.5
1.5	1.5	1.0	2.0	2.5	1.0	0.5	0.0	3.0	0.5	1.0	1.0
1.5	1.5	1.5	2.0	2.5	0.5	0.5	0.0	3.0	0.0	1.0	1.0
2.0	1.0	2.0	1.5	2.5	0.5	0.5	0.0	2.0	0.0	1.0	1.0
2.5	1.0	3.5	1.5	3.0	0.5	0.5	0.0	1.5	0.0	1.5	1.0
3.0	1.0	4.0	1.5	3.5	0.5	0.0	0.0	1.0	0.0	2.5	1.0
3.0	0.5	3.5	1.5	3.5	1.0	0.0	0.0	0.5	0.0	3.5	1.0

1.5	2.5	2.0	1.5	1.0	0.5	1.0	1.0	1.5	1.0	0.5	2.0
2.0	2.0	2.0	1.5	1.0	0.0	2.0	1.0	1.0	1.0	0.0	2.0
2.0	1.0	2.0	1.0	1.0	0.0	2.5	1.0	1.0	0.5	0.0	2.0
1.5	0.5	2.0	1.5	0.5	0.5	2.5	1.0	1.0	0.5	0.0	2.0
1.5	1.0	2.5	1.0	0.5	0.5	2.5	1.0	1.0	0.5	0.0	1.5
1.0	1.0	3.0	1.0	1.0	0.5	2.5	0.5	1.0	0.5	0.0	1.5
1.0	1.0	3.0	1.0	1.0	0.5	3.0	0.5	1.5	0.5	0.0	1.0
0.5	1.0	2.5	1.0	1.0	0.5	3.5	0.5	1.5	0.5	0.0	1.0
0.5	1.5	2.0	0.5	1.5	0.0	4.0	0.5	2.0	0.5	0.0	1.0
0.5	2.5	1.5	0.5	2.0	0.0	4.0	0.5	1.5	1.0	1.0	1.0
0.0	2.5	1.0	0.5	3.5	0.0	3.5	1.0	1.5	1.5	2.5	0.5
0.5	1.5	1.0	0.5	5.0	0.5	3.0	1.5	1.5	3.0	3.0	0.5
0.5	1.5	0.5	1.0	5.0	1.5	2.5	2.5	1.5	3.5	3.0	0.5
0.5	1.0	0.5	1.5	5.0	1.5	2.0	2.0	1.5	3.5	3.5	0.5
1.0	1.0	0.5	1.5	4.5	1.0	1.5	1.5	2.0	3.5	3.5	1.0
1.0	1.0	0.5	1.5	3.5	1.0	1.0	1.5	2.0	3.5	3.0	1.0
1.0	1.0	0.5	1.5	3.5	1.0	1.0	1.0	2.0	3.5	2.5	1.5
0.5	1.0	0.5	1.5	3.0	1.0	1.0	1.0	2.0	3.0	2.5	2.0
0.5	1.0	0.5	1.5	3.0	1.0	1.0	0.5	2.0	2.5	2.0	2.0
0.5	1.0	0.5	1.5	3.0	1.0	1.0	0.5	2.0	2.0	1.5	1.5
0.5	1.5	0.5	2.0	3.0	1.0	1.5	1.0	1.5	1.5	1.0	1.5
0.5	1.5	1.5	1.5	3.0	1.5	2.0	1.5	1.5	1.5	1.0	1.0
0.0	1.5	1.0	1.5	3.5	3.0	3.0	2.0	1.5	1.5	1.0	1.0
0.0	1.5	1.0	1.0	3.5	4.0	4.0	2.0	1.5	1.0	1.0	1.0
0.5	1.5	1.0	1.0	4.0	5.0	4.5	1.5	1.5	0.5	1.0	1.0
1.0	1.5	1.0	0.5	3.5	4.5	3.5	1.5	1.5	0.5	1.0	0.5
2.0	1.5	1.0	0.5	3.0	2.0	3.0	1.0	1.5	0.5	1.0	1.0
2.5	1.5	1.5	0.0	2.0	1.0	2.5	1.0	1.5	0.5	0.5	1.0
2.5	1.0	2.0	0.0	1.5	1.0	2.0	1.0	1.5	0.5	0.5	1.0
2.5	1.0	3.0	0.0	1.0	0.5	1.5	1.0	1.5	0.5	0.5	2.0
2.0	1.0	4.5	0.0	0.5	0.5	1.0	1.5	1.0	1.0	1.0	2.0
2.0	1.5	4.0	0.5	0.0	0.5	1.0	2.0	0.5	1.0	1.0	2.0
1.5	1.0	3.0	0.5	0.0	0.5	1.0	3.5	0.5	1.5	1.0	1.5
1.5	1.0	2.0	0.5	0.0	1.0	0.5	3.5	0.5	1.5	1.0	1.5
1.5	0.5	1.5	1.0	0.0	1.5	0.5	3.0	0.5	1.0	1.0	1.5
2.0	0.5	1.0	1.0	0.0	2.0	0.5	2.0	0.5	1.0	1.0	1.5
2.0	1.0	1.0	1.0	0.0	2.0	0.5	1.5	1.0	1.0	1.0	1.5
2.5	1.0	1.0	1.0	0.0	2.0	0.5	1.5	1.5	1.0	1.5	2.0
3.0	1.0	1.0	1.0	0.0	2.0	0.5	1.0	2.5	0.5	2.5	2.0
4.0	1.0	0.5	1.0	0.0	1.5	1.0	1.0	3.0	1.0	2.0	2.0
5.5	0.5	0.5	1.5	0.5	1.0	1.0	1.0	3.0	1.0	2.0	2.0
5.5	0.5	0.5	1.5	0.5	1.0	1.0	1.5	3.0	1.5	2.0	2.0
5.5	1.0	0.5	1.5	0.5	0.5	1.0	1.5	3.0	2.0	1.5	1.5
5.5	1.5	1.0	1.5	0.5	0.5	1.0	2.0	3.0	2.0	1.5	2.0
5.5	2.0	1.5	1.5	0.5	0.5	1.0	2.0	2.0	1.5	1.5	2.0
5.5	2.0	1.5	1.5	0.5	0.5	1.0	1.5	1.5	0.5	1.5	1.5

2.0	0.0	4.0	3.5	0.0	2.0	4.5	5.5	1.0	3.0	2.5	0.5
2.0	0.0	3.5	3.0	0.5	1.5	4.5	6.0	1.0	3.0	3.0	0.5
2.5	0.0	3.0	2.0	0.0	1.0	4.0	6.0	1.0	3.0	2.5	0.5
2.5	0.0	3.0	1.5	0.0	0.5	3.5	6.0	1.0	3.0	2.0	1.0
3.0	0.0	2.5	1.5	0.0	0.5	3.0	6.0	1.0	3.0	1.5	1.0
3.0	0.0	2.0	1.0	0.5	0.0	3.0	6.0	1.0	3.5	1.0	1.5
2.5	0.0	1.5	1.0	0.5	0.0	3.0	5.5	1.0	4.0	1.0	1.5
2.0	0.5	1.0	1.0	1.5	0.0	2.5	5.0	1.0	4.5	0.5	1.5
2.0	1.5	1.0	1.0	3.5	0.0	3.0	5.0	1.0	4.5	0.5	1.0
2.5	1.5	0.5	1.0	3.0	0.5	3.0	4.5	1.0	1.0	0.5	1.0
2.5	1.0	0.5	1.0	2.0	1.0	3.0	4.5	0.5	0.5	0.5	1.0
3.0	1.0	0.5	1.0	1.5	2.0	3.5	4.0	0.5	0.0	1.0	1.5
2.5	0.5	0.5	1.0	1.5	2.0	4.5	2.5	1.0	0.0	1.5	2.5
1.5	0.5	0.5	1.0	1.5	1.5	4.5	1.5	1.0	0.0	2.0	3.0
1.5	0.5	0.5	1.0	1.0	1.5	4.0	1.0	1.5	0.0	2.5	3.0
1.0	1.0	1.0	1.5	1.0	1.5	3.5	0.5	2.0	0.0	2.0	3.0
1.0	1.5	1.0	1.5	1.0	1.5	3.5	0.0	2.5	0.0	1.5	3.0
1.0	2.5	1.0	1.0	1.0	2.0	2.5	0.0	2.5	0.0	1.0	3.0
0.5	3.0	1.0	0.5	1.5	2.0	1.5	0.0	3.5	0.0	0.5	3.0
0.5	2.5	1.0	0.0	2.0	2.5	1.0	0.0	4.0	1.0	0.5	2.5
0.5	2.0	1.0	0.0	2.5	2.5	1.0	0.0	4.0	1.5	0.5	1.5
0.5	1.5	1.5	0.0	3.0	3.0	0.5	0.5	3.5	2.0	0.5	1.0
1.0	1.0	2.0	0.0	2.5	3.0	0.5	1.5	2.5	1.5	0.5	0.5
1.0	0.5	3.0	0.0	1.5	2.5	0.5	1.5	1.5	1.5	0.5	0.5
1.5	0.5	3.0	0.0	1.0	2.5	0.5	1.0	1.0	1.5	1.0	0.5
1.5	0.5	3.0	0.0	0.5	2.0	0.0	0.5	0.5	1.5	1.0	0.5
1.0	0.5	3.0	0.0	0.5	2.0	0.5	0.5	0.5	1.5	1.0	0.0
1.0	0.5	3.0	0.0	0.5	2.0	0.5	0.0	0.0	1.5	0.5	0.0
1.0	1.0	3.0	0.5	0.0	2.0	1.0	0.5	0.0	1.5	0.5	0.0
1.0	2.0	3.0	1.5	0.0	2.5	1.5	1.0	0.0	1.0	0.5	0.0
1.0	2.5	3.0	2.0	0.5	2.5	2.0	1.5	0.0	1.0	0.5	0.0
1.0	3.0	2.0	2.5	0.5	2.5	2.0	1.5	0.0	0.5	0.5	0.0
1.5	2.5	1.0	3.0	1.5	2.5	2.0	1.0	0.0	0.0	0.5	0.5
1.5	2.5	0.5	3.5	2.0	1.5	2.0	1.0	0.0	0.0	0.0	0.5
1.5	2.0	0.0	4.5	3.0	1.0	2.0	1.0	0.0	0.0	0.5	0.0
2.0	1.5	0.0	5.0	3.0	0.5	2.0	2.0	0.5	0.0	0.0	0.0
2.0	1.5	0.0	4.5	3.5	0.0	2.0	5.0	1.0	0.0	0.5	0.0
2.0	1.5	0.0	4.5	4.0	0.0	1.5	4.5	1.0	0.0	0.5	0.0
2.0	1.5	0.0	4.5	3.0	0.0	1.5	2.5	0.5	0.0	1.0	0.0
2.0	1.5	0.0	2.0	2.5	0.0	1.5	2.0	0.5	0.0	1.0	0.5
1.5	1.5	0.0	1.0	2.0	0.0	1.5	1.5	0.5	0.0	1.0	1.0
1.0	2.0	0.0	0.5	1.5	0.0	2.0	1.5	0.5	0.5	1.0	2.0
1.0	2.5	1.0	0.5	1.5	1.0	3.0	1.0	1.0	0.5	1.0	3.0
1.0	3.0	2.0	0.0	1.5	1.5	3.5	1.0	1.0	0.5	0.5	3.0
0.5	4.0	2.5	0.0	1.5	4.5	4.5	1.0	1.5	1.0	0.5	3.0
0.0	4.0	3.5	0.0	2.0	4.5	5.0	1.0	2.5	2.0	0.5	3.0

3.5	0.5	2.5	1.0	0.0	1.0	1.5	0.5	3.0	1.0	0.5	4.0
3.5	0.5	2.5	1.0	0.0	1.0	1.5	1.0	3.5	1.5	0.5	5.0
3.5	1.0	2.0	1.0	0.0	1.0	1.0	1.5	3.5	2.0	0.5	5.0
3.5	1.0	1.5	1.0	0.0	1.0	1.0	1.5	3.5	2.0	0.5	2.0
3.5	2.0	1.5	1.5	0.0	0.5	1.0	2.0	3.5	1.5	0.0	1.5
2.5	3.5	1.5	1.0	0.0	1.0	1.0	2.5	3.0	1.0	0.0	1.0
1.5	3.5	1.0	1.0	0.0	1.0	1.0	2.0	2.5	1.0	0.0	1.0
1.0	3.5	1.5	0.5	0.0	1.0	1.5	1.5	2.5	1.0	0.0	1.0
0.5	3.5	1.0	0.5	1.0	1.0	1.5	1.5	2.0	0.5	0.5	0.5
0.0	3.5	1.0	0.5	1.0	0.5	1.5	1.5	2.0	0.5	0.5	0.5
0.0	3.0	1.0	0.5	1.5	0.5	2.0	1.5	2.5	1.0	1.0	0.5
0.0	2.5	1.5	0.0	2.0	0.5	2.5	1.5	2.5	1.0	1.5	0.5
0.0	2.5	2.5	0.5	3.0	0.0	2.0	1.5	2.5	1.5	1.5	1.0
0.0	2.5	2.5	0.5	3.0	0.0	2.0	1.5	2.5	2.5	2.0	1.5
0.0	2.5	2.5	0.5	3.0	0.0	1.5	1.5	2.0	2.5	2.0	2.5
0.0	2.5	2.0	0.5	2.5	0.0	1.5	1.0	1.5	1.5	2.0	3.5
0.5	2.5	1.0	1.0	2.5	0.5	1.5	1.0	1.0	1.0	2.0	4.0
1.5	2.0	1.0	1.0	2.5	1.0	1.5	0.5	1.0	0.5	2.0	4.0
2.5	1.5	0.5	1.5	2.0	1.0	1.5	0.5	1.0	0.0	2.0	3.5
2.5	1.0	0.5	2.0	2.0	1.0	1.5	0.0	1.0	0.0	2.0	2.5
2.5	1.0	0.5	2.0	2.0	1.0	1.0	0.0	1.0	0.0	2.0	2.5
2.0	1.0	0.5	2.0	2.5	1.0	1.0	0.0	1.0	0.0	2.5	2.0
2.0	1.0	1.0	1.5	2.5	1.0	0.5	0.0	1.0	0.0	2.5	2.0
1.5	1.0	1.0	1.5	2.5	1.0	0.5	1.0	1.0	0.5	2.5	1.5
1.5	1.0	1.5	1.5	2.0	1.0	1.0	1.5	1.0	0.5	2.0	2.0
1.5	1.5	1.5	1.5	2.5	1.0	1.5	2.5	1.0	0.5	1.5	2.0
1.5	1.5	2.0	2.0	2.5	1.0	2.0	3.0	3.5	0.5	1.0	1.5
1.5	1.5	2.5	2.0	3.0	1.0	2.0	3.5	3.5	0.5	0.5	1.0
1.5	1.5	2.0	2.0	3.0	1.0	3.0	4.0	3.5	1.0	0.0	0.5
1.5	1.5	1.0	1.5	2.5	1.0	3.5	4.0	3.5	1.0	0.0	0.0
1.5	2.5	0.5	1.5	2.0	1.0	4.0	3.0	3.5	0.5	0.0	0.0
1.5	3.0	0.0	1.5	1.5	1.5	4.0	2.0	2.5	0.5	0.0	0.0
2.0	2.5	0.0	1.0	1.5	1.5	3.5	1.5	2.5	0.5	0.0	0.0
2.5	2.5	0.0	1.0	1.5	2.0	3.0	1.0	2.0	0.5	0.0	0.0
2.5	2.5	0.0	1.0	1.5	2.5	2.5	0.5	2.0	0.5	0.0	0.0
2.0	2.0	0.0	1.0	1.0	3.5	2.0	0.5	2.0	0.5	0.0	0.5
2.0	2.0	0.0	1.0	1.0	4.0	1.5	0.5	1.5	1.0	0.0	1.0
1.5	2.0	0.0	1.0	1.5	4.0	1.5	0.5	1.5	1.5	0.5	1.0
1.5	2.5	0.0	1.5	1.5	4.5	1.0	0.5	1.0	2.0	1.0	1.0
1.0	3.0	0.5	2.5	1.5	4.0	1.0	1.0	1.0	2.5	1.0	1.0
1.0	3.0	1.5	3.0	1.5	3.0	1.0	2.0	0.5	2.5	1.5	1.0
1.0	3.0	3.0	3.0	1.0	2.0	1.0	3.0	0.5	2.0	2.0	1.0
1.0	2.5	2.5	1.5	1.0	1.5	1.0	2.5	0.5	1.5	2.5	1.0
1.0	2.5	2.0	0.5	1.0	1.5	1.0	2.5	0.5	1.0	3.0	1.5
1.0	2.5	1.0	0.5	1.0	1.5	0.5	2.5	0.5	1.0	3.5	1.5
0.5	2.5	1.0	0.0	0.5	1.5	0.5	2.5	0.5	0.5	3.5	2.0

2.0	1.0	2.5	0.5	1.5	1.0	3.0	0.5	2.0	2.5	1.5	0.5
2.5	1.0	2.5	0.5	1.5	1.0	2.5	0.0	2.0	3.0	1.0	0.5
3.0	1.0	2.5	0.5	1.5	1.5	2.5	0.0	2.0	3.5	1.0	0.0
3.0	1.5	3.0	0.5	1.0	2.0	2.5	0.0	2.0	3.5	1.0	0.5
2.5	1.5	3.0	0.5	1.0	2.5	2.0	0.0	2.0	3.5	1.0	0.5
2.0	1.5	2.0	0.5	1.0	3.5	1.5	0.0	2.0	3.5	1.0	1.5
1.5	1.5	1.5	0.5	1.0	3.5	1.0	0.0	1.5	3.0	1.5	2.5
1.0	1.5	1.0	1.0	1.0	3.0	1.0	0.0	1.5	2.5	2.0	3.0
1.0	1.5	0.5	1.0	1.5	2.5	0.5	1.0	2.0	2.0	2.0	3.5
1.0	1.0	0.5	0.5	2.0	2.0	0.5	1.0	1.5	1.5	1.5	4.0
1.0	1.0	0.0	0.5	2.5	1.5	0.5	1.5	1.5	1.0	1.5	4.5
1.0	1.0	0.0	1.0	2.5	1.5	0.5	2.0	1.5	1.0	1.0	4.5
1.5	1.0	0.0	1.5	1.5	1.5	0.5	2.5	1.5	1.0	1.0	4.0
1.5	1.0	0.0	1.5	0.5	1.0	1.0	2.5	1.5	1.0	1.5	4.0
2.5	1.0	0.0	1.5	0.0	1.0	1.0	3.0	1.5	1.5	1.5	3.0
3.0	1.0	0.0	1.5	0.0	1.5	1.0	2.5	1.5	1.5	2.0	2.0
3.0	1.5	0.0	1.0	0.0	1.5	1.5	2.0	1.5	1.5	3.0	1.5
3.0	1.5	0.5	1.0	0.0	1.5	1.5	1.5	1.5	1.5	3.5	1.0
3.0	2.0	1.0	1.5	0.0	1.5	1.5	1.0	1.0	2.0	3.5	1.0
3.5	2.0	2.0	1.5	0.0	1.5	1.5	1.0	1.0	2.0	4.0	1.0
4.0	2.0	2.5	2.0	0.0	1.5	1.5	1.0	1.5	2.0	4.0	1.0
4.0	2.0	2.5	2.0	0.5	1.5	1.5	1.0	1.5	2.0	3.0	1.0
4.0	2.0	2.5	1.5	1.5	1.5	1.5	0.5	2.0	2.0	2.0	1.0
4.0	2.0	2.5	1.0	2.5	1.5	1.5	1.0	2.0	2.0	1.5	1.0
3.5	2.5	2.0	0.5	2.5	1.5	1.5	1.0	1.0	2.5	1.0	1.0
3.0	2.5	2.0	0.5	2.0	1.5	1.5	1.0	1.0	3.0	0.5	1.0
2.5	2.5	1.5	0.0	2.0	1.5	1.5	1.0	0.5	3.5	0.5	1.0
2.0	2.5	1.0	0.0	2.5	1.0	1.5	1.5	0.5	4.0	0.5	1.0
1.5	2.0	1.0	0.0	2.5	1.5	1.5	1.5	0.0	4.0	0.5	0.5
1.0	2.0	1.0	0.0	1.5	1.5	1.5	1.0	0.0	4.0	0.5	0.5
1.0	2.0	1.0	0.0	1.0	1.5	1.0	1.0	0.0	4.0	0.5	0.5
0.5	2.0	1.0	0.0	1.0	2.0	0.5	1.0	0.0	4.5	1.0	1.0
0.5	2.0	1.5	0.5	1.0	1.5	0.5	1.0	0.0	4.0	1.5	1.0
0.5	1.5	2.0	0.5	1.0	1.0	0.5	0.5	0.0	2.0	1.5	1.5
0.5	1.5	1.0	0.5	1.0	0.5	0.5	1.0	0.0	1.5	1.5	1.5
0.5	1.0	1.0	0.5	2.0	0.5	0.5	1.0	1.5	1.0	1.5	1.5
0.5	1.0	0.5	0.5	3.0	0.5	1.0	2.0	3.5	1.0	2.0	1.0
0.5	0.5	0.5	0.5	3.0	0.5	1.5	3.5	3.0	1.0	2.0	1.0
0.5	0.5	0.5	1.0	2.5	0.5	2.0	3.5	2.0	1.0	3.0	1.0
1.0	0.5	0.5	1.0	2.0	0.5	2.0	3.0	1.5	1.0	6.0	1.0
1.5	0.5	0.5	1.0	1.5	0.5	2.0	3.5	1.5	1.5	2.5	1.0
1.5	0.5	1.0	1.0	1.5	1.0	2.0	3.0	1.5	1.5	1.0	1.0
1.0	1.0	1.0	0.5	1.5	1.0	2.5	3.0	1.5	1.5	0.5	1.0
1.0	1.5	0.5	1.0	1.0	3.0	2.5	3.0	1.5	1.5	0.5	1.0
1.0	2.0	0.5	1.0	1.0	4.0	1.5	2.5	2.0	2.0	0.5	1.0
0.5	2.5	0.5	1.5	1.0	3.5	1.0	2.5	2.0	2.0	0.5	0.5

0.5	1.0	0.0	5.0	0.0	0.0
0.5	1.0	0.0	4.0	0.0	0.0
0.5	1.0	0.0	3.0	0.0	0.0
0.0	1.5	0.0	1.5	0.0	0.0
0.0	2.0	0.5	1.0	0.0	0.5
0.5	2.5	1.0	1.0	0.0	0.5
1.0	3.0	1.0	0.5	0.5	0.5
2.5	3.0	1.0	0.0	1.0	1.0
3.5	2.5	0.0	0.0	2.5	4.5
3.5	2.0	0.0	0.0	3.0	4.5
3.0	1.0	0.0	0.0	3.0	
3.0	1.0	0.0	0.0	3.0	
3.0	0.5	0.0	0.5	2.5	
3.0	0.5	0.0	1.0	2.5	
2.5	0.5	0.0	1.5	2.5	
2.5	0.5	0.0	1.5	2.5	
2.5	0.5	0.0	2.5	2.5	
2.5	0.5	0.0	7.0	2.0	
2.5	1.5	0.5	7.0	1.5	
2.5	4.0	0.5	6.5	1.0	
2.5	4.0	0.5	2.0	0.5	
2.0	3.5	0.5	1.5	0.5	
2.0	3.0	0.5	1.5	0.5	
2.0	2.5	0.5	1.0	0.0	
1.5	2.5	1.0	1.0	0.0	
2.0	2.5	1.0	1.0	0.5	
1.5	2.5	1.0	1.0	1.5	
1.5	2.5	1.0	1.0	2.5	
1.0	2.5	0.5	1.5	2.5	
1.0	1.5	0.5	2.0	2.0	
0.5	1.0	0.5	2.0	1.5	
0.5	1.0	1.0	2.5	1.5	
0.5	1.0	1.0	3.0	1.0	
0.5	1.0	1.5	3.0	1.0	
0.5	1.5	1.5	3.0	1.0	
1.0	2.0	1.5	2.5	1.0	
1.0	2.5	1.5	1.5	1.0	
1.0	2.5	1.5	1.5	1.0	
2.0	2.5	2.0	1.0	1.0	
3.5	2.0	3.0	1.0	1.5	
4.0	2.0	4.0	0.5	2.0	
3.0	1.5	5.0	0.5	1.5	
2.0	1.0	5.0	0.0	1.0	
1.5	0.5	6.0	0.0	0.5	
1.5	0.0	5.5	0.0	0.0	
1.0	0.0	5.5	0.0	0.0	

The following pages include raw data of CFL widths (μm) obtained under a **normal-aggregating condition** for 1 s. The time interval between each measurement was 1/3000 s.

0.5	2.5	1.0	3.5	2.0	1.0	1.5	2.0	3.0	1.0	2.5	3.5
0.5	2.0	1.0	1.5	2.0	1.0	1.0	1.5	2.5	1.0	2.0	3.5
0.0	1.5	1.0	0.5	2.5	1.5	1.0	1.5	2.5	1.0	2.0	3.5
0.0	1.0	1.5	0.0	2.5	1.5	1.0	1.0	2.5	1.0	1.5	3.0
0.0	1.0	2.0	0.0	3.5	2.0	1.0	1.5	3.0	2.0	1.0	2.5
0.0	0.5	2.0	0.0	3.5	2.5	1.0	2.0	3.5	4.0	1.0	2.5
0.0	0.5	2.5	0.0	3.5	3.0	1.0	2.0	5.0	4.5	1.0	2.5
1.0	0.5	2.0	0.0	3.5	3.0	1.0	2.5	5.5	3.5	1.0	2.5
1.0	0.5	1.5	0.0	3.0	2.5	1.5	3.0	5.5	3.0	1.0	2.5
1.0	0.5	1.5	0.5	3.0	2.5	1.5	3.5	6.0	2.5	1.0	2.5
1.0	1.0	1.0	1.0	3.0	2.0	1.5	4.0	5.0	2.5	1.5	3.0
1.0	2.0	1.0	0.5	2.5	1.5	1.5	4.0	3.5	2.5	2.5	3.0
0.5	5.5	1.0	0.5	2.0	1.0	1.5	4.0	2.5	2.5	3.0	3.0
0.5	5.5	1.5	0.5	1.5	1.0	1.5	3.5	2.0	3.0	3.5	2.5
0.5	4.5	2.0	0.5	1.0	0.5	1.5	3.5	2.0	3.0	3.5	1.5
0.5	3.5	2.5	0.5	1.0	0.5	1.5	3.5	1.5	3.0	4.0	1.0
0.5	3.0	2.5	0.5	1.0	0.5	1.5	3.5	1.5	3.0	4.0	1.0
1.0	2.5	2.0	1.0	1.0	0.5	1.5	3.5	1.5	3.0	4.0	1.0
1.0	2.5	2.0	1.5	1.0	0.5	2.0	3.0	2.0	3.0	4.0	1.0
1.0	2.5	1.5	4.0	1.0	1.0	2.0	2.0	2.0	2.5	3.0	1.0
1.5	2.5	1.0	5.5	1.0	1.5	2.5	1.5	1.5	1.5	3.0	1.0
1.5	2.5	1.0	6.5	1.0	2.5	3.0	1.0	1.5	1.0	2.5	1.5
1.5	2.0	1.0	5.5	1.0	2.5	3.0	1.0	1.0	0.5	2.0	2.0
1.5	1.5	1.0	2.5	1.0	2.5	3.0	1.0	1.0	0.0	2.0	2.0
1.0	1.0	1.0	1.5	1.0	2.5	2.5	1.0	0.5	0.0	1.5	2.0
1.0	1.0	1.0	1.5	1.0	2.5	2.0	1.0	0.5	0.0	1.5	2.0
1.0	1.0	1.0	1.0	1.0	2.5	1.5	1.0	0.5	0.0	2.0	2.5
1.0	1.0	1.0	1.0	1.5	3.5	1.0	1.0	1.0	0.5	2.5	3.5
1.0	0.5	2.0	1.0	3.0	4.0	1.0	1.0	1.0	1.0	3.0	4.0
1.0	1.0	5.0	1.0	3.5	4.5	1.0	1.5	1.5	1.0	5.5	4.0
1.0	1.0	5.0	1.0	4.0	4.5	1.0	2.5	2.0	1.0	5.0	4.0
1.5	1.0	5.0	1.0	5.0	4.5	1.0	4.0	2.0	0.5	4.0	4.0
1.5	1.5	4.5	1.5	5.5	4.0	1.5	4.0	2.0	0.5	3.5	4.0
1.0	2.0	3.5	2.0	6.5	3.5	2.0	3.0	2.0	0.5	3.0	3.0
1.0	3.0	2.5	2.0	6.5	2.5	2.5	2.0	1.5	0.5	2.5	2.0
0.5	3.0	2.0	2.0	2.0	1.5	2.5	1.5	1.0	0.0	2.0	2.0
0.5	3.0	1.5	2.0	1.5	1.0	2.0	1.0	1.0	0.5	1.0	2.0
0.5	3.5	1.5	1.5	1.0	1.0	2.0	1.0	1.0	0.5	1.0	2.0
0.5	3.5	1.5	1.5	1.0	0.5	1.5	1.0	1.0	1.0	1.0	2.0
0.5	3.5	2.0	1.5	1.0	0.5	1.5	0.5	1.5	1.5	1.0	2.0
1.0	3.5	2.0	1.5	0.5	0.5	1.5	1.0	1.5	2.0	1.0	2.0
1.0	3.0	3.0	2.0	1.0	1.0	1.5	1.5	2.0	2.5	1.0	2.0
1.5	2.5	3.5	2.0	1.0	1.5	1.5	4.0	2.0	2.5	1.0	1.5
2.0	2.0	4.0	2.5	1.0	2.0	1.5	4.5	1.5	2.5	2.0	1.5
2.5	1.5	4.5	2.5	1.0	2.0	2.0	3.5	1.0	2.5	3.0	1.5
2.5	1.0	4.5	2.5	1.0	2.0	2.0	3.0	1.0	2.5	3.5	1.0

1.0	1.0	4.5	1.0	1.5	1.0	1.0	1.5	3.0	1.5	3.0	0.5
1.5	1.0	4.5	1.0	2.5	1.0	1.5	1.0	3.0	1.0	3.5	0.5
1.5	1.0	4.5	1.0	5.5	1.0	2.0	0.0	2.5	1.0	4.0	1.0
1.5	1.0	4.5	1.0	5.5	1.0	3.0	0.0	1.5	1.0	4.5	1.0
1.5	1.0	5.0	1.0	5.5	1.5	3.0	0.0	1.0	1.0	4.5	1.0
2.0	1.0	5.5	1.0	4.0	2.0	2.0	0.0	1.0	1.0	4.0	1.5
2.0	1.0	6.0	1.0	3.0	2.5	1.0	0.0	0.5	1.5	2.5	4.0
3.0	1.0	6.0	1.0	2.5	3.0	1.0	0.0	0.0	1.5	1.5	4.0
3.5	1.0	2.0	1.0	2.0	3.0	0.5	0.0	0.0	1.0	1.0	3.5
3.5	1.0	1.5	1.5	2.0	2.5	0.0	1.0	0.0	1.0	0.5	3.0
3.5	1.0	1.5	1.5	2.5	2.0	0.5	3.5	0.5	0.5	0.5	2.5
3.0	1.0	1.0	1.0	3.0	1.5	0.5	3.5	1.5	0.5	0.5	2.5
2.5	1.0	1.0	1.0	3.5	1.0	0.5	3.5	2.5	0.5	0.5	2.5
2.0	1.5	1.0	1.0	3.5	1.0	1.5	3.5	2.5	0.5	0.5	2.0
2.0	5.5	1.0	1.0	3.5	1.0	3.0	3.5	2.5	0.5	0.5	2.0
1.5	5.0	1.0	1.5	3.0	1.0	3.5	3.0	2.0	0.5	0.5	2.0
1.5	4.0	1.0	1.5	3.0	1.5	4.0	2.5	1.5	0.5	1.0	2.0
1.0	3.5	1.0	1.5	3.0	2.5	4.0	2.0	1.0	1.0	1.5	2.0
1.0	2.5	1.0	1.5	2.5	3.0	3.5	2.0	1.0	1.5	2.5	2.0
1.0	2.0	1.0	1.0	2.5	2.5	3.5	1.5	1.0	5.5	3.0	2.0
1.0	1.5	2.0	1.0	3.0	2.0	3.0	1.0	1.5	6.5	3.0	1.0
1.5	1.5	3.0	1.0	3.0	1.5	3.0	1.0	1.5	7.0	3.0	1.0
2.0	1.0	3.0	0.5	3.0	1.5	2.0	1.0	2.5	5.0	3.0	0.5
2.5	1.0	3.0	0.5	3.0	1.5	1.0	1.0	3.0	4.0	3.0	0.5
2.5	1.0	2.5	1.0	2.5	1.5	0.5	1.5	3.5	2.5	3.0	0.0
2.0	1.0	2.0	1.0	2.5	1.5	0.5	1.5	3.5	2.0	3.0	0.0
1.5	1.0	1.5	1.5	2.5	1.5	0.0	1.5	2.5	1.5	2.5	0.0
1.5	1.0	1.5	1.5	2.0	1.5	0.0	1.5	2.0	1.5	1.5	0.0
1.0	1.5	1.0	1.5	2.0	1.5	0.0	1.5	1.5	1.5	1.0	0.0
0.5	1.5	0.5	2.0	2.0	2.0	0.5	2.0	1.0	1.5	1.0	0.0
0.5	1.5	0.5	3.0	2.0	2.0	1.0	2.0	1.0	1.5	0.5	0.0
0.0	2.0	0.5	3.5	2.0	2.5	3.0	2.0	0.5	1.5	0.5	0.0
0.0	2.0	0.5	3.5	2.5	4.5	4.0	1.5	0.5	1.5	0.5	0.5
0.0	2.5	1.0	3.5	3.0	6.5	4.0	1.5	0.5	1.0	0.0	1.0
0.5	3.0	1.5	3.5	3.0	6.0	4.0	1.5	1.0	1.0	0.5	2.5
1.0	3.0	2.0	2.5	2.5	5.0	4.0	1.5	1.0	1.0	0.5	3.5
2.0	2.5	1.5	1.5	2.0	4.5	3.0	1.5	1.5	1.0	1.0	4.0
2.5	2.5	1.0	1.5	1.5	3.5	2.0	1.5	1.5	1.0	2.0	4.5
2.5	2.0	0.5	1.0	1.0	2.0	1.0	1.5	1.5	2.0	3.0	6.0
2.5	2.0	0.5	1.0	1.0	1.5	1.0	1.5	2.0	3.0	3.0	7.0
2.5	2.0	0.5	1.0	0.5	1.5	0.5	1.5	2.0	4.0	2.5	7.0
2.0	2.0	0.5	0.5	0.5	1.0	0.5	1.5	2.0	3.5	2.0	6.0
1.5	2.0	0.5	0.5	1.0	1.0	0.5	2.0	2.0	3.5	1.5	5.0
1.5	2.5	0.5	1.0	1.0	1.0	1.0	2.0	1.5	3.0	1.0	4.5
1.0	3.0	1.0	1.0	1.0	1.0	1.5	2.5	1.5	3.0	1.0	4.0
1.0	4.0	1.0	1.0	1.0	1.0	1.5	3.0	1.5	3.0	1.0	3.5

3.5	0.5	1.5	2.0	1.0	1.0	2.5	1.5	3.5	1.5	1.0	0.0
3.0	0.5	1.0	2.0	1.0	1.5	3.0	1.5	2.5	1.5	1.0	0.0
3.0	0.5	1.0	2.0	1.5	1.0	3.0	1.5	1.5	1.5	1.0	0.0
2.5	0.5	1.0	2.0	2.0	1.0	2.5	1.5	0.5	2.0	1.0	0.0
2.0	1.0	1.0	2.0	2.0	1.0	2.0	1.5	0.5	2.5	1.0	0.0
2.0	1.5	1.0	2.0	2.5	1.0	2.0	1.5	0.5	4.0	1.0	0.5
1.5	3.0	1.0	2.0	2.5	1.0	1.5	1.5	0.5	5.0	1.0	1.0
1.5	4.0	1.0	1.5	2.5	0.5	1.0	2.0	0.5	5.0	1.0	2.0
1.0	4.5	1.5	1.0	2.5	1.0	1.5	2.5	0.5	5.0	1.5	2.0
1.5	4.5	1.0	1.0	2.0	0.5	1.5	3.0	1.0	5.0	1.5	2.0
1.5	4.0	1.0	0.5	1.0	1.0	1.5	3.0	1.5	5.0	1.5	2.0
1.5	4.0	1.0	0.5	1.0	1.0	2.0	3.0	2.0	5.0	1.5	2.5
2.0	4.5	1.0	0.5	0.5	1.5	2.5	2.0	2.0	4.0	1.5	3.0
2.5	5.0	1.5	0.5	0.5	4.0	3.5	1.5	2.5	2.5	1.0	2.5
3.0	5.0	1.5	1.0	0.5	4.5	4.0	1.0	2.5	1.5	1.0	1.5
2.5	4.0	2.5	1.0	1.0	5.0	3.5	1.0	2.0	1.0	1.0	1.0
2.0	3.0	2.5	1.5	2.0	5.0	2.5	0.5	2.0	1.0	1.0	0.5
1.5	3.0	2.5	1.5	3.0	3.5	1.5	0.5	2.0	0.5	1.5	0.5
1.5	2.5	2.5	1.0	3.0	2.5	1.0	0.5	1.5	1.0	2.0	0.0
2.5	2.5	2.0	0.5	3.5	2.0	1.0	0.5	1.5	1.0	3.0	0.0
3.5	3.0	2.0	0.5	3.5	1.5	0.5	1.0	1.5	2.0	3.5	0.0
4.0	3.0	2.0	0.0	3.5	1.0	0.5	1.5	1.5	2.5	3.5	0.0
4.0	3.0	2.0	0.0	3.5	1.0	0.5	1.5	2.0	3.0	3.5	0.0
3.0	2.5	2.0	0.0	3.0	1.0	0.5	1.0	2.0	3.0	3.0	0.5
2.5	1.5	2.0	0.0	3.0	1.0	0.5	1.0	2.0	2.5	3.0	1.5
2.0	1.0	2.0	0.0	3.0	1.0	1.0	1.0	1.5	2.0	3.0	4.0
1.5	1.0	1.5	0.5	3.0	1.0	1.5	1.0	1.5	2.0	3.0	4.5
1.5	1.0	1.5	1.0	2.5	1.5	2.0	1.0	1.0	1.5	3.0	5.0
1.5	1.0	1.0	3.0	2.5	2.0	2.0	2.0	1.0	1.5	3.0	5.0
1.5	1.0	1.0	4.5	2.5	4.5	2.0	2.5	1.0	1.5	2.5	4.5
1.5	1.0	1.0	4.5	2.5	6.0	1.5	3.5	1.5	1.5	1.5	3.5
2.0	1.0	1.0	4.0	2.0	6.0	1.5	3.0	2.5	1.5	1.5	2.5
2.0	1.0	1.0	4.0	2.0	6.5	1.5	1.5	6.0	1.0	1.0	1.5
2.5	1.5	1.5	2.5	1.5	7.5	1.0	1.0	6.5	1.0	1.0	1.0
2.5	2.5	1.5	1.5	1.5	7.5	1.0	1.0	6.5	1.0	1.0	0.5
2.0	3.0	2.0	1.0	1.5	6.5	1.0	1.0	6.5	1.0	1.0	0.5
1.5	2.5	3.0	1.0	1.5	5.0	1.0	1.0	6.0	1.0	1.0	0.5
1.5	2.0	3.5	0.5	1.5	4.5	1.0	1.0	3.5	1.0	2.0	0.0
1.5	1.5	3.5	0.5	2.0	4.5	1.5	1.0	2.5	1.5	4.5	0.0
1.5	1.5	3.5	0.5	2.5	4.0	1.5	1.0	2.0	2.0	5.0	0.0
2.0	1.5	4.0	0.5	2.5	3.5	1.5	1.0	1.5	2.5	5.5	0.0
2.0	1.5	4.0	1.0	2.0	3.5	1.5	1.0	1.5	2.5	5.5	0.0
1.5	2.0	4.0	1.0	2.0	2.5	1.0	1.0	1.0	2.5	2.0	0.0
1.0	2.0	3.5	1.5	1.5	2.5	1.0	1.5	1.0	2.0	1.0	0.0
1.0	2.0	3.0	1.5	1.5	2.5	1.0	2.0	1.0	1.5	0.5	0.5
0.5	2.0	2.5	1.0	1.5	2.5	1.0	3.0	1.0	1.5	0.0	1.0

1.0	4.5	2.0	3.5	4.0	2.5	0.5	5.5	0.5	1.5	2.5	2.0
1.0	4.5	2.5	3.0	4.0	2.5	0.5	4.5	0.5	1.5	3.5	2.0
1.0	3.5	3.0	2.5	4.0	1.5	0.5	2.5	1.5	1.0	6.5	2.0
1.5	2.0	2.5	1.5	4.0	1.5	1.0	2.0	2.0	1.5	3.5	2.0
1.5	1.0	1.5	1.5	4.5	1.0	1.0	1.5	1.5	1.5	2.0	2.0
1.5	0.5	1.0	1.0	4.5	1.0	1.0	1.0	1.5	1.5	1.5	2.0
1.5	0.0	1.0	1.0	4.5	1.0	1.5	1.0	1.0	1.5	1.0	2.0
1.5	0.0	0.5	1.0	3.5	1.5	1.0	1.0	1.0	1.5	1.0	1.5
1.5	0.5	0.5	1.5	2.5	2.5	1.5	1.0	1.0	2.0	1.0	1.5
1.5	1.0	0.5	1.5	2.0	5.0	1.0	1.0	1.0	3.0	0.5	1.0
1.5	1.5	0.5	2.0	1.5	5.5	1.0	1.5	1.0	3.5	0.5	1.0
2.0	1.5	0.0	2.0	1.5	5.5	1.5	2.0	0.5	4.0	0.5	1.0
2.5	1.0	0.0	1.5	1.5	5.0	4.5	2.0	0.5	4.0	0.5	1.0
3.5	1.0	0.5	1.0	1.5	3.5	3.5	1.5	0.5	3.5	1.0	1.5
3.5	1.0	0.5	1.0	1.5	2.5	3.0	1.0	0.5	3.0	2.0	2.0
4.0	1.0	1.0	0.5	1.5	2.0	3.0	1.0	0.5	2.0	3.0	4.5
4.0	1.0	1.0	0.5	1.5	2.0	3.0	1.0	0.0	1.0	3.0	5.0
4.0	1.5	1.0	0.5	1.5	1.5	2.5	1.0	0.0	1.0	3.0	5.5
3.5	2.0	1.0	0.5	2.0	1.5	2.5	1.0	0.5	1.0	2.5	5.5
3.0	2.5	1.0	0.5	2.0	1.5	2.0	1.0	0.5	1.0	2.5	5.0
2.5	2.5	1.0	0.5	1.5	1.5	2.0	1.5	1.0	1.0	2.5	4.0
2.5	3.0	2.0	1.5	1.5	2.0	2.0	2.0	1.5	1.0	2.5	3.5
2.5	3.0	2.0	3.5	1.0	2.0	2.0	2.0	2.0	1.5	2.0	2.0
2.0	2.5	2.5	3.5	1.0	2.0	1.5	1.5	3.0	2.5	2.0	1.0
2.0	1.5	2.0	3.5	1.0	1.5	1.5	1.5	4.0	3.5	2.0	1.0
2.0	1.0	2.0	3.5	1.0	1.5	2.0	1.0	5.0	4.5	2.0	0.5
2.0	1.0	1.5	3.5	1.5	1.0	2.0	1.0	5.0	5.0	1.5	0.5
2.0	0.5	1.0	3.5	2.0	0.5	2.0	1.0	5.5	5.0	1.5	0.5
2.0	0.5	1.0	3.0	2.5	0.5	2.0	1.0	5.5	4.5	1.0	0.5
1.5	0.5	1.0	2.5	3.0	0.5	1.5	1.0	6.0	3.5	1.0	0.5
1.5	0.5	1.0	2.5	3.5	0.5	1.5	1.5	5.0	2.5	0.5	0.5
1.5	0.5	1.0	2.0	3.5	0.5	1.5	1.5	2.0	1.5	0.0	0.5
1.5	0.5	1.0	2.0	3.5	0.5	2.0	2.5	1.5	1.0	0.0	1.5
2.0	1.0	1.5	2.0	4.0	0.5	2.5	5.0	1.0	1.0	0.0	1.5
2.5	1.0	1.5	2.0	5.0	1.0	3.0	5.0	1.0	0.5	0.0	1.5
2.5	2.5	1.5	2.0	5.5	1.5	3.5	4.0	1.0	0.5	0.0	1.0
2.5	3.0	1.5	2.5	5.0	2.0	3.0	3.5	1.0	1.0	0.0	0.5
2.0	3.0	1.5	3.0	4.5	2.5	2.0	2.5	1.0	1.0	0.5	0.0
2.0	3.0	1.5	3.0	3.5	2.5	1.0	2.0	1.0	1.5	1.0	0.0
2.0	2.5	1.0	2.5	2.5	2.5	0.5	1.5	1.5	2.0	7.0	0.0
2.0	2.0	1.0	2.5	2.0	2.5	0.0	1.0	1.5	2.0	5.5	0.5
2.0	1.5	1.0	3.0	2.0	2.5	0.0	1.0	2.0	2.0	4.5	1.0
2.0	1.5	1.0	3.5	1.5	2.0	0.0	1.0	2.0	2.0	4.0	2.0
2.0	1.5	1.5	4.0	1.5	1.5	0.0	0.5	2.0	2.0	3.5	2.5
3.0	1.5	2.5	4.0	2.0	1.0	0.5	0.5	2.0	2.0	3.0	2.5
4.0	1.5	3.5	4.0	2.5	1.0	1.5	0.5	1.5	2.0	2.5	2.5

2.5	5.5	2.5	0.0	1.5	1.5	0.5	1.0	3.0	2.5	2.5	4.0
2.5	5.5	2.5	0.0	1.5	2.0	1.0	0.5	2.5	3.0	2.0	4.5
2.5	5.0	2.5	0.0	1.5	2.5	1.0	0.5	2.0	3.5	1.5	5.0
3.0	4.5	2.0	0.0	1.5	5.0	1.5	1.0	1.5	4.0	1.5	4.5
3.0	3.5	1.0	0.5	1.5	5.5	2.5	1.0	1.5	3.5	1.0	3.0
3.5	3.0	1.0	1.0	1.5	5.5	2.5	2.0	1.0	2.5	1.0	2.5
4.5	3.0	0.5	1.5	1.5	6.0	2.0	3.5	1.5	2.5	1.0	2.0
4.0	2.5	0.5	2.0	1.5	6.0	1.5	3.5	1.5	2.0	0.5	1.5
2.0	2.5	0.5	2.0	2.0	6.0	1.0	3.5	2.0	1.5	0.5	1.5
1.5	2.5	0.5	2.0	2.0	5.0	0.5	3.5	3.0	1.5	1.0	1.5
1.0	2.5	1.0	2.0	1.5	4.0	0.5	3.5	3.5	1.0	1.0	1.5
0.5	3.5	1.5	2.0	1.5	3.0	0.5	3.0	3.5	1.0	1.5	1.5
0.0	4.0	2.0	2.0	1.5	2.5	0.5	2.5	3.5	1.0	1.0	1.5
0.0	5.5	2.0	1.5	1.5	2.0	1.0	2.0	3.0	1.0	1.0	1.5
0.0	5.0	2.0	1.5	1.0	2.0	1.5	2.0	2.5	1.0	1.0	1.5
0.0	3.5	2.0	1.5	1.0	1.5	2.0	1.5	3.0	1.0	2.0	1.5
0.5	2.5	2.0	1.5	1.5	1.5	2.0	1.5	3.5	1.5	2.5	2.0
1.0	2.0	2.0	1.5	1.5	1.5	2.0	1.5	4.0	2.0	2.5	2.0
1.0	1.5	2.0	1.0	2.5	1.5	2.0	1.0	4.0	3.0	2.0	2.5
1.0	1.5	2.5	1.0	3.0	1.5	1.5	1.0	4.0	5.0	1.5	3.0
1.0	1.5	2.5	1.0	3.5	1.5	1.5	1.0	4.0	5.0	1.5	4.5
1.0	1.5	2.5	0.5	3.0	2.0	1.5	1.0	4.0	2.5	1.5	4.5
1.5	2.0	2.0	0.5	2.5	2.5	1.0	1.0	3.5	1.5	1.5	5.0
2.0	2.0	2.0	0.5	2.0	3.5	1.5	0.5	3.5	1.0	1.5	5.0
2.5	2.5	1.5	0.5	1.5	4.0	2.0	0.5	3.0	1.0	2.5	5.0
2.0	4.0	1.5	0.5	1.5	3.5	2.5	0.5	3.0	1.0	3.5	4.5
2.0	5.0	1.5	1.0	1.0	3.0	2.5	0.0	3.0	1.0	4.0	3.5
1.5	4.5	1.5	1.5	1.0	2.5	2.5	0.5	3.0	1.0	4.0	2.0
1.5	3.5	1.0	2.0	1.5	1.5	2.0	0.5	2.5	2.0	4.5	1.0
1.0	2.5	1.0	2.5	1.5	1.0	1.5	1.0	1.5	2.0	5.0	1.0
1.0	2.0	0.5	3.0	1.5	1.0	1.5	5.0	1.0	2.0	5.5	0.5
1.5	2.0	0.5	3.0	2.0	1.0	1.0	5.0	1.0	2.0	7.0	0.5
1.5	1.5	0.5	3.0	2.0	0.5	1.0	4.0	0.5	2.0	6.0	0.0
1.0	1.5	0.5	3.0	2.5	1.0	0.5	2.5	0.5	1.5	4.5	0.5
1.0	1.0	0.5	2.5	2.5	1.0	0.5	2.0	0.0	2.0	3.5	0.5
1.0	1.0	0.5	2.0	2.5	1.0	0.5	1.5	0.0	2.0	3.5	1.0
0.5	1.0	1.0	1.5	2.0	1.5	0.5	1.0	0.0	2.0	3.5	1.5
0.5	0.5	1.5	1.0	1.5	2.0	0.5	1.0	0.0	2.0	3.5	2.5
0.5	0.5	2.5	1.0	1.0	1.5	1.0	0.5	0.5	1.5	3.5	4.0
0.5	0.5	10.5	1.0	1.0	1.0	0.5	0.5	1.0	1.5	3.5	5.0
0.5	0.5	2.5	1.0	1.0	1.0	1.0	0.5	2.5	1.5	3.5	5.0
1.5	0.5	1.5	1.0	1.0	0.5	1.0	0.5	3.0	1.5	3.0	5.0
2.5	0.5	1.0	1.0	1.0	0.5	1.0	0.5	3.0	1.5	3.0	4.5
3.5	1.0	1.0	1.0	1.0	0.5	1.5	1.0	2.5	2.0	3.0	3.5
5.0	1.5	0.5	1.0	1.0	0.5	1.5	1.5	2.5	2.5	3.0	3.5
5.0	2.0	0.0	1.0	1.0	0.5	1.0	2.5	2.5	2.5	3.5	3.0

3.0	3.0	1.0	2.5	3.0	1.5
3.0	3.0	0.0	2.0	2.0	2.0
3.0	3.0	0.0	1.5	1.5	2.5
3.5	3.5	0.0	1.5	1.0	3.0
4.0	3.5	0.0	1.0	1.0	5.5
4.5	3.5	0.0	1.0	1.0	6.0
4.0	3.0	0.5	1.0	1.0	6.5
3.0	3.0	1.0	1.0	1.0	6.5
2.5	2.5	3.5	1.0	1.0	6.5
2.5	2.0	4.5	1.0	1.0	6.0
2.0	1.5	3.5	1.0	1.0	
1.5	1.0	2.5	1.5	1.5	
1.5	1.0	2.0	2.0	2.5	
1.5	0.5	1.5	2.0	3.5	
1.5	0.5	1.5	2.5	4.5	
1.5	0.5	1.5	2.5	7.5	
2.0	0.5	1.5	2.0	5.5	
3.0	0.5	2.0	2.0	5.5	
3.0	1.0	2.5	1.5	5.0	
3.5	1.0	3.0	1.5	3.0	
3.0	1.0	2.5	1.5	1.0	
2.5	1.0	2.0	1.0	0.5	
1.5	1.0	1.5	1.0	0.0	
1.0	0.5	1.0	1.5	0.0	
0.5	0.5	1.0	1.5	0.0	
0.0	0.5	1.0	2.0	0.0	
0.0	0.5	1.0	2.5	0.0	
0.0	0.5	1.5	2.5	0.0	
0.0	1.5	2.0	2.0	0.0	
0.5	2.0	3.5	2.0	0.5	
1.0	3.0	4.0	1.5	1.0	
1.0	3.0	4.0	1.5	1.5	
1.0	3.0	3.5	1.0	1.5	
0.5	3.0	3.0	1.0	1.5	
0.5	3.5	2.5	0.5	2.0	
1.0	4.0	1.5	0.5	2.5	
1.0	4.5	1.0	0.5	3.0	
1.0	4.0	1.0	1.0	3.0	
1.5	4.5	0.5	1.0	2.5	
1.5	4.5	0.5	1.5	2.5	
2.0	5.0	0.5	1.5	2.5	
4.0	5.5	0.5	2.0	2.5	
4.0	6.0	1.0	2.0	2.0	
4.0	6.0	1.0	2.5	2.0	
3.5	5.5	2.5	3.0	1.5	
3.5	2.5	2.5	3.5	1.5	

The following pages include raw data of CFL widths (μm) obtained under a **hyper-aggregating condition** for 1 s. The time interval between each measurement was 1/3000 s.

1.0	1.0	2.0	0.0	1.5	1.5	1.5	2.5	1.5	2.0	4.0	3.0
1.0	1.0	2.5	0.5	1.0	1.5	1.5	3.0	1.0	2.0	3.5	2.5
1.5	1.5	3.0	3.0	1.0	1.5	2.0	4.0	1.0	2.0	3.5	2.5
2.0	4.5	3.5	4.0	1.0	1.5	2.5	6.0	0.5	2.0	3.0	2.0
2.0	5.0	3.5	3.5	1.0	1.5	2.5	5.5	0.5	2.0	3.0	2.0
1.5	4.5	3.0	3.0	0.5	2.0	3.0	4.5	0.0	2.5	2.5	1.5
1.5	4.0	2.0	3.0	0.5	2.5	4.0	4.5	0.5	2.5	2.5	1.5
1.0	4.0	1.5	3.0	1.0	3.0	4.5	4.5	0.5	3.0	2.5	2.0
1.0	3.5	1.0	3.0	3.5	3.5	4.5	5.0	1.0	4.0	2.5	2.0
1.0	3.5	1.0	3.0	4.5	3.5	4.5	5.0	2.0	5.5	2.5	2.0
1.0	3.5	1.0	3.5	5.0	3.5	4.5	4.5	2.5	6.0	2.5	2.0
1.0	3.5	1.0	4.0	5.5	3.5	4.5	3.0	2.0	5.5	2.5	1.5
1.0	4.0	0.5	4.0	5.0	4.0	4.0	2.0	2.0	4.5	2.0	1.5
1.0	4.5	0.5	4.0	4.0	4.0	3.0	1.0	1.5	4.0	1.5	1.5
1.5	4.5	1.0	4.0	4.0	3.5	2.0	1.0	1.5	3.5	1.5	1.5
1.5	3.0	1.5	3.0	3.5	2.5	2.0	1.0	2.0	3.0	1.5	1.5
1.5	2.5	2.0	2.5	3.5	2.0	1.5	0.5	1.5	3.0	2.0	2.0
1.5	2.0	2.5	2.0	3.5	1.5	1.5	0.5	1.5	3.0	2.5	4.5
2.0	1.5	2.5	1.5	4.0	1.0	1.5	0.5	1.5	2.5	3.5	5.0
5.5	1.5	3.0	1.5	4.0	1.0	2.0	0.5	1.0	2.5	4.0	4.5
5.0	1.0	3.5	1.5	4.5	0.5	2.5	0.5	1.0	2.5	4.0	3.5
4.5	1.0	4.5	1.5	4.0	0.5	1.5	1.0	1.0	2.0	3.5	2.5
3.5	1.0	3.5	2.0	3.0	1.0	1.5	1.0	1.5	1.5	2.5	2.0
2.5	1.5	3.0	2.5	2.5	1.0	1.0	1.5	2.0	1.5	2.0	2.0
2.5	2.5	2.5	2.5	1.5	1.5	1.0	4.5	2.0	1.0	1.5	1.5
2.0	3.0	2.0	2.5	1.5	2.0	1.0	4.0	2.0	1.0	1.5	1.5
1.5	2.5	2.0	3.5	1.0	3.0	1.0	4.0	1.5	1.0	1.5	1.0
1.5	2.5	2.0	4.0	1.0	3.5	1.0	4.0	1.5	1.0	1.5	1.0
1.5	3.0	2.0	5.0	1.0	3.5	1.0	3.5	1.0	1.0	1.5	1.0
1.0	3.5	1.5	5.0	1.0	3.5	1.0	3.5	1.0	1.0	1.5	1.0
1.0	3.5	1.0	5.0	1.5	3.0	1.0	4.0	1.0	1.5	1.5	1.0
1.0	2.5	1.0	4.5	1.5	2.5	1.0	4.0	1.0	2.0	2.0	1.0
1.0	2.0	1.0	4.5	1.5	1.5	1.0	3.0	1.0	2.5	2.0	1.5
1.0	1.5	1.0	4.0	1.5	1.5	1.0	2.0	1.0	3.0	2.0	1.5
1.5	1.5	1.5	4.0	1.0	1.0	1.5	1.5	1.0	3.5	3.0	2.0
1.5	1.5	2.0	3.5	1.0	1.0	1.5	1.5	1.5	3.5	4.0	2.5
2.5	1.5	3.0	3.5	1.0	1.0	1.5	1.5	1.5	3.5	3.0	3.0
2.5	1.5	3.0	3.5	1.0	1.0	1.0	1.0	1.5	4.0	2.5	3.0
2.5	2.5	2.0	3.5	1.5	1.0	0.5	1.0	2.0	3.5	2.5	3.0
2.0	3.0	1.5	3.5	2.0	1.0	0.5	1.0	3.5	3.5	2.0	3.0
1.5	3.0	1.0	3.0	2.0	1.0	0.0	1.0	3.0	3.0	2.5	2.5
1.0	2.5	0.5	2.5	2.0	1.5	0.0	1.0	2.5	3.0	3.0	2.5
1.0	2.0	0.5	2.0	2.0	2.0	0.5	1.5	1.5	3.0	3.5	2.5
1.0	2.0	0.0	2.0	2.0	2.0	1.0	4.5	2.0	3.0	4.0	2.5
1.0	1.5	0.0	1.5	1.5	2.0	2.0	3.5	1.5	3.5	4.0	2.5
1.0	1.5	0.0	1.5	1.5	2.0	2.5	2.5	2.0	4.5	3.5	2.5

3.0	2.5	2.0	2.0	3.0	1.5	1.0	2.5	2.0	2.0	2.5	1.0
3.5	2.0	1.5	2.0	2.5	2.0	1.5	2.0	2.0	1.5	2.0	1.0
4.5	1.5	1.5	2.5	2.0	2.5	1.5	2.0	2.5	1.5	2.0	1.0
4.5	1.5	1.5	2.5	1.5	2.5	2.0	2.0	2.5	1.5	2.0	2.0
4.0	1.5	1.0	3.0	1.5	2.5	2.0	1.5	2.0	1.5	2.0	3.0
3.5	2.0	1.0	3.0	1.5	2.5	2.0	1.5	2.0	1.5	2.5	3.0
3.0	2.0	1.0	3.0	1.0	3.0	1.5	2.0	2.0	2.0	3.0	2.5
2.5	2.0	1.5	4.0	1.5	2.5	1.5	2.0	2.0	2.0	4.0	2.5
2.5	1.5	2.0	5.0	1.5	2.0	1.5	2.0	1.5	2.0	4.5	2.5
2.5	1.5	3.5	6.0	2.0	2.0	1.5	2.0	1.5	2.0	4.5	2.5
3.0	1.5	4.0	6.5	2.0	1.5	1.5	1.5	1.5	2.0	4.0	2.5
3.0	1.5	4.0	7.0	2.5	1.5	2.0	1.5	1.5	2.0	4.0	2.5
2.5	1.5	4.0	7.0	3.0	1.5	3.5	1.0	1.5	2.5	3.5	2.5
2.5	1.5	4.0	6.5	3.0	1.5	4.0	1.0	1.5	3.0	3.0	2.5
2.5	1.5	4.0	6.0	3.0	1.5	4.0	1.5	1.5	3.0	2.5	2.5
2.5	2.5	3.5	5.0	2.5	1.5	4.0	2.0	2.0	3.0	2.5	2.5
2.5	3.0	3.0	4.0	2.5	2.5	4.0	2.5	3.0	3.0	2.0	2.5
2.0	3.0	2.5	3.0	2.5	4.0	4.0	3.5	4.0	3.0	2.0	2.0
2.0	2.5	2.0	2.5	3.0	4.5	4.5	4.0	4.5	3.0	2.0	2.0
2.0	2.0	2.0	2.0	3.5	5.0	4.0	4.0	4.5	2.5	2.0	2.0
2.0	2.0	2.0	2.0	3.5	5.5	3.5	4.0	4.5	1.5	2.0	2.0
2.0	1.5	2.0	2.0	3.0	5.5	2.5	3.5	4.0	1.0	2.0	1.5
1.5	1.5	2.0	2.0	2.5	5.5	2.0	3.5	2.5	0.5	2.5	2.0
1.5	1.5	1.5	2.0	2.0	5.0	1.5	3.5	1.5	0.0	3.0	2.0
1.5	1.5	1.5	2.0	2.0	5.0	1.5	3.5	1.5	0.0	3.5	2.0
2.0	1.5	1.5	2.0	1.5	4.5	1.5	4.0	1.0	0.0	3.0	2.0
2.5	1.0	1.5	2.0	1.5	4.5	1.0	4.5	1.0	0.0	3.0	2.0
2.5	1.5	1.0	2.5	1.5	4.5	1.0	3.5	1.0	0.0	3.5	2.5
2.5	1.5	1.0	2.5	1.5	4.0	1.0	2.5	1.0	0.0	4.0	3.0
3.0	1.5	1.0	2.0	1.5	3.0	1.5	2.5	1.0	0.5	4.0	2.5
3.0	1.5	1.0	2.0	2.0	3.0	1.5	2.0	1.0	1.5	4.0	2.0
2.5	1.5	1.0	2.0	2.0	3.0	2.0	2.0	1.0	1.0	3.5	1.5
2.5	1.5	1.5	2.0	2.5	2.5	2.5	2.0	1.0	1.0	3.5	1.5
2.5	1.0	7.0	1.5	2.0	2.5	2.0	2.0	1.0	0.5	3.5	1.5
2.5	1.5	6.0	1.5	2.0	2.5	2.0	2.0	1.0	0.5	3.0	1.5
2.5	1.5	5.0	1.5	2.0	2.5	1.5	2.5	1.5	0.5	3.0	1.5
2.0	1.5	4.0	2.0	1.5	3.0	1.5	3.0	2.0	0.5	3.0	1.5
2.0	1.5	3.0	2.0	2.0	3.5	1.5	3.5	3.0	1.0	3.0	1.5
2.0	2.0	2.5	1.5	2.0	4.0	1.5	3.0	5.5	1.5	2.5	1.5
2.0	5.0	2.5	1.5	2.0	4.0	2.0	3.0	5.5	1.5	2.5	1.5
1.5	5.0	2.0	2.0	2.5	3.0	2.5	2.5	5.0	1.5	2.5	1.5
1.5	4.5	2.0	2.5	3.0	2.5	3.0	2.0	4.0	1.0	2.0	1.5
1.5	4.0	2.0	2.5	2.5	2.0	3.5	2.0	3.0	1.0	1.5	1.5
1.5	3.5	1.5	3.5	2.5	1.5	3.0	2.0	2.5	1.5	1.0	1.5
2.0	3.0	1.5	4.0	2.0	1.5	2.5	1.5	2.5	2.0	1.0	2.0
2.5	2.5	1.5	4.0	2.0	1.5	2.5	1.5	2.0	2.5	1.0	2.0

2.5	1.0	2.5	1.0	2.5	4.0	5.0	1.5	2.5	2.0	1.5	2.5
3.0	1.0	3.0	1.0	2.5	3.0	4.5	1.5	2.0	1.5	1.5	3.0
3.0	1.5	2.5	1.5	2.0	2.5	4.0	1.0	2.0	1.0	1.5	3.0
3.0	2.0	2.0	2.0	2.5	2.0	3.0	1.0	2.0	1.0	1.5	2.5
3.0	2.5	1.5	2.5	2.5	2.0	2.5	1.0	2.0	1.0	1.5	2.0
2.5	2.5	1.0	2.5	2.5	1.5	2.0	1.0	2.5	1.0	1.5	1.5
2.0	2.5	0.5	3.0	3.0	1.5	1.5	1.5	2.5	1.0	1.5	1.5
1.5	3.0	0.5	3.5	2.0	1.5	1.5	2.0	2.0	1.5	1.5	1.0
1.5	3.0	0.0	4.0	1.5	1.0	1.0	2.5	1.5	2.0	2.0	1.0
1.0	2.5	0.0	3.5	1.0	1.5	1.0	2.5	1.5	2.0	2.0	1.0
1.0	2.0	0.0	2.5	1.0	1.5	1.0	3.0	1.0	1.5	2.5	1.0
1.0	1.5	0.5	2.0	1.0	2.0	1.0	3.0	1.0	1.5	2.5	1.0
1.0	1.0	1.5	1.5	0.5	2.0	1.5	2.5	1.0	1.0	2.0	1.5
1.0	1.0	2.5	1.5	0.5	2.0	2.0	2.0	1.0	1.0	1.5	1.5
1.0	1.0	3.0	1.5	0.5	2.5	2.5	1.5	1.0	1.0	1.5	2.0
1.0	1.0	3.0	1.5	0.0	3.0	2.5	1.5	1.5	1.0	1.5	2.5
1.5	1.5	3.5	1.0	0.5	3.0	2.0	1.5	2.0	1.0	1.5	2.5
1.5	1.5	3.5	1.0	1.0	3.5	1.5	1.0	2.0	1.5	1.0	3.0
1.0	1.5	4.0	1.0	3.0	4.5	1.5	1.0	2.0	2.0	1.0	2.0
1.0	1.5	4.5	1.0	4.0	5.0	1.5	1.5	2.0	3.5	1.5	1.5
1.0	1.5	4.5	1.0	5.0	5.0	1.5	1.5	2.0	5.0	1.5	1.5
1.5	2.0	4.5	1.5	5.0	5.5	1.0	2.5	2.0	5.0	1.5	1.0
2.5	2.5	4.5	2.0	4.0	6.5	1.0	3.0	2.0	4.0	2.0	1.0
5.5	2.5	4.5	2.5	3.0	7.0	1.0	3.5	1.5	2.5	2.0	1.0
4.0	2.5	2.5	3.0	2.5	5.5	1.0	3.5	1.0	2.0	2.0	1.0
3.0	2.5	1.5	3.0	2.5	4.5	1.0	4.0	1.0	1.5	2.0	1.5
2.0	2.5	1.0	2.5	2.0	4.5	1.0	4.0	1.0	1.0	2.0	2.0
2.0	3.0	0.5	2.5	2.0	4.0	1.0	3.0	1.0	1.0	2.5	2.0
1.5	3.0	0.5	2.5	2.0	4.5	1.0	2.0	1.0	1.0	2.5	2.0
1.5	3.0	0.5	3.0	2.5	4.5	1.0	1.5	1.5	0.5	3.0	2.0
2.0	3.0	0.0	3.0	2.5	4.0	1.0	1.5	1.5	0.5	3.0	2.0
2.0	2.5	0.0	2.5	2.5	3.0	1.5	1.5	1.5	0.0	2.5	2.0
2.5	2.5	0.5	2.5	2.5	2.5	2.0	1.0	1.5	0.5	2.0	2.5
3.0	2.0	0.0	2.0	2.0	2.5	2.5	1.0	1.0	1.0	1.5	3.5
3.5	2.0	0.0	2.0	2.0	2.5	2.0	1.0	1.0	2.0	1.5	3.5
3.0	2.0	0.0	2.0	2.0	2.5	2.0	1.0	0.5	4.0	1.5	2.5
2.5	2.5	0.0	2.0	2.0	2.5	1.5	1.5	0.5	3.5	1.5	2.0
2.5	2.5	0.5	1.5	2.5	2.5	1.5	1.5	1.0	3.0	1.5	1.5
2.5	2.5	1.0	1.5	3.5	3.5	1.0	2.0	1.5	2.5	1.5	1.5
2.0	3.0	1.5	1.0	4.0	4.0	1.0	2.0	1.0	2.5	1.5	1.0
2.0	3.0	1.5	1.0	4.5	4.0	1.5	2.0	1.5	2.5	1.5	1.0
1.5	3.0	1.0	1.0	4.5	4.0	1.5	2.0	1.5	2.5	1.5	1.0
1.5	2.5	1.0	1.5	4.5	4.0	2.0	2.0	2.0	2.5	1.5	0.5
1.0	2.5	1.0	1.5	5.5	4.0	2.0	2.0	2.5	2.5	1.5	0.5
1.0	2.5	1.0	2.0	5.5	4.0	1.5	2.0	3.5	2.0	1.5	0.0
1.0	2.5	1.0	2.0	5.0	4.5	1.5	2.0	5.0	2.0	2.0	0.5

1.0	0.5	1.0	4.5	2.5	1.5	3.0	3.0	2.5	1.0	3.0	1.0
2.0	0.5	1.0	3.5	2.0	1.5	3.0	3.5	2.5	1.5	3.0	1.0
3.0	0.0	1.5	2.5	1.5	1.5	3.0	4.0	3.0	2.0	3.0	1.0
3.5	0.0	2.0	2.5	1.0	1.5	3.0	4.0	4.0	3.0	3.5	1.0
2.5	0.0	3.5	2.0	1.0	1.5	3.0	4.0	5.0	2.5	4.0	1.0
2.0	1.0	4.5	2.0	0.5	1.5	2.5	3.5	5.5	2.0	4.5	1.5
1.5	2.5	4.5	1.5	1.0	2.0	2.5	2.5	6.0	2.0	4.5	2.0
1.5	3.0	4.5	1.5	1.0	2.0	2.0	2.0	6.0	2.0	3.5	2.5
1.5	3.0	5.0	2.0	1.0	2.5	1.5	1.5	2.5	2.0	2.0	2.0
1.5	2.5	5.0	2.5	1.5	3.0	1.0	1.5	2.0	2.0	1.5	1.5
2.0	2.5	5.0	3.0	2.0	2.5	1.0	1.0	1.5	2.0	1.0	1.0
2.5	2.5	5.5	3.0	2.0	2.5	1.0	1.0	1.5	1.5	0.5	1.0
2.5	2.0	5.5	2.5	1.5	2.0	1.0	1.0	1.5	1.5	0.0	0.5
2.0	2.0	5.5	2.0	1.0	1.5	1.0	0.5	1.5	1.5	0.0	0.0
2.0	2.0	5.0	2.0	1.0	1.5	1.0	0.5	2.5	1.5	0.0	0.0
2.0	2.0	4.0	1.5	1.0	1.0	1.0	0.5	3.5	1.0	0.0	0.5
2.0	2.0	3.5	1.5	1.0	1.0	1.0	1.0	4.0	1.0	0.5	1.0
2.0	2.0	3.5	1.5	1.5	1.0	1.0	1.5	3.5	1.0	0.5	1.5
2.0	2.0	3.5	1.5	2.0	1.0	1.5	1.5	3.0	1.5	1.0	1.5
2.5	2.5	4.0	1.5	2.0	2.0	2.0	2.0	2.5	1.5	1.5	1.5
2.0	2.0	4.0	1.5	2.5	5.0	2.5	2.0	2.0	1.5	2.5	1.5
2.5	2.5	4.5	1.5	2.5	4.5	3.0	2.0	2.0	2.0	5.0	1.5
2.0	2.5	4.5	1.5	2.5	4.0	3.5	2.0	2.0	1.5	5.0	1.5
2.0	3.0	4.0	1.5	2.5	3.5	3.5	2.5	2.0	1.5	3.0	1.5
2.0	3.0	4.0	1.5	2.5	3.0	3.5	2.5	2.0	1.5	2.0	1.5
2.0	3.0	3.5	2.0	2.5	3.0	3.0	2.0	2.0	1.5	1.0	2.0
1.5	2.5	3.0	2.5	2.0	2.5	3.0	1.5	2.0	1.5	1.0	2.5
1.5	2.0	2.5	3.0	1.5	2.5	3.0	1.5	2.0	1.5	0.5	2.5
1.5	1.5	2.0	3.0	1.0	2.5	2.5	1.0	2.0	1.5	0.5	2.5
1.5	1.5	2.0	4.0	1.0	3.0	2.5	1.0	2.0	1.5	0.5	2.0
1.5	1.5	1.5	4.0	0.5	2.0	2.0	1.0	2.5	1.0	0.5	1.5
2.0	1.0	1.5	3.0	0.0	1.5	2.0	1.0	3.0	1.0	0.5	1.5
2.5	1.0	1.5	2.5	0.0	1.0	1.5	1.0	3.5	1.0	1.5	1.0
3.0	1.0	1.5	2.5	0.0	0.5	1.5	1.0	3.5	1.0	2.0	1.0
3.0	0.5	1.5	2.0	0.0	0.5	1.5	1.5	3.0	1.0	2.5	1.0
3.0	0.5	1.5	2.0	0.0	0.0	1.5	2.5	2.5	0.5	2.5	1.0
3.0	1.0	1.5	2.0	0.0	0.0	2.0	2.5	2.5	0.5	2.5	1.0
3.0	1.0	1.5	2.0	0.5	0.0	2.0	2.5	2.5	1.0	2.5	1.0
3.0	1.0	1.5	2.0	1.0	0.0	2.0	2.0	2.5	1.0	2.5	1.0
3.0	2.0	1.0	2.0	1.0	0.0	2.0	1.5	2.0	1.5	2.5	1.0
2.5	2.0	1.0	2.5	1.0	0.0	2.0	1.0	1.5	1.5	2.5	1.0
2.5	1.5	0.5	3.5	1.0	0.5	2.0	1.0	1.0	2.5	3.0	1.0
1.5	1.0	0.5	4.0	2.0	1.5	2.0	1.0	1.0	4.0	4.5	0.5
1.5	1.0	1.0	4.5	3.0	2.5	2.0	1.5	1.0	3.5	3.0	0.5
1.0	1.0	2.0	4.5	2.5	2.5	2.5	2.5	1.0	3.5	2.0	0.5
1.0	1.0	3.0	4.0	2.0	2.5	3.0	2.5	1.0	3.0	1.5	0.5

1.0	2.0	1.0	0.5	1.5	1.0	1.5	5.0	1.0	1.5	2.0	2.0
1.5	1.5	1.5	0.5	2.0	1.5	1.5	5.0	1.0	1.5	3.0	2.0
2.5	1.5	1.5	1.0	2.5	2.5	1.0	5.5	1.0	2.0	3.0	2.0
2.5	1.0	1.5	1.0	2.5	3.0	1.0	5.5	1.5	2.0	2.5	2.0
2.5	1.0	1.5	1.5	2.5	3.0	1.0	4.0	2.5	1.5	2.0	1.5
2.0	1.0	1.5	1.5	2.5	3.0	1.0	3.0	3.0	1.5	2.0	1.5
2.0	1.0	1.5	1.5	2.5	3.0	0.5	3.0	3.0	1.5	1.5	1.5
1.5	1.0	2.0	1.5	2.5	4.0	0.5	3.0	3.0	1.5	1.5	1.5
1.5	1.5	2.0	1.5	2.5	4.5	0.5	2.5	3.0	2.0	1.5	1.5
1.5	2.0	2.5	1.5	2.5	4.5	0.5	2.5	3.0	3.0	1.5	1.5
1.5	2.5	3.0	1.5	3.0	3.5	1.0	2.0	3.5	3.0	1.5	1.5
1.5	2.5	4.0	1.5	3.0	3.0	1.5	2.0	3.5	3.0	1.5	1.5
2.0	2.5	4.0	1.5	3.0	2.5	2.0	2.0	2.5	3.0	2.0	1.5
2.0	2.0	3.5	1.0	3.0	2.0	2.5	2.0	2.0	3.0	2.0	2.0
2.0	2.0	3.0	1.0	3.0	2.0	2.5	2.0	1.5	3.0	2.0	2.0
2.0	1.5	3.0	1.0	2.5	1.5	2.5	2.0	1.0	3.0	2.0	1.5
1.5	1.5	3.0	1.0	2.5	1.5	2.5	2.0	1.0	3.0	2.0	1.5
1.0	1.5	2.5	1.0	2.0	1.5	2.5	2.0	1.0	3.0	2.0	1.5
1.0	1.5	2.5	1.0	1.5	2.0	2.5	2.0	1.0	3.0	1.5	2.0
1.0	1.5	2.0	1.5	1.5	2.0	2.5	2.0	1.0	3.0	1.5	2.0
1.5	1.5	1.5	2.0	1.5	2.0	2.5	1.5	1.5	3.0	1.0	3.0
2.0	2.5	1.5	4.5	1.5	1.5	2.5	1.5	2.0	3.0	1.0	3.0
2.5	3.0	1.5	5.0	1.5	1.5	2.5	1.5	2.0	2.5	1.0	3.0
2.0	4.5	1.5	5.0	1.5	1.0	2.0	1.0	1.5	2.0	0.5	3.0
2.0	4.0	1.5	4.0	1.5	1.0	1.5	1.0	1.5	2.0	0.5	2.5
2.5	3.0	1.5	3.5	1.5	1.0	1.0	1.0	1.5	2.5	0.5	1.5
2.5	3.0	1.5	2.5	1.5	1.0	1.0	1.0	1.0	3.0	0.5	1.0
2.5	2.5	2.0	2.0	1.5	1.0	0.5	1.0	1.0	3.0	0.5	1.0
3.0	2.5	2.5	1.5	1.0	1.0	0.0	1.0	1.0	3.0	1.0	0.5
3.0	2.5	2.5	1.5	1.0	1.5	0.0	1.0	1.0	2.0	1.0	0.5
2.5	2.5	2.0	1.5	1.0	2.0	0.0	1.5	1.5	1.5	2.0	0.5
1.5	3.0	2.0	1.5	1.0	2.5	0.0	2.0	2.5	1.0	2.5	0.5
1.0	3.0	2.5	1.5	1.0	2.5	0.5	3.5	3.0	1.0	2.5	0.5
1.0	2.5	2.5	1.5	1.5	2.5	0.5	4.0	3.0	0.5	2.5	0.5
1.0	2.5	3.5	2.0	2.0	2.0	1.0	5.5	2.0	0.5	2.5	0.5
0.5	2.0	4.0	3.0	2.5	1.5	1.0	6.0	1.5	0.5	2.5	0.5
0.5	2.0	3.5	4.0	2.5	1.0	1.0	6.5	1.5	0.5	2.0	1.0
1.0	1.5	3.5	4.0	3.5	1.0	1.0	6.5	1.0	0.5	2.0	2.0
1.0	1.5	3.5	3.5	6.0	0.5	1.0	6.0	1.0	1.0	2.0	5.5
1.0	1.5	2.5	3.5	7.0	0.5	1.0	5.0	1.0	1.0	2.0	5.5
1.5	1.5	1.5	3.0	2.5	0.5	1.0	4.5	1.0	1.5	2.0	1.5
3.0	1.5	1.5	2.5	2.0	0.5	1.5	3.5	1.0	1.5	2.0	1.0
3.5	1.5	1.0	2.0	1.5	1.0	2.0	2.5	1.0	1.0	1.5	0.5
3.5	1.5	1.0	1.5	1.0	1.5	3.0	1.5	1.0	1.0	1.5	0.0
3.5	1.5	0.5	1.5	1.0	1.5	5.0	1.5	1.0	1.0	1.5	0.0
3.0	1.0	0.5	1.5	1.0	1.5	5.0	1.0	1.5	1.5	2.0	0.0

0.0	0.5	1.5	1.0	1.0	1.5
0.0	0.5	1.5	1.0	1.0	2.0
0.0	1.0	1.5	1.5	1.0	3.0
0.0	1.0	1.5	1.5	1.5	3.0
0.0	1.0	1.5	1.5	2.0	2.5
0.0	1.0	1.5	2.0	2.0	2.5
0.0	1.0	1.5	2.5	2.0	2.0
0.5	0.5	1.5	2.5	1.5	2.0
1.0	0.5	1.5	2.0	1.5	2.0
3.5	1.0	1.5	1.5	1.5	1.5
3.5	1.5	1.5	1.5	2.0	
3.5	2.5	1.5	1.0	3.0	
3.0	3.0	1.5	1.0	3.0	
2.5	3.0	1.5	1.0	2.5	
2.0	4.0	1.5	1.0	2.0	
1.5	4.0	1.5	1.0	2.0	
1.0	4.0	2.0	1.0	1.5	
1.0	4.0	2.0	1.0	1.5	
1.0	3.0	1.5	1.0	1.5	
1.0	3.0	1.5	1.0	1.5	
1.0	2.5	1.0	2.0	1.5	
1.0	2.0	1.5	2.0	1.5	
1.0	2.0	1.5	2.5	1.5	
1.5	1.5	1.5	2.5	1.5	
1.5	1.5	1.5	3.0	1.5	
1.5	1.5	1.5	3.5	1.5	
1.0	1.5	1.5	3.0	2.0	
1.0	1.5	1.5	3.0	1.5	
1.0	1.5	1.5	2.5	1.5	
1.0	1.5	1.5	2.5	1.0	
1.0	1.5	2.0	2.5	1.0	
1.5	2.0	5.0	2.5	1.0	
1.5	2.5	5.5	2.5	1.0	
2.0	2.5	5.5	2.5	1.5	
2.5	2.0	5.5	3.0	1.5	
2.5	1.5	5.5	3.0	1.5	
2.5	1.5	5.0	3.5	1.5	
3.0	1.0	4.5	3.5	1.5	
3.5	1.0	4.0	3.0	1.5	
3.5	1.5	3.5	2.5	1.0	
2.5	1.5	3.0	2.0	1.0	
1.5	1.5	2.5	1.5	1.0	
1.0	1.5	2.0	1.5	1.5	
1.0	1.5	1.5	1.5	1.5	
1.0	1.5	1.0	1.0	1.5	
0.5	1.5	1.0	1.0	1.5	

Appendix D: Mathematical derivation of the two-phase model in CHAPTER IV

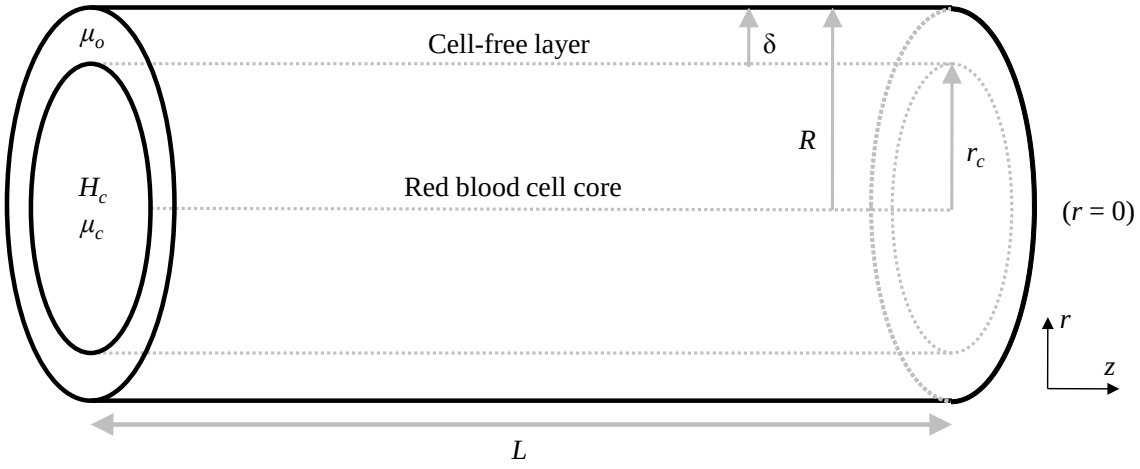

Figure A-VI-2: Schematic diagram of a two-phase model.

Governing equations

$$-\frac{\partial p}{\partial z}+\frac{\mu_c}{r}\frac{\partial}{\partial r}\left(r\frac{\partial u_c}{\partial r}\right)=0, \quad (0\le r<r_c) \tag{A1}$$

$$-\frac{\partial p}{\partial z}+\frac{\mu_o}{r}\frac{\partial}{\partial r}\left(r\frac{\partial u_o}{\partial r}\right)=0, \quad (r_c<r<R) \tag{A2}$$

Boundary conditions (BC)

$$\frac{\partial u_c}{\partial r}=0 \quad at\ r=0 \tag{A3a}$$

$$u_0=0 \quad at\ r=R \tag{A3b}$$

$$u_c=u_o \quad at\ r=r_c \tag{A3c}$$

$$\mu_c\frac{\partial u_c}{\partial r}=\mu_o\frac{\partial u_o}{\partial r} \quad at\ r=r_c \tag{A3d}$$

Solution for RBC core domain ($0 \le r < r_c$)

$$\frac{\partial p}{\partial z} = \frac{\mu_c}{r}\frac{\partial}{\partial r}\left(r\frac{\partial u_c}{\partial r}\right)$$

$$\frac{1}{2}\frac{1}{\mu_c}\frac{\partial p}{\partial z}r^2 = r\frac{\partial u_c}{\partial r} + C_1 \qquad \text{by } BC \text{ (A3a), } C_1 = 0$$

$$\frac{1}{2}\frac{1}{\mu_c}\frac{\partial p}{\partial z}r = \frac{\partial u_c}{\partial r}$$

$$\text{thus, } u_c(r) = -\frac{1}{4}\frac{1}{\mu_c}\frac{\partial p}{\partial z}r^2 + C_2 \qquad \text{(A4)}$$

Solution for cell-free layer domain ($r_c < r \le R$)

$$\frac{\partial p}{\partial z} = \frac{\mu_o}{r}\frac{\partial}{\partial r}\left(r\frac{\partial u_o}{\partial r}\right)$$

$$\frac{1}{2}\frac{1}{\mu_o}\frac{\partial p}{\partial z}r^2 = \frac{\partial u_o}{\partial r} + C_3$$

$$\frac{1}{2}\frac{1}{\mu_o}\frac{\partial p}{\partial z}r = r\frac{\partial u_o}{\partial r} + \frac{C_3}{r}$$

$$u_o(r) = -\frac{1}{4}\frac{1}{\mu_0}\frac{\partial p}{\partial z}r^2 + C_3\,ln(r) + C_4 \text{ by } BC \text{ (A3b), } C_4 = \frac{1}{4}\frac{1}{\mu_0}\frac{\partial p}{\partial z}R^2 - C_3\,ln(R)$$

$$\text{thus, } u_o(r) = -\frac{1}{4}\frac{1}{\mu_0}\frac{\partial p}{\partial z}r^2 + C_3\,ln(r) + \frac{1}{4}\frac{1}{\mu_0}\frac{\partial p}{\partial z}R^2 + C_3\,ln(R) \qquad \text{(A5)}$$

By imposing *BC* (A3c) and (A3d) to Eqs (A4) and (A5)

$$\begin{cases} \mu_c\dfrac{\partial u_c}{\partial r} = \dfrac{1}{2}\dfrac{\partial p}{\partial z}r \\ \mu_o\dfrac{\partial u_o}{\partial r} = \dfrac{1}{2}\dfrac{\partial p}{\partial z}r - \dfrac{C3}{r} \end{cases}$$

By *BC*(A3d), $\frac{1}{2}\frac{\partial p}{\partial z}r_h - \frac{C_3}{r} = \frac{1}{2}\frac{\partial p}{\partial z}r_h$, thus $C_3 = 0$

$$\begin{cases} u_c(r) = \frac{1}{4}\frac{1}{\mu_c}\frac{\partial p}{\partial z}r^2 - C_2 \\ u_o(r) = -\frac{1}{4}\frac{1}{\mu_o}\frac{\partial p}{\partial z}(R^2 - r^2) \end{cases}$$

By *BC* (A3c), $-\frac{1}{4}\frac{1}{\mu_o}\frac{\partial p}{\partial z}(R^2 - r_h^{\,2}) = \frac{1}{4}\frac{1}{\mu_c}\frac{\partial p}{\partial z}r_h^2 - C_2$

thus, $C_2 = -\frac{1}{4}\frac{1}{\mu_o}\frac{\partial p}{\partial z}(R^2 - r_h^2) + \frac{1}{4}\frac{1}{\mu_c}\frac{\partial p}{\partial z}r_h^2$

$$\therefore \begin{cases} u_c(r) = -\frac{1}{4}\frac{1}{\mu_o}\frac{\partial p}{\partial z}\left[R^2 - r_h^2 + \frac{\mu_o}{\mu_c}(r_h^2 - r^2)\right] \\ u_o(r) = -\frac{1}{4}\frac{1}{\mu_o}\frac{\partial p}{\partial z}(R^2 - r^2) \end{cases}$$

By introducing non-dimensionalization parameters

$$\xi = \frac{r}{R},\ \lambda = \frac{r_h}{R},\ P = \frac{|\Delta p|}{L}$$

Finally, we can get velocity profile function for the two domains.

$$\begin{cases} u_c(\xi) = \frac{PR^2}{4\mu_o}\left[1 - \lambda^2 + \frac{\mu_o}{\mu_c}\left(\lambda^2 - \xi^2\right)\right], & (0 \le \xi \le \lambda) \\ u_o(\xi) = \frac{PR^2}{4\mu_o}\left[1 - \xi^2\right], & (\lambda \le \xi \le 1) \end{cases}$$

The Volumetric Flow Rate

The volumetric flow rate of the blood is given by:

$$Q = 2\pi R^2 \int_0^{\lambda} u_c(\xi)\xi d\xi + 2\pi R^2 \int_{\lambda}^{1} u_o(\xi)\xi d\xi$$

$$Q = 2\pi R^2 \frac{PR^2}{4\mu_o}\left[\int_0^{\lambda}\left(1-\lambda^2+\frac{\mu_o}{\mu_c}\lambda^2-\frac{\mu_o}{\mu_c}\xi^2\right)\xi d\xi + \int_{\lambda}^{1}(1-\xi^2)\xi d\xi\right]$$

$$Q = 2\pi R^2 \frac{PR^2}{4\mu_o}\left[\left|\frac{1}{2}\xi^2-\frac{1}{2}\lambda^2\xi^2+\frac{1}{2}\frac{\mu_o}{\mu_c}\lambda^2\xi^2-\frac{1}{4}\frac{\mu_o}{\mu_c}\xi^4\right|_0^{\lambda}+\left|\frac{1}{2}\xi^2-\frac{1}{4}\xi^4\right|_{\lambda}^{1}\right]$$

$$Q = \frac{\pi PR^4}{8\mu_o}\left[\frac{\mu_o}{\mu_c}\lambda^4+1-\lambda^4\right] \qquad \text{(A6)}$$

The Overall Mass Balance of The Red Blood Cells in The Tube

$$QH_d = 2\pi R^2\int_0^1 \xi u(\xi)h(\xi)d\xi \text{ where } h(\xi)=\begin{cases}H_c, & 0 \le \xi \le \lambda\\ 0, & \lambda<\xi\le 1\end{cases}$$

$$QH_d = 2\pi R^2\int_0^{\lambda}\xi u_c(\xi)H_c d\xi + \int_{\lambda}^{1}\xi u_o(\xi)\cdot 0 d\xi$$

$$QH_d = 2\pi R^2\frac{PR^2}{4\mu_o}H_c\left|\frac{1}{2}\xi^2-\frac{1}{2}\lambda^2\xi^2+\frac{1}{2}\frac{\mu_o}{\mu_c}\lambda^2\xi^2-\frac{1}{4}\frac{\mu_o}{\mu_c}\xi^4\right|_0^{\lambda}$$

$$Q = \frac{\pi PR^4}{8\mu_o}\left(\frac{H_c}{H_d}\right)\left[\frac{\mu_o}{\mu_c}\lambda^4+2\lambda^2(1-\lambda^2)\right] \qquad \text{(A7)}$$

Eq. (A6) can be rewritten as:

$$Q = \frac{\pi PR^4}{8\mu_{app}} = \frac{\pi PR^4}{8\mu_o}\left[\frac{\mu_o}{\mu_c}\lambda^4+1-\lambda^4\right]$$

$$\mu_{app} = \mu_o\left[\frac{\mu_o}{\mu_c}\lambda^4+1-\lambda^4\right] \qquad \text{(A8)}$$

The tube hematocrit H_t is defined by:

$$H_t = 2\int_0^1 h(\xi)\xi d\xi \quad \text{where } h(\xi)=\begin{cases}H_c, & 0 \le \xi \le \lambda\\ 0, & \lambda<\xi\le 1\end{cases}$$

$$H_t = 2H_c\left|\frac{1}{2}\xi^2\right|_0^{\lambda}$$

$$\therefore H_t = \lambda^2 H_c \tag{A9}$$

From the relationship between Q (Eq. (A6)) and QH_D (Eq. (A7)):

$$\frac{\pi P R^4}{8\mu_o}\left[\frac{\mu_o}{\mu_c}\lambda^4 + 1 - \lambda^4\right] = \frac{\pi P R^4}{8\mu_o}\frac{H_d}{H_c}\left[\frac{\mu_o}{\mu_c}\lambda^4 + 2\lambda^4 + 2\lambda^2(1-\lambda^2)\right]$$

$$\frac{H_c}{H_d} = \frac{\frac{\mu_o}{\mu_c}\lambda^4 + 1 - \lambda^4}{\frac{\mu_o}{\mu_c}\lambda^4 + 2\lambda^2(1-\lambda^2)} \tag{A10}$$

Appendix E: MATLAB code for the simulation in CHPTER VI

```
% CFL prediction with two-phase model

%*********************************************************************
% Parameters
%*********************************************************************
% Hd: discharged hematocrit which is equal to systemic hematocrit
% D: diameter of tube
% gamma: pseudoshear rate of tube
% Ht: tube hematocrit
% mu_app_rel: relative apparent viscosity of tube
% mu_app: apparent viscosity of tube
% mu_c: apparent viscosity of core
%*********************************************************************
function TwoPhaseCFL()
close all

Hd = 0.4;
mu_pl = 1.25;
gamma = (5:1:300)';
D = 30:1:100;

% coefficients for relative apparent viscosity of tube (mu_rel)
condition(1).name = 'Control';
condition(1).a = [5.42e-5 -1.47e-5 0 0];
condition(1).b = [1.28e-2 2.43e-3 0 0];
condition(1).c = [3.6764 -0.22357 100 100];
condition(2).name = 'Normal';
condition(2).a = [7.27e-4 -2.01e-5 1.17e-3 -1.07e-4];
condition(2).b = [-3.92e-2 1.96e-3 -8.65e-2 1.41e-2];
condition(2).c = [4.1446 -0.197714 2.744 -0.2938];
condition(3).name = 'Hyper';
condition(3).a = [4.97e-4 -2.61e-5 4.95e-4 -8.44e-6];
condition(3).b = [-3.11e-2 3.64e-3 -2.47e-2 1.42e-3];
condition(3).c = [5.2512 -0.2907 1.4897 -8.71e-3];

% coefficients for viscosity of core (mu_c)
condition(1).d = [1.6536 5.4967 -0.5134 0.9667];
condition(2).d = [4.2159 4.0554 -0.2639 0.8277];
condition(3).d = [5.2369 4.1601 -0.2908 0.8058];

% solving process
for z = 1:1:3 % RBC aggregation conditions
    disp(['condition: ',condition(z).name]);
    for j = 1:length(D) % tube diamters
        disp(['Diamter: ', num2str(D(j))]);
        for i = 1:length(gamma) % pseudoshear rates
            [beta(i,j) lamda(i,j) error(i,j) Hc(i,j) mu_c(i,j)] ...
                = Sol_CFL(Hd,mu_pl,D(j),gamma(i),condition(z));
        end
    end
    ncfl = 1-lamda; %normalized CFL
    for i=1:length(D) % actual CFL
        cfl(:,i) = D(i)/2.*ncfl(:,i);
```

```
    end

    % Saving results
    cfl30_5_100(z,:,:) = cfl(:,1:5:end);
    temp_cfl = cfl(:,1:5:end);
    ncfl30_5_100(z,:,:) = ncfl(:,1:5:end);
    temp_ncfl = ncfl(:,1:5:end);
    beta30_5_100(z,:,:) = beta(:,1:5:end);
    temp_beta = beta(:,1:5:end);
    Hc30_5_100(z,:,:) = Hc(:,1:5:end);

    fname = strcat(num2str(z),'.',condition(z).name,'-cfl.txt');
    save (fname, 'temp_cfl', '-ascii','-tabs');
    fname = strcat(num2str(z),'.',condition(z).name,'-ncfl.txt');
    save (fname, 'temp_ncfl', '-ascii','-tabs');
    fname = strcat(num2str(z),'.',condition(z).name,'-beta.txt');
    save (fname, 'temp_beta', '-ascii','-tabs');

    % collecting data at 5s^-1 & 300s^-1
    at5ncfl(:,z) = ncfl(1,1:5:end);
    at300ncfl(:,z) = ncfl(end,1:5:end);
    at5cfl(:,z) = cfl(1,1:5:end);
    at300cfl(:,z) = cfl(end,1:5:end);

    % collecting data for a comparison wtih in vivo
    for i=1:4
        target_gamma = invivo_gamma(z,i);
        target_D = invivo_D(z,i);
        row = find(gamma == target_gamma);
        col = find(D == target_D);
        invivo(z,i) = ncfl(row,col);
    end
end

% Plot figures
colr = ['b','g','r'];
figure,
for z = 1:1:3
    semilogx(gamma,ncfl30_5_100(z,:,1),colr(z))
    hold on
end
hold off
title('30um');
legend('Non','Normal','Hyper');
xlabel('Pseudoshear rate');
ylabel('Normalized CFL');
ylim([0,0.4]);

figure,
for z = 1:1:3
    semilogx(gamma,ncfl30_5_100(z,:,5),colr(z))
    hold on
end
hold off
title('50um');
legend('Non','Normal','Hyper');
```

```
xlabel('Pseudoshear rate');
ylabel('Normalized CFL');
ylim([0,0.4]);

figure,
for z = 1:1:3
    semilogx(gamma,ncfl30_5_100(z,:,15),colr(z))
    hold on
end
hold off
title('100um');
legend('Non','Normal','Hyper');
xlabel('Pseudoshear rate');
ylabel('Normalized CFL');
ylim([0,0.4]);

fname = strcat('at5ncfl.txt');
save(fname, 'at5ncfl', '-ascii','-tabs');
fname = strcat('at300ncfl.txt');
save(fname, 'at300ncfl', '-ascii','-tabs');
fname = strcat('at5cfl.txt');
save(fname, 'at5cfl', '-ascii','-tabs');
fname = strcat('at300cfl.txt');
save(fname, 'at300cfl', '-ascii','-tabs');

figure, plot(D(1:5:end),at5ncfl);
title('at 5 s^-^1');
legend('Non','Normal','Hyper');
xlabel('Diameter');
ylabel('Normalized CFL');
ylim([0,0.4]);

figure, plot(D(1:5:end),at300ncfl);
title('at 300 s^-^1');
legend('Non','Normal','Hyper');
xlabel('Diameter');
ylabel('Normalized CFL');
ylim([0,0.4]);
%**************************************************************************

%**************************************************************************
% Solution function for iterative method
%**************************************************************************
function [beta lamda error Hc mu_c] = ...
    Sol_CFL(Hd,mu_pl,D,gamma,para)
% Define parameters for each viscosity function
a = para.a;
b = para.b;
c = para.c;
d = para.d;
p = zeros(length(a));

% Relative apparent viscosty
for i = 1:4
    p(i) = a(i)*D^2+b(i)*D+c(i);
end
```

```
mu_app_rel = min(p(1)*gamma^p(2),p(3)*exp(p(4)*gamma));

% Hematocrit function
Ht = Hd*(Hd+(1-Hd)*(1+0.387*exp(-0.1779*D)-0.603*exp(-0.0111*D)-
0.0187*exp(-9.06e-11*D)));

%initial guess for Hc (Hc > Hd)
Hc = Hd;
gradient = 0.01;
error = 1;

while error >= 1e-8
    lamda = sqrt(Ht/Hc);
    mu_c = d(1)*exp(d(2)*Hc)*gamma^((d(3)*Hc+d(4))-1);
    beta = mu_app_rel*(1-lamda^4)/(1-mu_app_rel*mu_pl/mu_c*lamda^4);
    mu_o = beta*mu_pl;

    % shear rate to pseudoshear rate
    % 1.gamma: pseudo-shear rate of tube
    % 2.gamma_c: pseudo-shear rate of core
    % 3.shear: shear rate for core viscosity
    % 4.gamma -> gamma_c -> shear
    gamma_c = (gamma/lamda^3)*(1-(mu_app_rel/beta)*(1-lamda^4));
    shear = 6.31*gamma_c;
    mu_c = d(1)*exp(d(2)*Hc)*shear^((d(3)*Hc+d(4))-1);
    beta = mu_app_rel*(1-lamda^4)/(1-mu_app_rel*mu_pl/mu_c*lamda^4);
    mu_o = beta*mu_pl;

    Hc_final = Hd*(mu_o/mu_c*lamda^4+1-lamda^4)/...
        (mu_o/mu_c*lamda^4+1-lamda^4-(1-lamda^2)^2);

    error = (Hc_final-Hc)^2;
    Hc = Hc_final + gradient*abs(Hc_final-Hc);
end
%*********************************************************************
% code ended
```

VITA, PUBLICATIONS AND CONFERENCES

VITA

Bachelor of Engineering (1999-2006)

- Biomedical Engineering, Yonsei University, Korea

Master in Biomedical Engineering (2006-2008)

- Biomedical Engineering, Yonsei University, Korea
- Computer Aided Biomedical Engineering Lab., under the supervision of Prof. Kim Han Sung
- Thesis title: "*A study for the effect of large blood vessel and optimizing input waveforms in radio-frequency liver tumor ablation using finite element method*"

Doctor of Philosophy in Bioengineering (2008-2012)

- Bioengineering, National University of Singapore, Singapore
- Microhemodynamics Lab., under the supervision of Dr. Kim Sangho
- Thesis title: "*Rheological aspect of cell-free layer formation in micro-blood flow: Experimental and Numerical study*"

JOURNAL PUBLICATIONS

[1] Bumseok Namgung, Seungkwan Cho, Peng Kai Ong, Hiromi Sakai, and Sangho Ki m, Characteristics changes of cell-free layer formation by erythrocyte aggregation i n a 25-μm tube. (***CHAPTER III in this dissertation***, S***ubmitted and now under rev iew***)

[2] Bumseok Namgung, Meongkeun Ju, Pedro Cabrales, and Sangho Kim, Two-phase model for prediction of cell-free layer width in blood flow, *Microvascular Research* , DOI: 10.1016/j.mvr.2012.10.006. **(*CHAPTER IV in this dissertation*)**

[3] Bumseok Namgung, Peng Kai Ong, Yun Hui Wong, Dohyung Lim, Keyoung Jin C hun, and Sangho Kim, A comparative study of histogram-based thresholding metho ds for determination of cell-free layer width in small blood vessels. *Physiological M easurement*, 31(9), N61-N70, 2010. (***CHAPTER II in this dissertation***)

[4] Bumseok Namgung, Peng Kai Ong, Paul C. Johnson, and Sangho Kim, Effect of ce ll-free layer variation on arteriolar wall shear stress, *Annals of Biomedical Engineer ing*, 39(1), 359-366, 2010. (***CHAPTER V in this dissertation***)

[5] Meongkeun Ju, Bumseok Namgung, and Sangho Kim, Application of Refutas mode l to estimate erythrocyte viscosity in a dextran solution, *Macromolecular Research*, 20(8), 887-890, 2012.

[6] Peng Kai Ong, Swati Jain, Bumseok Namgung, Sangho Kim, Keyoung Jin Chun an d Dohyung Lim, Study of time-dependent characteristics of a syllectogram in the pr esence of aggregation inhibition, *International Journal of Precision Engineering an d Manufacturing*, 13(3), 421-428, 2012.

[7] Peng Kai Ong, Seung Kwan Cho, Bumseok Namgung, and Sangho Kim, Effects of cell-free layer formation on NO/O2 bioavailability in small arterioles, *Microvascula r Research*, 83(2), 168-177, 2012.

[8] Peng Kai Ong, Swati Jain, Bumseok Namgung, Yeon I Woo, and Sangho Kim, Cell -free layer formation in small arterioles at pathological levels of erythrocyte aggreg ation, *Microcirculation*, 18(7), 541-551, 2011.

[9] Peng Kai Ong, Swati Jain, Bumseok Namgung, Yeon I Woo, Hiromi Sakai, Dohyu ng Lim, Keyoung Jin Chun, and Sangho Kim, An automated method for cell-free la yer width determination in small arterioles. *Physiological Measurement*, 32(3), N1-

N12, 2011.

[10] Peng Kai Ong, Bumseok Namgung, Paul C. Johnson, and Sangho Kim, Effect of er ythrocyte aggregation and flow rate on cell-free layer formation in arterioles. *Ameri can Journal of Physiology – Heart and Circulatory Physiology*, 298(6), H1870-187 8, 2010.

[11] Sangho Kim, Bumseok Namgung, Peng Kai Ong, Young I. Cho, Keyoung Jin Chun and Dohyung Lim, Determination of rheological properties of whole blood with a s canning capillary-tube rheometer using constitutive models. *Journal of Mechanical Science and Technology*, 23, 1718-1726, 2009.

CONFERENCE PRESENTATIONS

[1] B. Namgung, Y. Woo and S. Kim, "Effect of red cell flux imbalance on cell-free laye r formation in a venular bifurcation", *14th International congress of biorheology and 7th international conference on clinical hemorheology*, Istanbul Turkey, 4-7 July, 201 2.

[2] S. Cho, P. K. Ong, B. Namgung and S. Kim, "Temporal variation of the cell-free laye r width may influence nitric oxide transport in small arerioles", *14th International con gress of biorheology and 7th international conference on clinical hemorheology*, Istan bul Turkey, 4-7 July, 2012.

[3] B. Namgung, M. K. Ju, P. K. Ong and S. Kim, "Two-phase model for prediction of c ell-free layer formation in blood flow", *Asian Congress of Microcirculation*, Bangko k Thailand, 26-28 October, 2011.

[4] M. K. Ju, B. Namgung, and S. Kim, "Application of Refutas model in blood viscosity determination", *Asian Congress of Microcirculation*, Bangkok Thailand, 26-28 Octo ber, 2011.

[5] B. Namgung, P. K. Ong, S. Jain, D. Lim, K.J. Chun, and S. Kim, "Study of time-depe ndent characteristics of a syllectogram in the presence of aggregation inhibition", *Exp erimental Biology*, Anaheim California US, 24-28 April, 2010.

[6] B. Namgung, P. K. Ong, P. C. Johnson, S. Kim, "Effects of cell-free layer width and its variability on wall shear stress in arterioles", *Experimental Biology*, New Orleans

Louisiana US, 18-22 April, 2009.

[7] P. K. Ong, B. Namgung, P. C. Johnson, S. Kim, "Effect of erythrocyte aggregation a nd flow rate on temporal variation of cell-free layer width in arterioles", *Experimenta l Biology*, New Orleans Louisiana US, 18-22 April, 2009.

[8] B. Namgung, P. K. Ong, S. Kim, "Effects of mean cell-free layer thickness and its variability on wall shear stress in arteriolar network", *ICBME 2008*, Singapore, 3-6 December, 2008.

Blank Page